IDEALIZED SIMULATIONS OF SUPERCELL THUNDERSTORMS INTERACTING WITH THE APPALACHIAN MOUNTAINS

by

Roger R. Riggin IV

A thesis submitted to the faculty of
The University of North Carolina at Charlotte
in partial fulfillment of the requirements
for the degree of Master of Science in
Earth Science

Charlotte

2022

Approved by:

_____
Dr. Casey Davenport

_____
Dr. Matthew Eastin

_____
Terry Shirley

ABSTRACT

ROGER R. RIGGIN IV. Idealized Simulations of Supercell Thunderstorms Interacting with the Appalachian Mountains (Under the direction of DR. CASEY DAVENPORT)

The Appalachian Mountains within the eastern United States have a considerable impact on daily weather, including supercell thunderstorms. Forecasters currently lack a comprehensive conceptual model to assist with the decision-making process when supercellular hazards occur in this region which is characterized by complex terrain. While some idealized modeling studies have been conducted that have aided in understanding supercell evolution across idealized terrain configurations and environments, there has yet to be an investigation using more realistic thermodynamic and kinematic profiles. In this study, our research aims to increase understanding of supercell interactions with the Appalachian Mountains, using a combination of both realistic and idealized terrain, and a realistic base-state environment, rooted in model analysis proximity soundings gathered from 62 isolated supercells that traversed the south-central Appalachians between 2008-2019. These storms were tracked via radar and classified based on whether they were maintained following interaction with significant terrain ("crossing") or instead dissipated ("non-crossing"). The present study uses an idealized numerical model to further investigate the environmental controls on crossing versus non-crossing storms. Proximity soundings incorporated into the model base-state were constructed from the upstream/initiation, peak elevation, and downstream/ dissipation points along each observed storm track, with composites calculated at each point for both crossing and non-crossing cases. Several experiments were run while using three different terrain configurations (No Terrain, Idealized, and Realistic Terrain). The base-state environment was horizontal homogeneous (aside from terrain-induced variability) and fixed over time. Three terrain configurations were also tested: no terrain, idealized terrain,

and realistic terrain resulting in 12 unique simulations. Results demonstrate four key terrain-induced mechanisms (e.g., terrain blocking, terrain channeling, upslope flow, downslope flow) responsible for modulating simulated supercells as they traverse the south-central Appalachians. In general, these processes lead to kinematic amplifications and reduced thermodynamics at both the meso-γ and meso-β scales. A series of conceptual models are presented to synthesize these terrain-induced mechanisms to aid in operational decision-making processes during future episodes of supercellular convection within the study region.

ACKNOWLEDGEMENTS

There are not enough words to truly express my gratitude to the numerous individuals who guided and supported me through the completion of this work. First and foremost, I extend the utmost gratitude to my advisor, Dr. Casey Davenport for unwavering support throughout the ups and downs of my graduate experience. Secondly, I want to thank the rest of my committee, Dr. Matthew Eastin, and Mr. Terry Shirley for additional suggestions and support throughout the research processes. Additionally, this project would not have been possible without financial and technological support from the following groups: UNCC Department of Geography and Earth Sciences, UNCC Office of OneIT Research Computing Group, and NOAA's CSTAR Program which supported this project through NOAA grant NA19NWS4680003. This research was truly a collaborative effort with numerous individuals that deserve recognition for their efforts towards this project. The first being my prior research partner's Katie McKeown and Sarah Purpura. My work is built upon their extensive research efforts and therefore would not have been possible without their prior dedication. We also appreciate all feedback and assistance from the Storm Prediction Center and the following National Weather Service Offices: Peachtree City, GA, Greenville-Spartanburg, SC, Jackson, KY, Charleston, WV, Blacksburg, VA, and Morristown, TN. Additionally, I thank Dr. George Bryan for the development and maintenance of CM1: the open-source numerical model used in this study. Also, I'd like to extend a huge thank you to Dr. Branden Katona whose efforts made it possible for us to incorporate a realistic terrain field into our simulations. Finally, I want to thank my family and friends who have quite literally kept me sane during the trials and tribulations over the past two years. My family has quite literally been my rock throughout this process with their unending love and support. So many friends, near and far, have provided much needed motivation through their words of encouragement. This is

especially true for my fellow graduate students, Lauren Decker, Andrew Robinson, and Alison Van Ormer, who also made the countless hours in the McEniry office more bearable.

DEDICATION

I dedicate this work to my late grandparents and aunt, Roger R. “Bubby” Riggin Jr, Ruby M. Riggin, and Kimberly B. Richards. Without the years of love and support from them, I would not have made it to this point in my career. Though they are not physically here with us anymore; it is the work ethic, perseverance, and accountability in which all three helped instill in me that brought this project to its completion.

TABLE OF CONTENTS

LIST OF TABLES

LIST OF FIGURES

LIST OF ABBREVIATIONS

ASOS – Automated Surface Observing System

BSS – Base-State Substitution

BWER – Bounded Weak Echo Region

CAPE – Convective Available Potential Energy

CIN – Convective Inhibition

CM1 – Cloud Model 1

CONUS – Continental United States

CSTAR – Collaborative Science, Technology, and Applied Research

CWA – County Warning Area

DEM – Digital Elevation Raster Model

F – Fujita Scale

FFD – Forward Flank Downdraft

EF – Enhanced Fujita Scale

EML – Elevated Mixed Layer

GBR – Great Barrington, Massachusetts

GIS – Geographic Information System

HRRR – High-Resolution Rapid Refresh Model

KFCX – Blacksburg, Virginia Office, or Radar Site

KFFC – Peachtree City, Georgia Office, or Radar Site

KGSP – Greenville-Spartanburg, South Carolina Office, or Radar Site

KJKL – Jacksonville, Kentucky Office, or Radar Site

KMRX – Morristown, Tennessee Office, or Radar Site

KRLX – Charleston, West Virginia Office, or Radar Site

MCS – Mesoscale Convective System

MLCAPE – Mixed-Layer Convective Available Potential Energy

MLCIN – Mixed-Layer Convective Inhibition

MUCAPE – Most Unstable Convective Available Potential Energy

MUCIN – Most Unstable Convective Inhibition

NROT – Normalized Rotation

NSSL – National Severe Storms Laboratory

NWS – National Weather Service

QLCS – Quasi-Linear Convective System

RAP – Rapid Refresh Model

RFD – Rear Flank Downdraft

RH – Relative Humidity

RUC – Rapid Update Cycle Model

SBCAPE – Surface-Based Convective Available Potential Energy

SBCIN – Surface-Based Convective Inhibition

SAR – Southern Appalachian Region

SCS – Southern Cumberland System

SOM – Self-Organizing Maps

SPC – Storm Prediction Center

SRH – Storm Relative Helicity

ST – Significant Tornado (F/EF-2 +)

STP – Significant Tornado Parameter

UH – Integrated 2-5 km Updraft Helicity

USGS – United States Geographic Survey

UTC – Coordinated Universal Time

VIL – Vertically Integrated Liquid

VORTEX – Verification of the Origins of Rotation in Tornadoes Experiment

WRF – Weather Research and Forecasting Model

WER – Weak Echo Region

WFO – Weather Forecast Office

WoFS – Warn-on-Forecast System

WSR-88D – Weather Surveillance Radar 1988 Doppler

CHAPTER 1: INTRODUCTION AND MOTIVATION

1.1 Introduction

Discrete supercell thunderstorms are rare in the vicinity of complex terrain such as the Appalachian Mountains in the eastern United States. Though infrequent, when one occurs it is usually accompanied by significant severe weather including damaging wind gusts, hail, and tornadoes. More prolific examples include the 1974 Super Outbreak (Corfidi, et. al. 2010), the 2002 Veterans Day Weekend Outbreak (Beuchler et. al. 2004), and the 2011 Super Outbreak (Knupp et. al. 2014). Much of our conceptual understanding of supercell thunderstorm dynamics come from studies that investigate convective environments commonly seen across the U.S. Great Plains (e.g., Lemon and Doswell 1979; Davies-Jones 1984; Klemp 1987), with significant advances made through two large field campaigns VORTEX (Verification of the Origins of Rotation in Tornadoes Experiment; Rasmussen et. al. 1994) and VORTEX2 (Wurman et al. 2012). A notable trait of the Great Plains is the relatively flat terrain. However, complexities arise when considering supercells in regions of varying terrain; while the basic structure of a supercell is independent of the location in which it occurs, the storm's inflow environment can be modified by geographic features (e.g., Bosart et al. 2006; Smith et al. 2016; Katona et. al. 2016; Katona and Markowski 2021). Such environmental variability introduces additional complications when forecasting supercell maintenance and evolution in mountainous regions such as the Appalachians.

Prior research on severe convection and terrain has largely focused on orographically-generated convection or linear convective storm modes such as squall lines (e.g., Reeves and Lin 2007; Letkewicz and Parker 2011; Mulholland et al. 2020). More recent explorations have focused on the relationship between complex terrain and supercellular convection, but have

largely been highly idealized (e.g., Markowski and Dotzek 2011; Smith et al. 2016; Katona and Markowski 2021), or isolated case studies (e.g., Keighton et al., 2004; Bosart et. al. 2006; Gaffin 2012; Prociv 2012; Lyza and Knupp 2018). Even with these initial studies, there are lingering questions regarding the relationship between supercells and topography that warrant continued exploration.

1.2 Motivation and Goals

The primary objective of this research is to improve short-term forecasting of supercell thunderstorms in the Central and Southern Appalachian region through the development of a conceptual model of how supercells evolve in differing background environment conditions as they interact with the Appalachian Mountains. Prior work has been completed in investigating both the environmental and radar characteristics of 62 observed discrete supercell thunderstorms that interacted with various terrain features of the Appalachians between 2008-2019 (Purpura et al. 2022; McKeown 2021). The current work builds on these results using an idealized cloud-resolving numerical model to further explore both idealized and realistic terrain influences on crossing and non-crossing supercells in a controlled manner. The inability to determine how a storm would have behaved without the presence of terrain is a commonly noted limitation in prior research (e.g., Markowski and Dotzek 2011). Numerical modeling is the only exploratory method in which we can effectively control the presence of terrain to isolate its influences.

The current work, along with the prior radar and environmental studies, has been a highly collaborative effort, working with the Storm Prediction Center (SPC), and six NWS Weather Forecast Offices (WFO) including: Blacksburg, VA (KFCX), Peachtree City, GA (KFFC); Greenville-Spartanburg, SC (KGSP); Jacksonville, KY (KJKL); Morristown, TN (KMRX); and Charleston, WV (KRLX). Our study area is composed of the collective County Warning Areas

(CWAs) and the associated terrain feature that the listed WFOs have forecasting jurisdiction over (Fig. 1.1a-b). The open communication between our researchers and the NWS forecasters allows us to focus on the results that will be most beneficial for forecasting supercells in proximity to the Central and Southern Appalachians. Our overarching goals are to improve watch and warning issuance that communicate severe weather risks to the public, as well as reduce false alarms scenarios.

The research-oriented goals of this study are specific to the idealized modeling techniques that can aid in the overall goal of improved forecasting. We want to isolate terrain-induced effects on supercell morphology by investigating simulated mature and discrete supercells. Specifically, differences in the low-level inflow environment and storm intensity can be compared between simulations that do and do not include complex terrain. Using simulations containing both idealized and realistic terrain will allow us to link the results back to our study area and provide the most pertinent results to our collaborators.

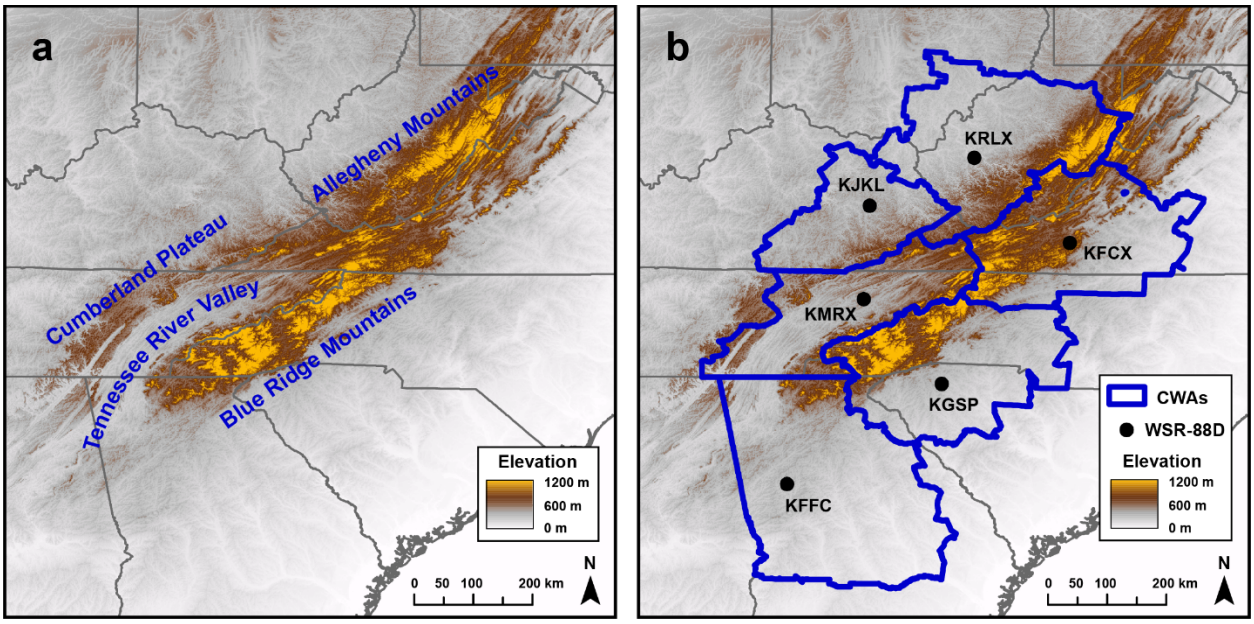

Figure 1.1: Maps of the defined study area. (a) the four main terrain features that compose the South-Central Appalachians are given particular interest: Cumberland Plateau, Great Tennessee Valley, Blue Ridge Mountains, and the Allegheny Mountains; and (b) the six WFO's CWA that composes the geographic extend of our study area. Terrain is emphasized to highlight both the variability & complexity using both a DEM & hillshade raster. The six primary WSR-88D radar sites within the study area are shown with 60 n mi. buffers to highlight notable radar observation gaps (from Purpura et al. 2022).

CHAPTER 2: LITERATURE REVIEW

2.1 Introduction

This chapter provides insight to the key findings of prior studies involving supercell thunderstorms interacting with complex terrain. This literature review has been split up into six sub-sections. Section 2.2 discusses observation-based studies of individual and/or multiple supercells that interacted with complex terrain. Section 2.3 focuses on the climatology of supercells throughout the Weather Forecast Offices (WFOs) relevant to our study (Fig. 1.4). Section 2.4 reviews several key numerical modeling studies of simulated supercells interacting with both idealized and realistic terrain. Section 2.5 summarizes the key results from the Environmental & Radar Observation studies completed for the given study area. Section 2.6 includes a summary of the literature review, discusses the key research gaps in the prior literature, and how the current work intends to help alleviate those gaps.

2.2 Observational Studies

Several case-studies were reviewed to provide a solid understanding of the physical processes that have been observed during supercell thunderstorms while they interact with complex topography. These studies provide observation-based results that aid in the formulation of hypotheses about how complex terrain features modify supercell evolution and morphology. Studies investigating multiple supercellular events in the presence of complex terrain further elevate these hypotheses through repeated observations in various locations of elevated terrain. From these studies we formulate our background knowledge of how supercells behave in the presence of complex terrain, which provides a benchmark on how we should expect simulated supercells to interact in our modeling simulations.

2.2.1 The Great Barrington, Massachusetts, Tornado on 29 May 1995

On 29 May 1995, a long-lived supercell was observed via WSR-88D throughout most of its life cycle, including interaction with several complex terrain features around western New York and Eastern Massachusetts. This storm produced a long track F3 tornado that significantly impacted the town of Great Barrington, Massachusetts (GBR). Bosart et al. (2006) explored this storm's radar characteristics and the associated terrain interactions in detail. The supercell that produced the GBR tornado initially ascended the Catskill Mountains; then, as it moved off the escarpment into the Hudson Valley, the rotational velocity observed by radar increased at all beam elevations (Fig. 2.1a). This enhancement was speculated to be a result of terrain-channeled 0-1 km southerly inflow through the Hudson Valley that then converged with northerly outflow surging down the escarpment (Fig. 2.1b). The collision of these two air masses was speculated to have generated a substantial source of baroclinic horizontal vorticity which could be stretched/amplified into the vertical by the storm's updraft. This would effectively enhance the low-level mesocyclone and associated storm-scale dynamics lead to the increasing the potential for severe weather.

The storm then became tornadic and maintained intensity as it continued across the Hudson Valley and approached the western foothills of the Taconic Range. As the storm ascended towards the crest of the Taconic Range, the mesocyclone rapidly weakened. This was co-located with a gap in the GBR tornado damage path, suggesting the increasing terrain elevation disrupted the low-level mesocyclone (Fig. 2.1b). The supercell survived the initial disruption and again became tornadic once it descended from the crest of the Taconic Range into GBR, where the most significant damage and fatalities occurred. The storm continued east and remained tornadic for a short time before dissipating. Ultimately, the analysis suggests that the

enhancements of the GBR supercell were likely a result of ample low-level convergence and vorticity produced by terrain-channeled flow (Bosart et. al. 2006).

2.2.2 Duanesburg, New York Tornadic Supercell on 22 May 2014

Complex terrain also played a significant role in modifying the mesoscale environment of another supercell that produced EF3 damage near Duanesburg, New York on 22 May 2014 (Tang et al. 2016). This event was unique as the synoptic-scale set-up did not suggest significant severe potential. As such, its isolated severe weather impacts were realized by mesoscale inhomogeneities induced by the terrain, as captured by the High-Resolution Rapid Refresh (HRRR) model. As described by Tang et al. (2016), an ageostrophic response to a north-to-south differential heating boundary resulted in strengthening upslope flow along the Adirondacks. This flow was channeled and accelerated through the Mohawk River Valley providing enhanced moisture, instability, and streamwise vorticity; this inflow enhancement is like the terrain-channeling in the Hudson Valley described by Bosart et al. (2006). As shown in Fig. 2.2, this favorable terrain-induced enhancement of the inflow environment resulted in the development of classic supercell radar signatures by 1947 UTC. Review of the Duanesburg supercell compliments the GBR analysis; this time including multiple datasets to verify terrain-induced environmental modifications impacted an observed supercell's intensity.

2.2.3 Tornadoes in the Great Tennessee Valley

Schneider (2009) explored three separate tornado events occurring around smaller geographic features in the Great Tennessee Valley to emphasize how these terrain features can result in localized increases in storm-relative helicity (SRH). In all three events, supercell updraft intensification was inferred to have occurred because of enhanced low-level convergence and upslope flow providing moist unstable inflow to the storms. One of the storms discussed in this

study, the Tazewell, Tennessee EF1 Tornado of 26 April 2007 appeared to be strongly influenced by a terrain bulge of the Cumberland Mountains, with peaks reaching about 1000 m. The timing of the storm ascending the Cumberland Mountain bulge overlaps with a period of intensification, suggesting orographic ascent aided in intensifying the updraft. The mountain shape also effectively trapped low-level moisture along a boundary which could have amplified the generation of baroclinic vorticity in a region characterized by low Lifting Condensation Level (LCL) heights, which are optimal for tornadogenesis (Thompson et al. 2003). A time-series of low-level rotational velocity derived from the KMRX radar suggests that this pre-existing horizontal vorticity was vertically tilted and stretched by the main updraft as it descended the higher terrain just before the Tazewell tornado formed (Fig. 2.3). Similar conclusions are drawn about terrain-induced environmental enhancements leading to tornadogenesis for two other events as well, though analysis of each is limited by spatiotemporal observations (Schneider 2009).

2.2.4 Supercells in the Blacksburg, Virginia WFO

Keighton et al. (2004) compared four supercells that traversed through the Blacksburg, Virginia WFO (KFCX) on 28 April 2002, only one of which became tornadic following interaction with the terrain (Fig. 2.4). Using radar and mesoscale analyses, they deduced that the tornadic supercell had both a stronger and deeper mesocyclone than the other three storms. Though there was no clear correlation between terrain and supercell intensity in this study, it is speculated that the tornadic supercell was amplified further through vortex stretching as it descended a leeward slope of the Blue Ridge.

Using a larger database of observed supercells within the Blacksburg WFO region, Prociv (2012) examined both geographic and meteorological data, using Geographic Information System (GIS) methodologies. This study investigated terrain and landcover influences of the Blue Ridge Mountains on low-level rotational velocities in 14 observed supercells occurring in KFCX between 1998 through 2011. The inclusion of a GIS framework with NEXRAD Level II radar data provided a solid methodology to explicitly correlate terrain features with storm-scale modifications that were largely subjective in prior literature. All 14 storms were tracked via radar, and their rotational values were compared and correlated with the terrain via mean elevation, slope, aspect, and landcover (Fig. 2.5a). Unsurprisingly, statistical analysis showed stronger rotational velocities when the terrain slope was smaller. When the slopes were stratified by aspect, results show that this inverse relationship was strongest along the westward facing slopes, which are generally characterized by drier and more stable environments. Qualitative comparison of elevation to rotational velocity highlighted eight cases of terrain-induced vorticity stretching leading to the amplification of the low-level rotational velocity as storms descended both southeasterly and northwesterly facing slopes (e.g., Fig. 2.5b). The strongest supercells were seen in the Piedmont region, which lacks significant terrain variability (Prociv 2012). Results were still limited due to the small sample size, but this study provided an excellent framework to further explore storm-scale relationships with terrain in our own study area which will be discussed in Section 2.5.2.

2.2.5 Terrain Influences during the 27 April 2011 Super Outbreak

A record-breaking tornado outbreak occurred throughout the southeastern United States on 27 April 2011. Nearly 200 tornadoes were spawned by several waves of quasi-linear convective systems (QLCS) and discrete supercells (Fig. 2.6). The event was largely driven by

an overlap of anomalous synoptic and mesoscale features that comprised one of the most conducive environments for violent tornadoes ever documented in scientific literature; several of these tornadoes occurred in the Southern Appalachians, including Alabama, Georgia, and Tennessee. An extensive review of the event by Knupp et al. (2014) showed a correlation between topographic variability and tornado intensity, with weaking observed as the tornadic circulations propagated upslope, and rapid intensification occurring on the downslope side (e.g., Fig. 2.7). Many of the tornadoes which occurred during the 27 April 2011 Super Outbreak appear to have initiated around the opening of southwest-to-northwest oriented valleys along the spine of the Southern Appalachians (Gaffin 2012). Surface winds in the Great Tennessee Valley were out of the southeast during the peak of the event, resulting in terrain-channeled accelerations through these valleys (Fig. 2.8). As discussed with the GBR and Duanesburg, New York tornadoes (Bosart et al. 2006; Tang et al. 2016), terrain-channeled inflow leads to amplification of low-level helicity which can be amplified and stretched by existing supercell updrafts to maximize tornado potential, especially in an already favorable environment.

2.3 Climatological Studies

To construct a conceptual model of supercell behavior in the region, we need a full understanding of both the low-level mesoscale environment that is modulated by the terrain, along with the synoptic-scale environment that conditions the atmosphere for the formation of these storms. Yet, a formal, comprehensive climatology of supercell thunderstorms for the Appalachian region does not currently exist. Several studies have explored sub-regions of the Appalachians and identified some climatological aspects of supercells. These studies provide some insight to the annual and diurnal cycles, severe weather impacts, and general meteorological patterns observed during supercellular events in the South-Central Appalachians.

Significant tornadoes (ST), those which produce F/EF2 + damage, occur more frequently in and around the southern Appalachian regions, compared to other areas of mountainous terrain, such as the Rockies (Fig. 2.9). We can use ST climatologies as a proxy for the missing Appalachian supercell climatology since STs are primarily produced by discrete supercells (Grams et al. 2012). Gaffin and Parker (2006) compiled a 54-year climatology of synoptic conditions associated with STs in the Southern Appalachian Region (SAR), including three distinct terrain features shown in Fig. 2.10. Spatial distributions show that STs are much more common on the southern and western sides of the Appalachians, with a notable decrease along the eastern flanks (Fig. 2.9). The temporal distributions of STs reflect the typical severe weather climatology, with a seasonal primary peak in the spring, a secondary peak in the autumn (Fig. 2.11), and a diurnal peak in the mid-to-late afternoon. The variable spatial distribution with respect to terrain invoked additional exploration on the synoptic scale environment across the SAR for ST events.

Synoptic-scale composite maps were constructed to analyze common patterns associated with ST events (Fig. 2.12). Composites show that a surface low is commonly located in the Ohio Valley. Surface analyses showed that ST events in the SAR were most often associated with pre-frontal troughs or cold fronts. Warm fronts and stationary boundaries were less common surface features associated with STs. No discernable differences in the surface patterns were found to be associated with the terrain features of the SAR, which highlights terrain-influences as more of a mesoscale process. Analysis of composite 500 hPa charts show STs are commonly associated with southwesterly flow ahead of a neutrally tilted trough, suggesting there is no significant discrimination of the upper-level trough tilt to ST events. One notable deviation is that northwest flow at 500 hPa was almost exclusive to summer ST events, though significant conclusions from

this are limited by a small sample size. Similarly, when analyzing upper-level jet streaks in relation to ST events there was no discriminator between the right-entrance or left exit-regions where the most favorable synoptic-scale ascent is found. However, it was noted that most ST event seem to occur on the right-side of the 300-250 hPa jet. Also, they compared composite ST events with ST Outbreaks (5+ ST events in a 12-hr period), and non-ST tornado events which showed that wind dynamics are much more important for ST events in the Appalachians than instability (Gaffin and Parker 2006).

The prior study provides synoptic-scale patterns associated with STs (and by proxy, supercells) in the south-central Appalachians. Supercells are mesoscale phenomenon, and therefore also are highly depended on the mesoscale environment in which they traverse. Katona et al. (2016) addresses how complex terrain influences mesoscale environmental heterogeneities throughout the Eastern United States by utilizing average convective day climatologies derived from the High-Resolution Rapid Refresh (HRRR) operational forecast model. They argue that the averaging of instability and wind shear parameters over numerous convectively favorable days will diminish synoptic and mesoscale variabilities not associated with the underlying terrain, thus emphasizing terrain-induced heterogeneity in the climatologies.

HRRR forecasts were collected during the warm season (1 February – 30 September) between 2013-2015 when Mixed-Layer Convective Available Potential Energy (MLCAPE) exceeded 500 Jkg^{-1} over 10% of the grid points over land. Identified days were binned by geographic region (Northeast vs. Southeast) and 10-m wind orientation (Southeasterly vs. Southwesterly), as the ground-relative flow dictates how the flow will move across the terrain. Climatology maps were generated for MLCAPE, 0-1 km SRH (both not shown), and a variant of the significant tornado parameter (STP) which combines, MLCAPE, 0-1 km SRH, MLLCL

heights, and 0-6 km bulk shear to parameterize tornadic environments (Fig. 2.13). A notable positive anomaly in the mean STP field occurs around the Hudson and Mohawk Valleys in New York for SW flow days, which supports the inference of terrain-induced environmental enhancements discussed in prior observational studies (e.g., Bosart et al. 2006; Tang et al. 2016).

Similar anomaly patterns were seen in the 0-1 km SRH climatology highlighting the role of low-level wind dynamics for favorable terrain-induced environmental perturbations. Numerous other anomalies are present in the climatologies as well, usually located around variable topography, such as coastlines, lakeshores, valleys, and ridges. Bootstrapped standard errors were computed to show that most of these mesoscale anomalies were statistically significant, further highlighting the importance of these findings. Additionally, while the HRRR can resolve larger-scale topographic influences, the 3-km grid resolution is insufficient to completely resolve storm sensitivity to the terrain-induced environmental modulations (Katona et al. 2016). Despite this limitation, this study improves our understanding of the mesoscale variability associated with favorable convective environments and terrain.

WFO-specific climatologies provide useful regional information regarding the presence of supercells, severe weather, and significant terrain. For example, Stonefield and Hudgins (2006) constructed a severe weather climatology for the Blacksburg, VA CWA (KFCX) between 1950-2005, making note regarding the role of orography, along with other typical forcing mechanisms in the development/modification of severe convection throughout KFCX. As expected, most severe convection occurred during the late spring and early summer months, with a peak diurnal frequency coinciding with peak surface heating hours. Tornado occurrence closely followed the typical diurnal pattern of severe weather, though they were favored more during the spring when vertical wind shear was stronger. April is the climatological peak for significant

tornadoes (F2 or higher) due to more frequent frontal passages enhancing vertical wind shear, which was also seen in the synoptic analyses from Gaffin and Parker (2006). It should be noted that most KFCX tornadoes occurred east of the Blue Ridge (Fig. 2.14), likely due to lee-side convergence and higher instability creating frequent tornadic environments in the Piedmont when compared to the Mountains. Hail events followed a similar climatology to tornadoes. Severe winds were the most recurrent severe weather events throughout KFCX, though they often occurred a bit later in the warm season. Most severe wind reports were associated with summertime mesoscale convective systems (MCS), suggesting wind reports may not be as useful for exploring supercell occurrences in the region.

Lane (2008) constructed a similar climatology for the Greenville-Spartanburg CWA (KGSP), though emphasized their analysis on significant tornadoes (ST) occurring over 60 different days between 1948-2006. The temporal and diurnal patterns remain unchanged in KGSP when compared to previously discussed tornado climatologies in the southern Appalachians. The synoptic climatology for STs in KGSP highlights the need for a juxtaposition of low-level wind shear and moisture transport, typically found in the warm sector of an extratropical cyclone, to be located over KGSP. This pattern is best-established when the surface low is located well to the north and west of KGSP, as south/easterly cyclones tracks increase the likelihood of cold-air damming, resulting in a statically stable boundary layer over the region. They also constructed composite proximity soundings via NCEP-NCAR reanalysis data which showed significantly lower instability parameters for STs when compared to distributions from Thompson et al. (2003). The one notable difference was 0-3 km CAPE which was usually comparable or larger than noted ST events in prior literature. It is becoming clear that environments supportive of supercellular convection in the south-central Appalachians are

largely dictated by favorable thermodynamics and wind dynamics in the lowest 3 km of the troposphere; the layer where terrain-induced perturbations will be most influential.

A notable climatological maximum of tornadic activity was identified around the southern end of the Appalachian Mountains in Northeast Alabama (Coleman and Dixon 2014; Lyza and Knupp 2018). A total of 79 tornadoes between 1992-2016 were identified in impacting a region of complex terrain associated with the Cumberland Plateau in Northeastern Alabama (Fig. 2.15); dubbed the Southern Cumberland System (SCS) in Lyza and Knupp (2018). These tornadoes were most frequent during the spring months, with a secondary peak during late autumn, which agree with previously discussed climatologies (Gaffin and Parker 2006; Stonefield and Hudgins 2006; Lane 2008). A diurnal analysis showed that SCS tornadoes occurred during all periods of the day, but a favored parent-storm mode signal existed for supercells during the mid-afternoon to evening hours, and QLCS favored overnight into the early morning hours. Lyza and Knupp (2018) also identifies several terrain-induced processes that appear to amplify tornado potential in convectively favorable background environments including channeled flow, and lower LCL heights over elevated terrain. These processes are often found along the northwestern slopes of Sand Mountain, where rapid intensification of storm-scale rotation is often observed. These findings further support the notion that low-level environmental modifications are key in developing/maintaining conducive environments for supercells in regions of complex terrain.

Reviewing existing regional severe weather climatologies has painted a clear picture of the synoptic and mesoscale ingredients required for supercells to occur around the south-central Appalachians (Gaffin and Parker 2006; Stonefield and Hudgins 2006; Lane 2008). The synoptic pattern for supercells in the Appalachians is characterized by a convectively favorable

juxtaposition of low-level wind shear and moisture in combination with upper-level dynamical support (Gaffin and Parker 2006; Lane 2008). This occurs most commonly during the mid-to-late afternoon in the spring months. Mesoscale variability in CAPE and SRH in the vicinity of complex terrain under varying surface wind orientations highlights the role of the terrain in the environmental modifications (Katona et al. 2016). Such variabilities have been seen in the observations to enhance supercell intensity which effectively allows it to persist through areas of complex topography (Bosart et al. 2006; Schneider 2009; Prociv 2012; Tang et al. 2016). Though it is still unclear exactly how supercells respond to these environmental modifications, and to what degree the terrain-induced enhancements play on storm-scale dynamics. As such, numerical modeling studies are required to explore these topics in finer detail.

2.4 Idealized Modeling Studies

Idealized numerical modeling of supercell thunderstorms has been a common method to conduct controlled experiments to explore storm dynamics and their sensitivities to various components of their environment. While many studies neglect terrain for simplicity, more recently, supercell modeling studies have begun to include complex terrain to understand its influences on convection and storm evolution (e.g., Markowski and Dotzek 2011; Soderholm et al. 2014; Smith et al 2016; Miglietta et al. 2017; Scheffknecht et al. 2017; Katona and Markowski 2021; LeBel et al. 2021). The main findings of these studies are summarized in the following two sub-sections, with 2.4.1 focusing on the results of studies where the terrain was highly idealized, and 2.4.2 focusing on the results utilizing more realistic terrain.

2.4.1 Simulated Supercells Interacting with Idealized Terrain

Markowski and Dotzek (2011; hereafter MD2011) is considered the seminal study corresponding to simulated supercell interactions with terrain. Utilizing Cloud Model 1 (CM1;

Bryan and Fritsch 2002), a highly idealized cloud resolving numerical model, they conducted multiple simulations of right-moving supercell thunderstorms interacting with a variety of idealized-terrain configurations (e.g., 500-m tall, 20-km wide hill; 10-km wide escarpment; 500-m deep, 15-km wide valley). Storms were initiated with three different surface wind profiles (easterly, calm, or westerly ground-relative winds with respect to the terrain). Each simulation is compared to a simulated supercell initialized in an identical environment without terrain. For relevance to the current study, we will focus on the results of the simulations including the 500-m hill. The air flow over the terrain in all simulations resulted in environmental modifications that modulated simulated supercell structure and intensity. The reader is advised to refer to MD2011 for additional information regarding results from other configurations.

In the three simulations involving the 500-m hill, terrain-induced environmental modifications result in heterogeneities in both thermodynamic and vertical shear profiles (see Figs. 2.16-2.17 for the easterly surface wind simulations with and without terrain); importantly, these environmental variations resulted in attendant impacts to supercell intensity. For example, weakening of the supercell's vertical velocity and vorticity were observed along the lee-side slope (relative to the surface wind) of the hill for both the easterly and westerly ground-relative wind simulations. This weakening was attributed to terrain-induced gravity waves modifying relative humidity (RH) in the 1-3 km layer, with subsidence leading to drier low-level layer on the leeside of the terrain, producing enhance CIN and a more convectively hostile environment (Fig. 2.16 e-g). For the easterly ground-relative wind simulation, the near-surface flow had a significant upslope component. This enhanced vertical shear by reducing near surface windspeeds, which effectively produced additional dynamic lift to aid in sustain the supercell as it ascended the terrain. The negative thermodynamic modifications appear to outweigh dynamic

enhancements due to increased low-level shear, resulting in the net-weakening of the supercell. In all simulations, terrain-induced horizontal homogeneities in vertical wind shear were shown to be vitally dependent on the ground-relative wind profiles.

The results of MD2011 were investigated further by Smith et al. (2016), using a similar methodology but also testing sensitivity to peak terrain height (500 m, 1000 m, and 1500 m). Results were primarily in agreement with MD2011; terrain-induced environmental variations in thermodynamic and kinematic quantities were present (e.g., Fig. 2.18) and had some impact on storm evolution. However, given the more substantial peak terrain altitude, Smith et al. (2016) found that terrain blocking effects played a larger role in modifying inflow and enhancing low-level vorticity along the gust front, which was thought to be more important for sustaining the simulated supercells in their simulations (Fig. 2.19). The development, structure, and intensity of analyzed simulated supercells for each of the three terrain configurations were reduced when compared to the control (no-terrain) simulated storm. The mountains effectively directed more inflow into the updraft resulting in more precipitation, and therefore a stronger cold pool to help maintain storms during their ascent uphill in the mountain simulations. During the 1500 m simulation, the cold pool became too strong and effectively undercut the updraft, which resulted in a weakening period until the storm was revitalized by leeside convergence as it descended the peak. Analysis also showed storm track sensitivity to terrain height, with higher terrain resulting in a larger shift to the left of the expected storm motion (Fig. 2.20). In summary, Both MD2011 and Smith et al. (2016) were pivotal studies that aid in our understanding of idealized supercell dynamics in the presence of complex terrain.

2.4.2 Simulated Supercells Interacting with Realistic Terrain

The utilization of realistic terrain helps to expand our dynamical understanding of supercell-terrain interactions due to a closer representation of observed events. This is particularly useful for constructing conceptual forecast models of supercell behavior in specific regions of complex terrain. Overall, simulated supercells with realistic terrain show similar modifications as those seen in the idealized studies (Scheffknecht et al. 2017; Miglietta et al. 2017; Katona and Markowski 2021; LeBel et al. 2021). A review of these studies provides a more realistic picture of the perturbed environments observed storms experience when interacting with complex and variable terrain.

Katona and Markowski (2021) took a unique approach by utilizing a numerical model to explore how realistic terrain modifies convectively favorable environments without initiating a simulated storm. Building on the results of Katona et. al (2016), they identified convectively favorable southwesterly and southerly flow regimes where environmental modification can occur due to terrain influences of Sand Mountain in Alabama. These regimes were then simulated in CM1 to isolate the effects of air flow over Sand Mountain in modifying the convective environment. Results of the idealized simulations were compared to the HRRR climatologies. It was implied that any pattern overlaps of severe weather parameters seen in both the HRRR climatologies and its corresponding CM1 simulation were a product of terrain-modified flow. The southwesterly flow simulations resulted in a large component of flow that is parallel to the simulated terrain of Sand Mountain producing minor environmental perturbations. The southerly flow simulation had a more perpendicular component of flow to the terrain, resulting in significant environmental modifications (Fig. 2.21).

Cross-terrain flow has been simulated and observed in generating terrain-induced perturbations in convective environments (MD2011; Smith et al. 2016; Tang et al. 2016; Lyza and Knupp 2018; LeBel et al. 2021). SRH within 0-1 km was amplified atop the Sand Mountain Plateau due to an increase in low-level vertical shear because of deceleration in the flow as surface parcels work against a statically stable environment to ascend the terrain (also seen in MD2011). Conversely, 0-1 km SRH decreased in the Tennessee Valley due to an acceleration of parcels descending the leeside of Sand Mountain in a uniform manner with height, effectively reducing the low-level wind shear. Perturbations in LCL heights were also well correlated with terrain height contours, with lower LCLs found at higher elevations. This suggests that near-surface parcels atop the plateau require less work to be lifted into the cloud base. High values of 0-1 km SRH and low LCL heights have been identified as key discriminators for significantly tornadic environments (Thompson et al. 2003). The overall results suggested that convective environments characterized by a large component of cross-terrain low-level flow are more likely to experience significant environmental perturbations. This has significant implications on the modulation of any severe convection which could occur in the perturbed environment.

LeBel et al. (2021) utilized the Weather Research and Forecasting model (WRF-ARW v3.9.1.1; Skamarock et al. 2008) to investigate the impact of a terrain-induced boundary on the intensification a tornadic supercell that impacted Mechanicville, NY on 31 May 1998. Idealized simulation results suggest that terrain-channeled flow through the Mohawk and Hudson Valleys forced the generation of a pseudo-dryline boundary. They note that this mesoscale boundary would have been undetectable in real-time during the event due to sparse observations within the affected region in 1998. As such, the modeled environment was evaluated with available surface and upper-air observations which ensured the analysis was based on an accurate representation

of the observed convective event. The environment to the east of the boundary, closest to Mechanicville, was exceptionally favorable for supercellular convection. The simulated supercell rapidly intensified shortly after interacting with the boundary as moist air containing strong streamwise vorticity was ingested to the updraft (Fig. 2.22). This study emphasizes the importance of terrain-features in the amplifying tornadic potential which was a common theme in observational studies as well (e.g., Bosart et al. 2006; Schneider 2009; Prociv 2012; Tang et al. 2016; Lyza and Knupp 2014, 2018).

Scheffknecht et al. (2017) utilized a numerical modeling with realistic terrain to investigate how the complex terrain of the Swiss Alps aided in maintaining a long-lived, discrete supercell on 2 August 2007. Three WRF simulations were run to investigate the impact of topography on both the airflow and simulated development of the supercell. The first simulation (C) is a control, utilizing realistic terrain that closely follows the topographic variability of the Alps in which the supercell was observed to traverse. The second (T1) utilizes idealized terrain which preserved the large-scale topographic variability while smoothing out the complexities seen in simulation C. The third (T2) includes a flat plateau elevated to 400 m above sea-level throughout the model domain. Comparative analysis of the three simulations provides insight to environmental and storm-scale sensitivities introduced by complex and variable terrain.

Simulation C results in a long-lived discrete supercell that closely followed observations from the 2 August 2007 event. Notable enhancements in the simulated supercell's intensity were co-located with enhanced CAPE and reduced CIN seen in valleys due to the channeling of warm moist air (Fig. 2.23a-b). These thermodynamic enhancements decrease in magnitude in T1 and T2 (Fig. 2.23c-f), highlighting the complexity of the terrain in realizing the enhanced convective environment. This helps explain why only simulation C can replicate the long-lived supercell

seen in the observations. T1 produces a short-lived supercell, while T2 produces a linear convective system. Differences in convective mode between the simulations is attributed to enhancements in vertical wind shear by the presence of the terrain. As such, it can be inferred that the topography also played a critical role in providing the necessary wind dynamics to support the long-lived supercell (Scheffknecht et al. 2017). These findings are critical as we see the environmental enhancements discussed in more idealized studies (MD2011; Smith et al. 2016) are playing a crucial role in emulating observed supercell behavior in more realistic models.

In summary, idealized numerical modeling studies have provided critical details regarding the relationship between supercell dynamics with complex terrain. Orography plays a significant role in modulating the thermodynamic environment through either gravity waves excited by cross-terrain flow or terrain-channeling. Whether or not these thermodynamic perturbations result in convective enhancements depends on the ambient low-level wind direction, the pre-existing convective environment, and peak terrain height (MD 2011; Smith et al. 2016; Scheffknecht et al. 2017; Katona and Markowski 2021). Similar patterns are seen with orographically modulated low-level shear, which can provide dynamical enhancements to storms traversing the underlying complex terrain. Though storm-scale dynamics are independent of the ground-relative wind profile, orographic enhancements are shown to be dependent to low-level flow orientation with respect to the terrain (MD2011; Katona and Markowski 2021). There also appears to be a goldilocks zone in which favorable thermodynamic and low-level shear modifications induced by orographic features can overlap to allow a storm to completely traverse a region of complex terrain. Alternatively, it is also seen that the dynamical enhancements can be outweighed by unfavorable thermodynamic terrain-induced modifications (MD2011). As such,

these studies raise just as many questions about orographic influences on supercells as they also answer. The relationship between the two vary depending on synoptic, mesoscale, and microscale features of both individual storms and the underlying terrain.

2.5 Observations of Supercells in the South-Central Appalachian Mountains

Thus far, the focus of this literature review has emphasized critical findings regarding the relationships between supercells and their environments to terrain from external peer-reviewed studies. The next two sub-sections are dedicated to examining the main findings of prior work directly related to the current study; these results are fundamental to the formulation of methodologies in the current work. Both studies, McKeown (2021) and Purpura et al. (2022) developed and analyzed a dataset of 62 discrete supercells that traversed and interacted with the South-Central Appalachians region between 2009-2019. Supercells were stratified by their ability to survive crossing complex terrain features of the Appalachians (Fig. 2.24a) or not (Fig. 2.24b), with a total of 25 crossers and 37 non-crossers. Section 2.5.1 discusses the climatology of the 62 supercells and how it relates to the previous climatological studies within the study region. Section 2.5.2 discusses and compares the environmental evolution of these crossing and non-crossing supercells. Section 2.5.3 discusses and compares the radar characteristics of the same supercells.

2.5.1 Climatology of Observed Supercells in the Appalachians

Climatological analyses of the 62 observed supercells from McKeown (2021) and Purpura et al. (2022) closely follow results discussed in Section 2.3 (e.g., Gaffin and Parker 2006; Stonefield and Hudgins 2006; Lane 2008). As in the prior climatologies, supercells were most common between April and May regardless of crossing status (Fig. 2.25). The consistent springtime seasonality between multiple climatological studies stresses the importance of vertical

wind shear for supercell occurrence around the Appalachians. This is particularly evident by the shift in storm tracks between spring and summer months, consistent with seasonal transitions in the upper-level height patterns and jet stream (Fig. 2.25c). Storms also tended to occur in daily clusters, meaning forecasters usually had multiple supercells to address during a single event. Similar diurnal cycles from prior studies are seen as well with storms forming in the late afternoon and persisting into the overnight hours (Fig. 2.26), emphasizing the role of peak heating for supercell development. Crossers tended to initiate earlier and dissipate later than the non-crossers, suggesting stronger dynamical influences, such as upper-level jet streaks (Gaffin and Parker 2006), were at play during crossing events.

Non-crossers were more likely to become linear at the end of their lifecycle, while crossers were more likely to dissipate as an isolated cell (Fig. 2.27). This is likely due to terrain-influences disrupting the storm dynamics, along with faster storm motions keeping crossers ahead of organized squall lines. Severe hail and winds were the most common impacts from the supercells, regardless of crossing status. Most of the tornado reports were associated with crossers, again suggestive of stronger dynamics in these cases (Fig. 2.28). Approximately 19% of the dataset were associated with the 27 April 2011 Super Outbreak. Results were tested for robustness when the outbreak was removed. Overall, the climatological results remained consistent even when the outbreak was removed (e.g., Figs. 25-26, and 28). The consistency and robustness of the climatological results from these studies with prior work is reassuring given the small sample size in which these conclusions were drawn from. (McKeown 2021; Purpura et al. 2022).

2.5.2 Environmental Evolution of Observed Supercells in the Appalachians

Purpura et al. (2022) explored both the synoptic patterns and inflow environments associated with the stratification of crossing and non-crossing supercells. Overall, the large-scale set-up indicated that crossers tend to have stronger dynamic support than non-crossers. This was evident as crossers more frequently occurred near the right entrance of the upper-level jet, with a negatively tilted 500 hPa trough, an 850-hPa low-level jet, and were initiated near a cold front (Fig. 2.29a). This synoptic set-up was also seen with ST outbreaks in Gaffin and Parker (2006). In contrast, non-crossers were more common with positively tilted 500 hPa trough, a weaker 850 hPa low-level jet, and initiated near a warm front or stationary boundary (Fig. 2.29b), which resembles the weaker tornado events from Gaffin and Parker (2006). Composite near-inflow soundings were constructed via the RAP/RUC model analyses at three key points during each supercell's lifecycle: upstream of the Appalachians (representative of initiation), peak elevation, and downstream of the Appalachians (representative of dissipation). These soundings, shown in Fig. 2.30, form the basis of the model environment used in the current study; see more details in Chapter 3. Statistical analyses to identify significant differences between crossing and non-crossing environments revealed that, overall, parameters associated with the wind profile, rather than the thermodynamic profile, were better discriminators between crossing and non-crossing supercells.

Low-level (i.e., 0-1 and 0-3 km) bulk shear and SRH were among the most significantly different parameters between crossing and non-crossing supercells (Fig. 2.31). Crossers generally had more available low-level SRH than non-crossers, especially as they moved from the upstream point towards the terrain peak. Physically, this emphasizes the role low-level wind dynamics play in maintaining supercell mesocyclones as they cross complex terrain, as discussed

in previous studies (Schneider 2009; Smith et al. 2016; Scheffknecht et al. 2017; Lyza and Knupp 2018). Subtle changes in 0-6 km bulk shear were seen across storm stratifications stressing prior inferences that the 0-3 km layer is more important for terrain-induced modifications (Gaffin and Parker 2006; Lane 2008; Schneider 2009; MD2011; Katona and Markowski 2021). While few thermodynamic parameters were statistically significant, one notable trend was the presence of drier mid-level air for non-crossers, especially at the peak and downstream locations, suggesting updraft entrainment and/or enhanced downdrafts may lead to an early demise. Instability parameters did not show significant discrimination between crossers and non-crossers (Purpura et al. 2022).

2.5.3 Radar Characteristics of Observed Supercells in the Appalachians

An in-depth analysis of the Doppler radar characteristics of the 62 supercells as they passed within 60 nautical miles of one of six WSR-88Ds located within the study area (Fig. 2.26) was performed by McKeown (2021). General trends in radar-derived parameters suggest crossers are more intense than non-crossers. Physically, this makes sense given the more favorable wind shear and thermodynamics quantified in crossing environments from Purpura et al. (2022). Crosser parameters also exhibited more variability which is likely a consequence of more frequent/prolonged terrain interactions. Such variability is highlighted in prior studies as well stressing the complex relationship between the individual storm and terrain (e.g., Keighton et al. 2004; MD2011; Prociv 2012; Scheffknecht et al. 2017). Doppler velocity and velocity-derived products, such as Mesocyclone Depth, Diameter, Intensity, and Normalized Rotation (NROT), exhibited the best discriminators between crossers and non-crossers (Fig. 2.32). Larger, wider, and more persistent mesocyclones were seen with crossing storms (as inferred by Keighton et al. 2004). The significant difference in the mesocyclone parameters remained even with the removal

of the 27 April 2011 outbreak. Classic supercell radar signatures (e.g., hook echoes and/or bounded weak echo regions) along with tornadogenesis on the upstream side of the mountains were more frequent with crossing storms.

2.6 Summary

The aforementioned studies provide the basis for our current understanding of terrain-influences on supercell structure and intensity. Observed case studies have highlighted the incredible complexities of terrain-storm interactions which are usually exacerbated by limited spatiotemporal observations. For example, terrain-induced storm-scale modifications play a key role in enhancing severe weather potential (e.g., Bosart et al. 2006; Schneider 2009; MD2011; Smith et al. 2016; Tang et al. 2016; Scheffknecht et al. 2017; LeBel et al. 2021). Additionally, terrain-induced effects such as vortex stretching may also be key (e.g., Keighton et al. 2004; Bosart et al. 2006; Schneider 2009; Prociv 2012; Tang et al. 2016). In all the observational studies, there is a call for future work to isolate terrain-induced influences on these storms through the usage of a high-resolution idealized numerical model (Keighton et al. 2004; Bosart et al. 2006; Schneider 2009; Gaffin 2012; Prociv 2012; Lyza and Knupp 2014, 2018; McKeown 2021; Purpura et al. 2022).

Idealized modeling studies have been pivotal to filling in the gaps from the limited observations of supercell-terrain interactions. The seminal work of MD2011 using idealized terrain highlighted the importance of terrain-induced environmental heterogeneities and their impact on storm evolution, while Smith et al. (2016) confirmed that the terrain itself can be impactful via blocking/channeling effects and orographic enhancements. The incorporation of more realistic terrain has further supported the findings of MD2011, indicating that maintaining

an environment supportive of convective maintenance is key (Scheffknecht et al. 2017; Katona and Markowski 2021; LeBel et al. 2021).

The recent work of McKeown (2021) and Purpura et al. (2022) provided the observational foundation for the present modeling study. They have demonstrated that terrain effects and terrain-induced environmental variability are both important for anticipating supercell evolution/intensity in the south-central Appalachians. Yet, the observations were spatiotemporally limited; thus, additional exploration using an idealized modeling framework is warranted. The environmental analyses of Purpura et al. (2022) were spatially limited to three locations along the storm tracks. McKeown (2021) exhibited spatial limitations due to data degradation and increasing elevation of the radar beam as one moves away from the radar site. Both studies are temporally limited by the available observations for their analyses. As such, we still have a limited understanding on how the complex terrain of the Appalachians acts to modulate supercell structure and the timescales on which these modulations occur. Numerical modeling acts to fill in these gaps by providing high-resolution spatiotemporal data regarding the inflow environment and intensity of simulated supercells interacting with the Appalachian Mountains. With such data we can explore storm-scale and environmental sensitivities to the variable terrain in greater detail to solidify their conclusion. Then the results from all three studies can be combined to formulate a conceptual model to aid in forecasting supercells which cross the Appalachian Mountains in an operational setting.

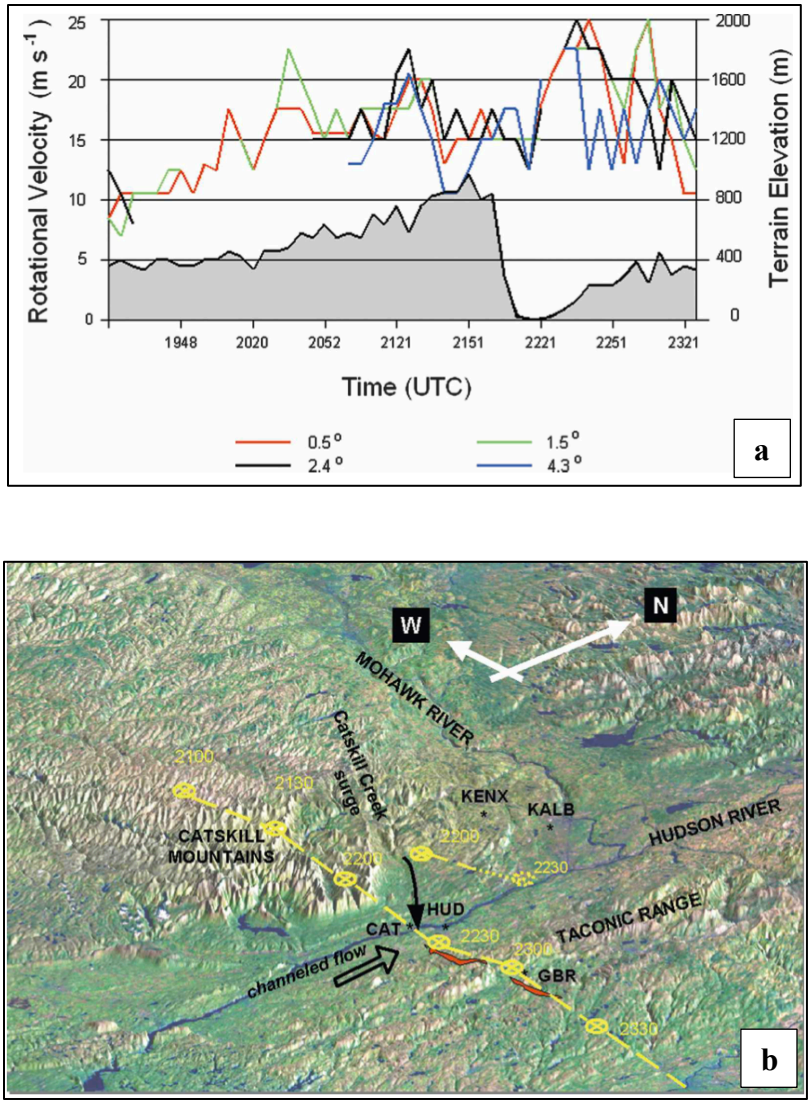

Figure 2.1: (a) time-series of radar-derived velocities of the GBR Supercell at four beam elevation angles vs. terrain elevation during the temporal period in which it traversed the Catskill Mountains and Hudson Valley. This provides a quantitative assessment of the terrain-induced amplification of the mesocyclone; and (b) a map displaying the GBR supercell storm track (yellow) overlaid on top of topographic features it interacted with over its life cycle. Channeled Flow and an Outflow Surge are annotated to highlight their role in the amplification of the supercell. The GBR tornado track (red) begins shortly after emphasizing this terrain-related process in modifying the rotational velocity of the storm (From Bosart et. al. 2006).

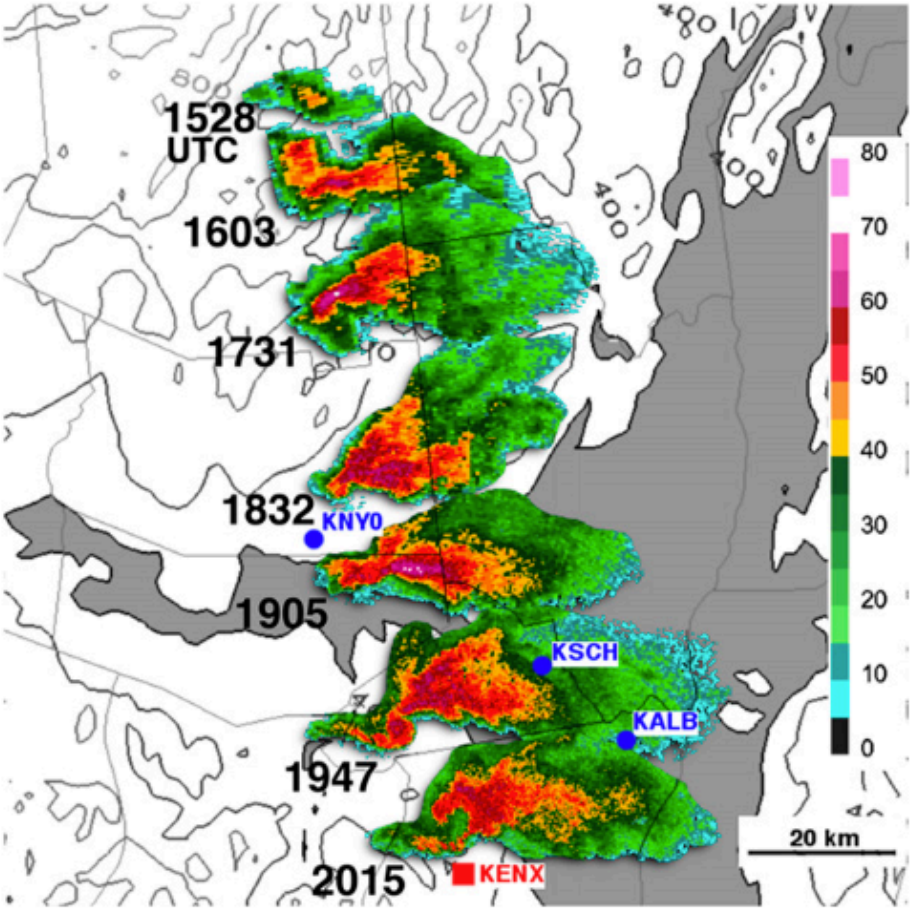

Figure 2.2: A time-series of radar reflectivity of the Duanesburg, New York Tornadic Supercell on 22 May 2014 overlaid on terrain contours. Elevation below 200 m is filled in grey to emphasize the Mohawk (West-to-East) and Hudson (North-to-South) Valleys. The storm clearly evolves into an intense supercell as it ascends the southern slope of the Mohawk Valley between 1905 and 1947 UTC. Key surface observation stations (blue) and the NEXRAD radar site (red) are also included (From Tang et al. 2016).

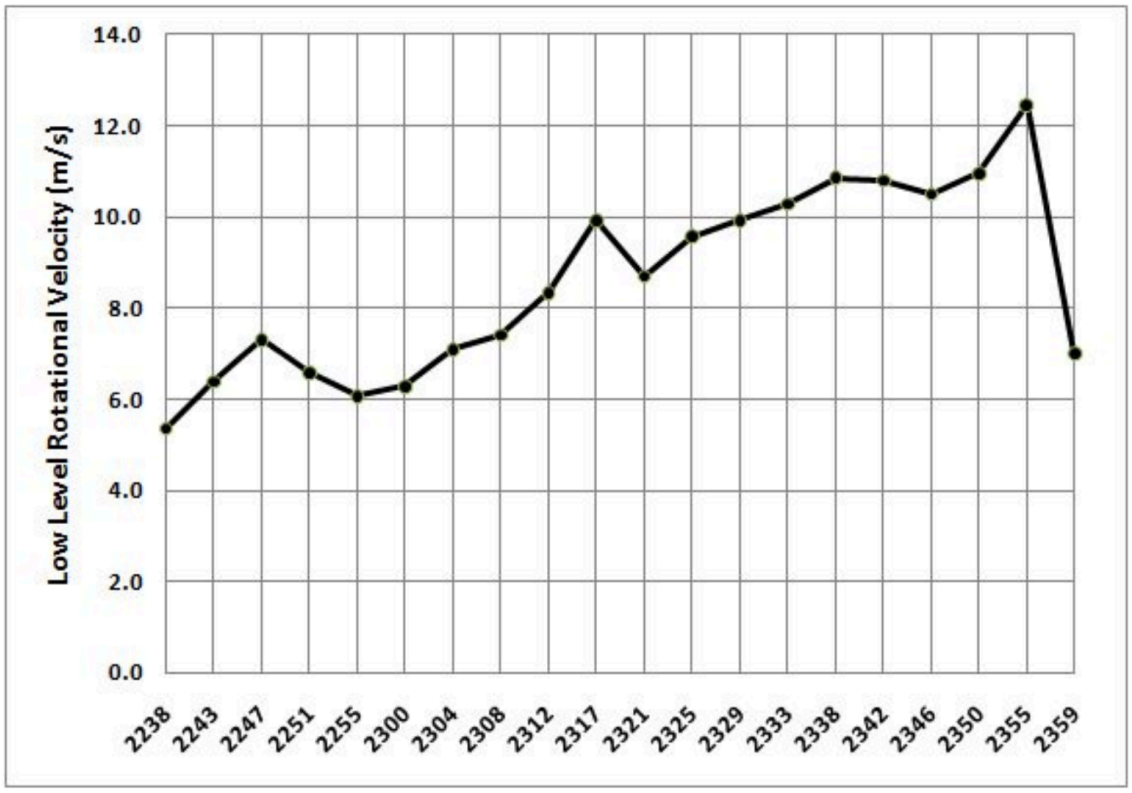

Figure 2.3: A time-series of the low-level rotational velocity derived from the KMRX radar while the Tazewell, Tennessee supercell traversed the Cumberland Mountain bulge. Rotational velocity continues to increase after 2300 UTC once the storm moves off the terrain (From Schneider 2009).

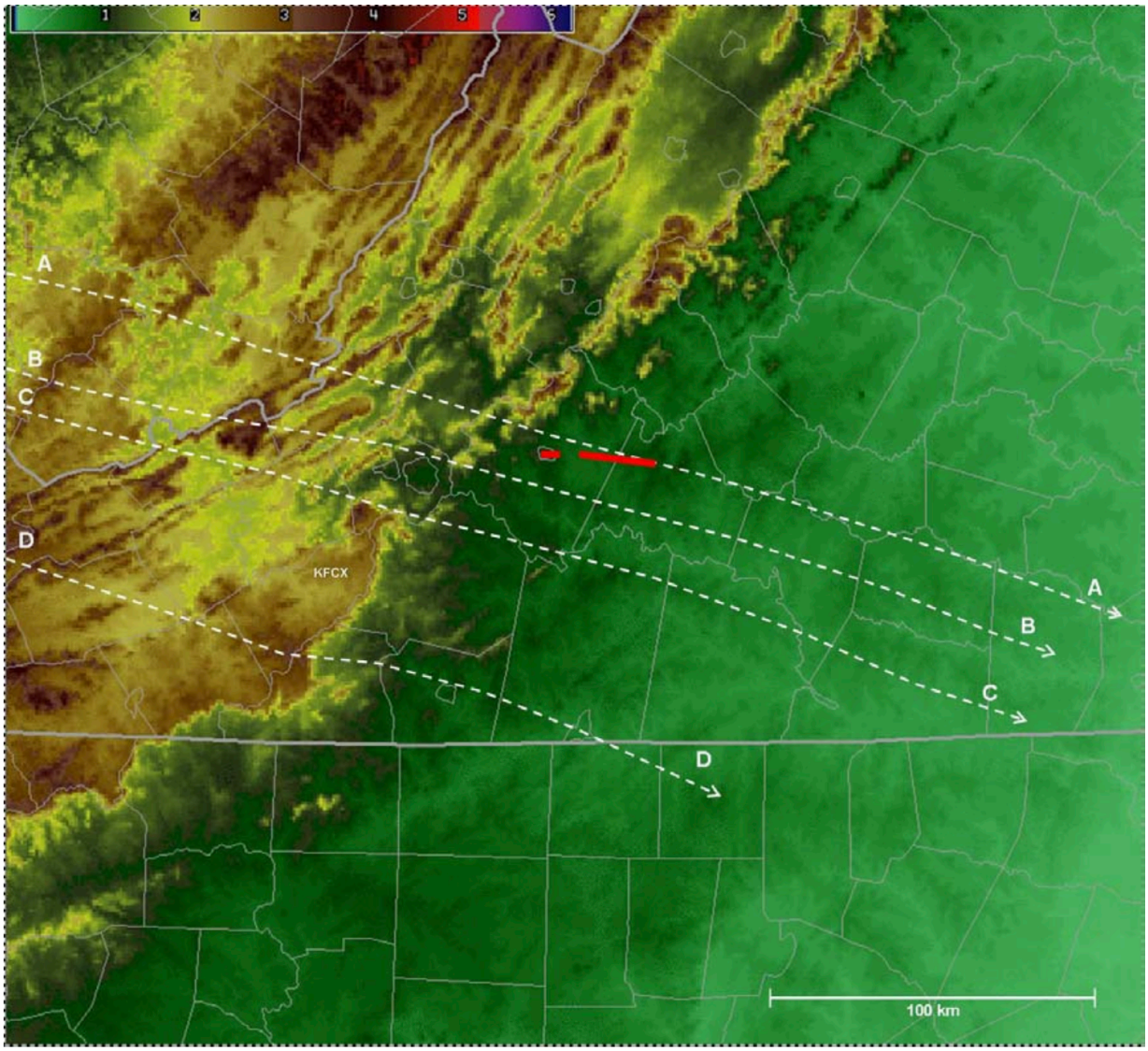

Figure 2.4: Tracks of the mesocyclones (dashed) associated with the four supercells that traversed KFCX on 28 April 2002. Two tornado tracks associated with Supercell A are shown in red. These tracks are overlaid on terrain to examine potential terrain influences on each storm (From Keighton et al 2004).

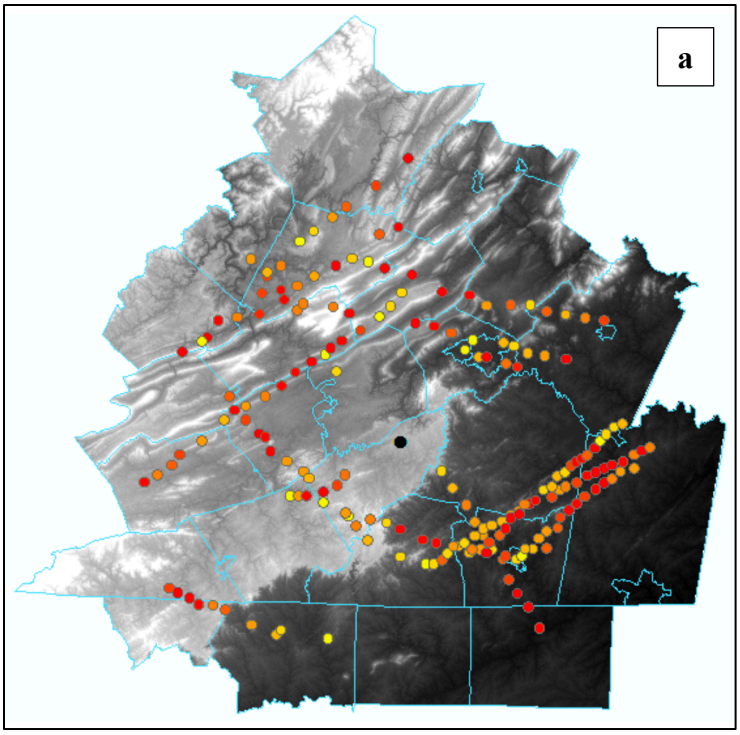

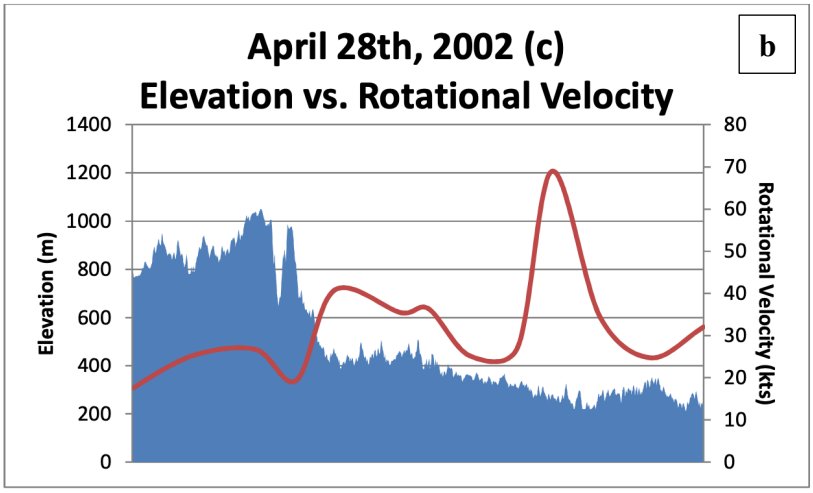

Figure 2.5: (a) Storm track points of all 14 supercell from Prociv (2012). The points are symbolized by rotational velocity magnitude where weaker rotational rates are shown in yellow with orange and red representing stronger rates; and (b) the terrain profile overlaid with the average rotational velocity of a supercell occurring on 28 April 2002. The rotational velocity clearly exhibits a sharp increase as the storm descends the elevated terrain.

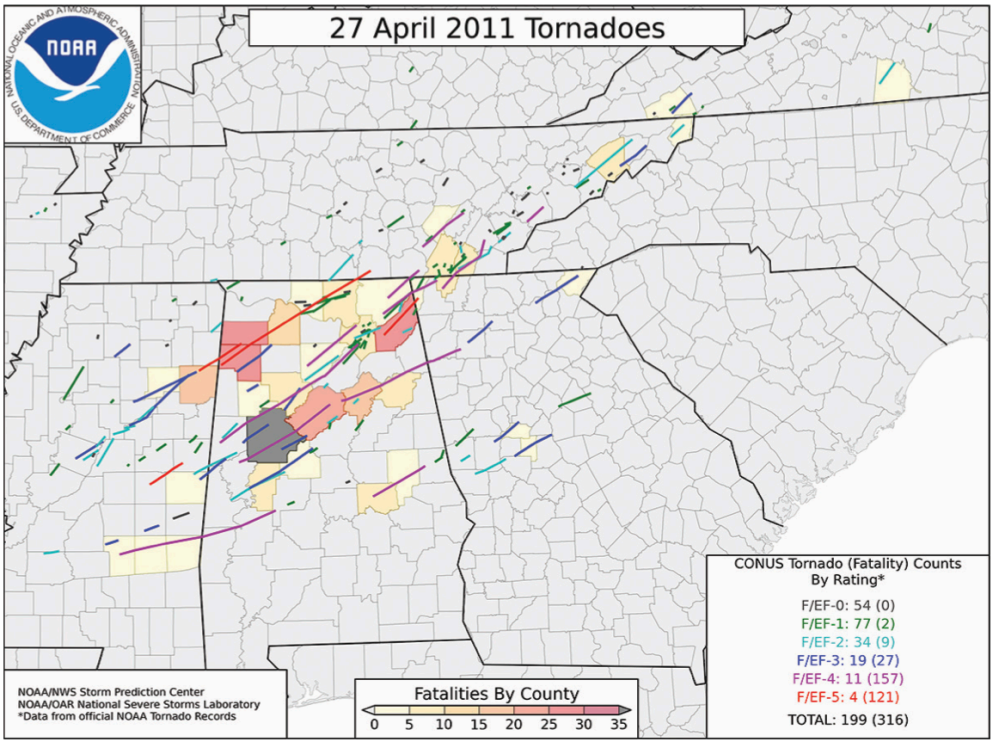

Figure 2.6: Tornado tracks from the 27 April 2011 Super Outbreak. Tracks are colored by EF-Scale rating and Fatalities by County are shaded to emphasize the significant impacts of this event (From Knupp et al. 2014).

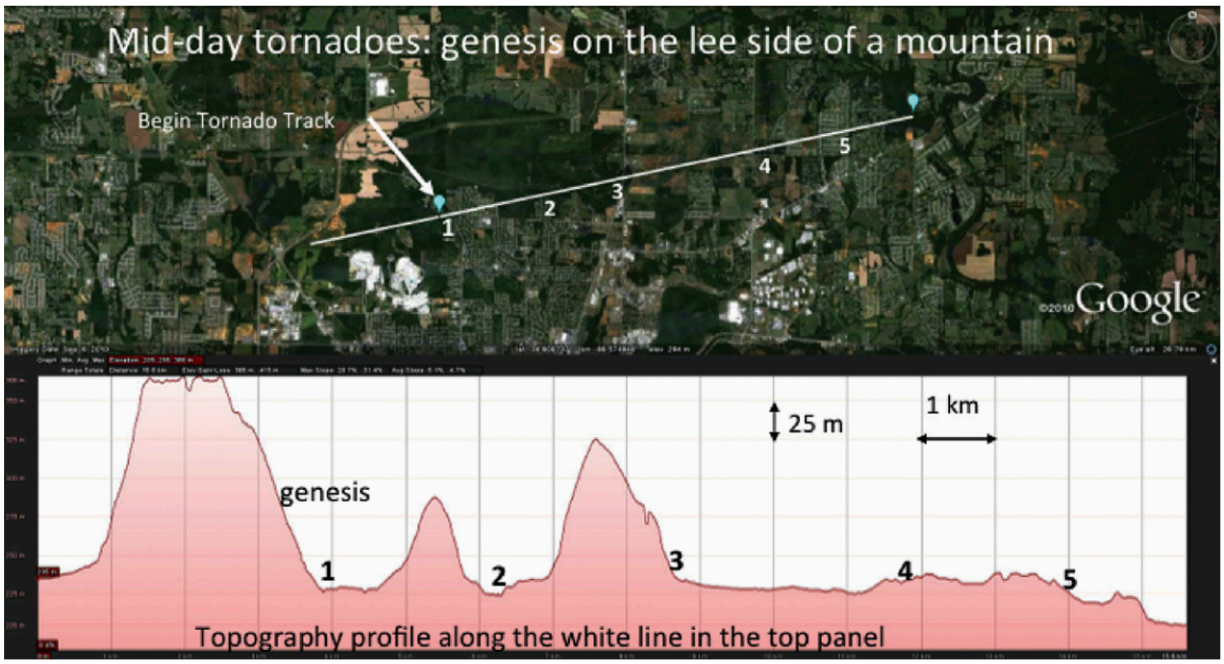

Figure 2.7: An example of potential topographic influences on tornadogenesis during the 27 April 2011 Super Outbreak. An EF-1 Tornado formed downslope of the largest terrain feature and exhibited intensification along additional downslope regions as inferred via damage surveys (From Knupp et al. 2014).

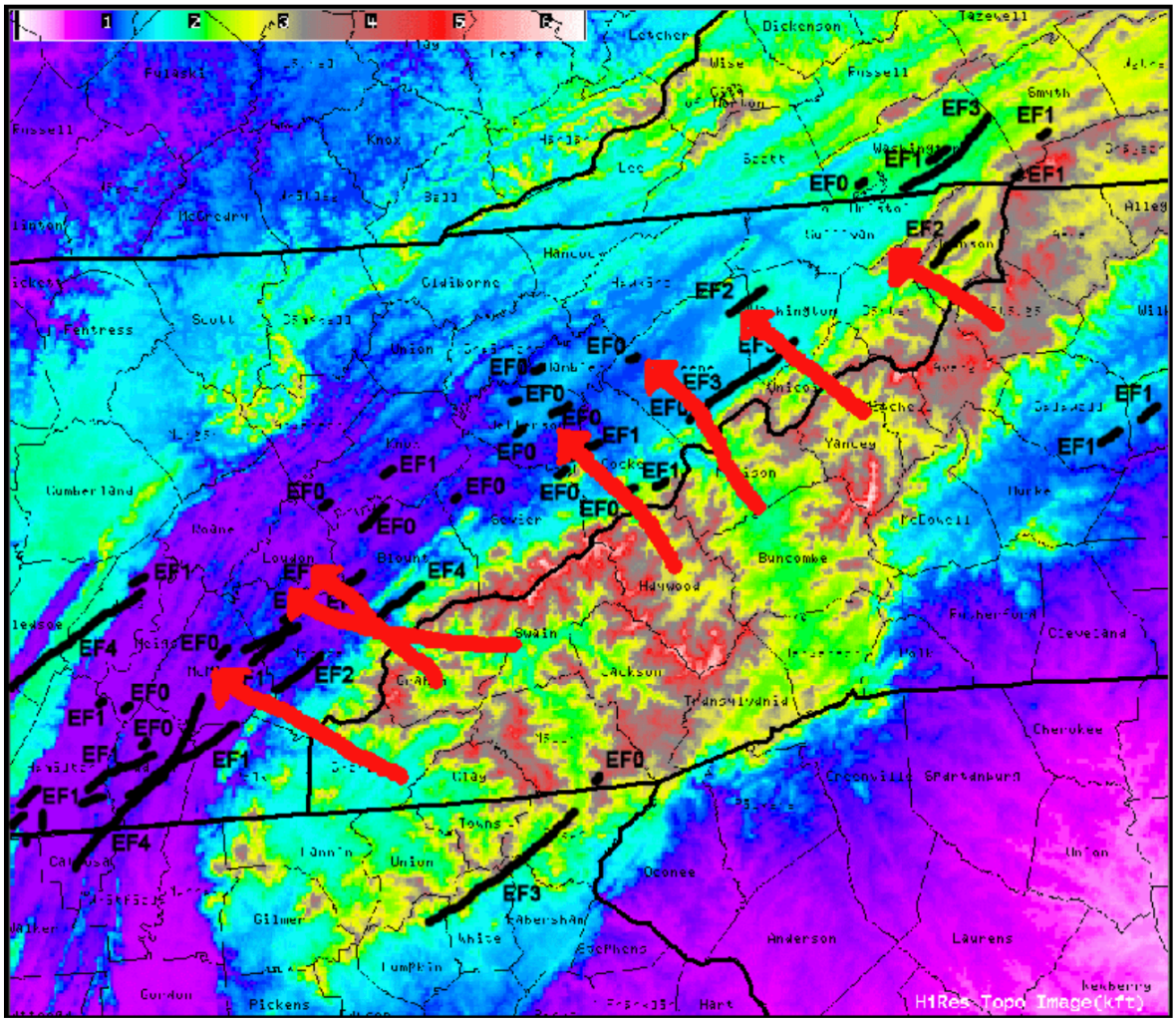

Figure 2.8: Topographic features of the Southern Appalachians overlaid with tornado tracks from the 27 April 2011 Super Outbreak. The red arrows have been annotated to highlight the path of terrain-channel flow in relation to the initiation points of multiple tornado tracks (From Gaffin 2012).

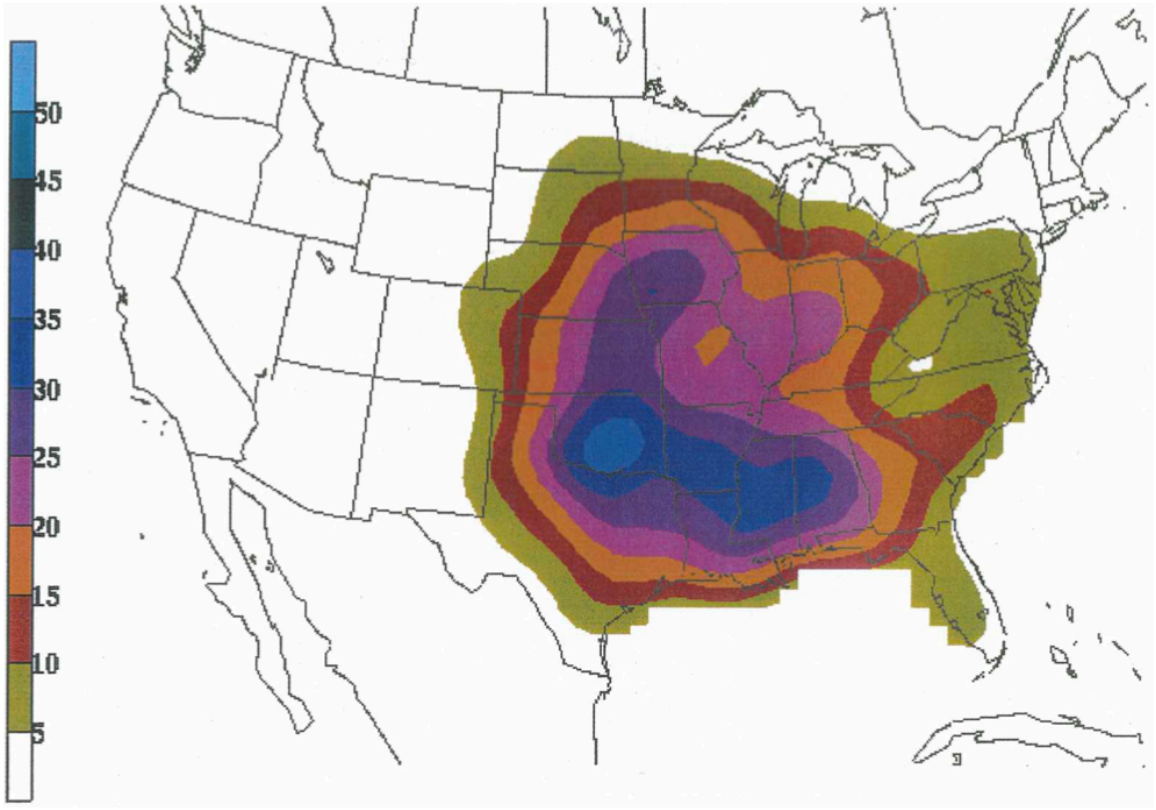

Figure 2.9: Mean number of days per century with at least one significant tornado (F/EF-2 +) event based on data from 1921-1995 (From Gaffin and Parker 2006).

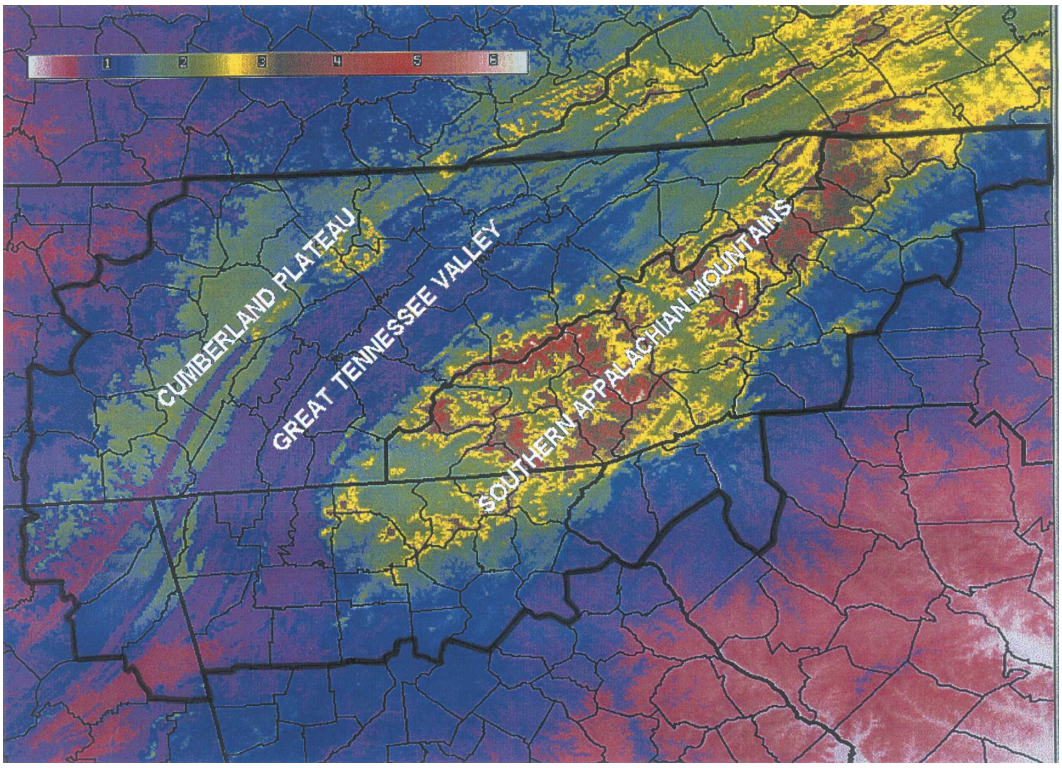

Figure 2.10: The geographic region denoted as the Southern Appalachian Region (SAR) in Gaffin and Parker (2006).

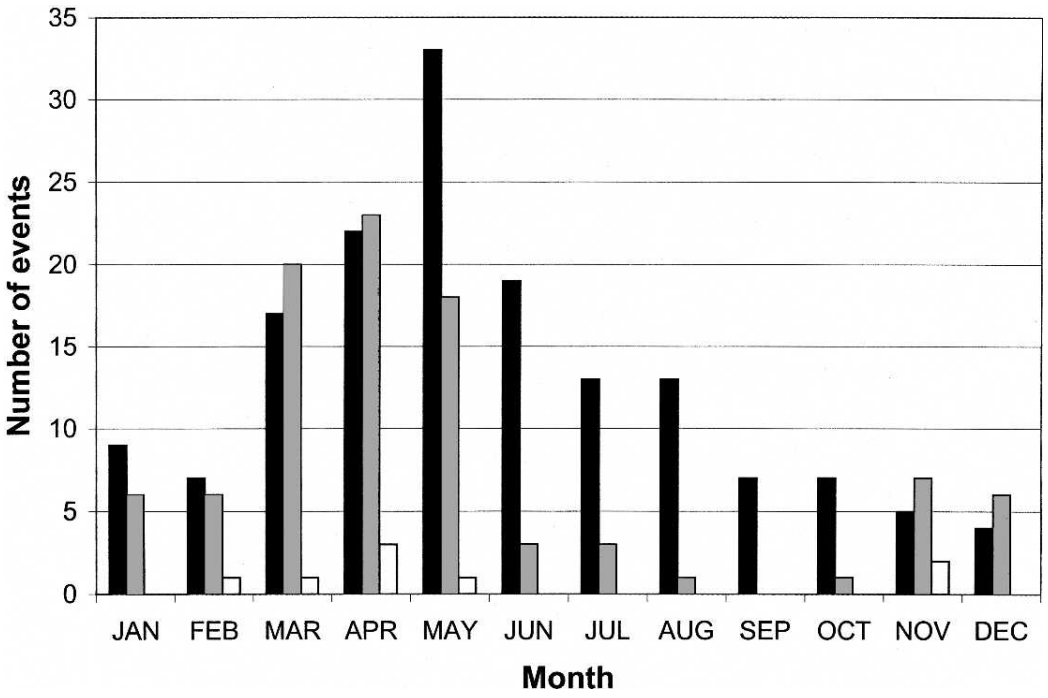

Figure 2.11: Monthly distributions of weak (black bars), significant (gray bars), and outbreak (white bars) tornado events occurring in the SAR between 1950-2003 (From Gaffin and Parker 2006).

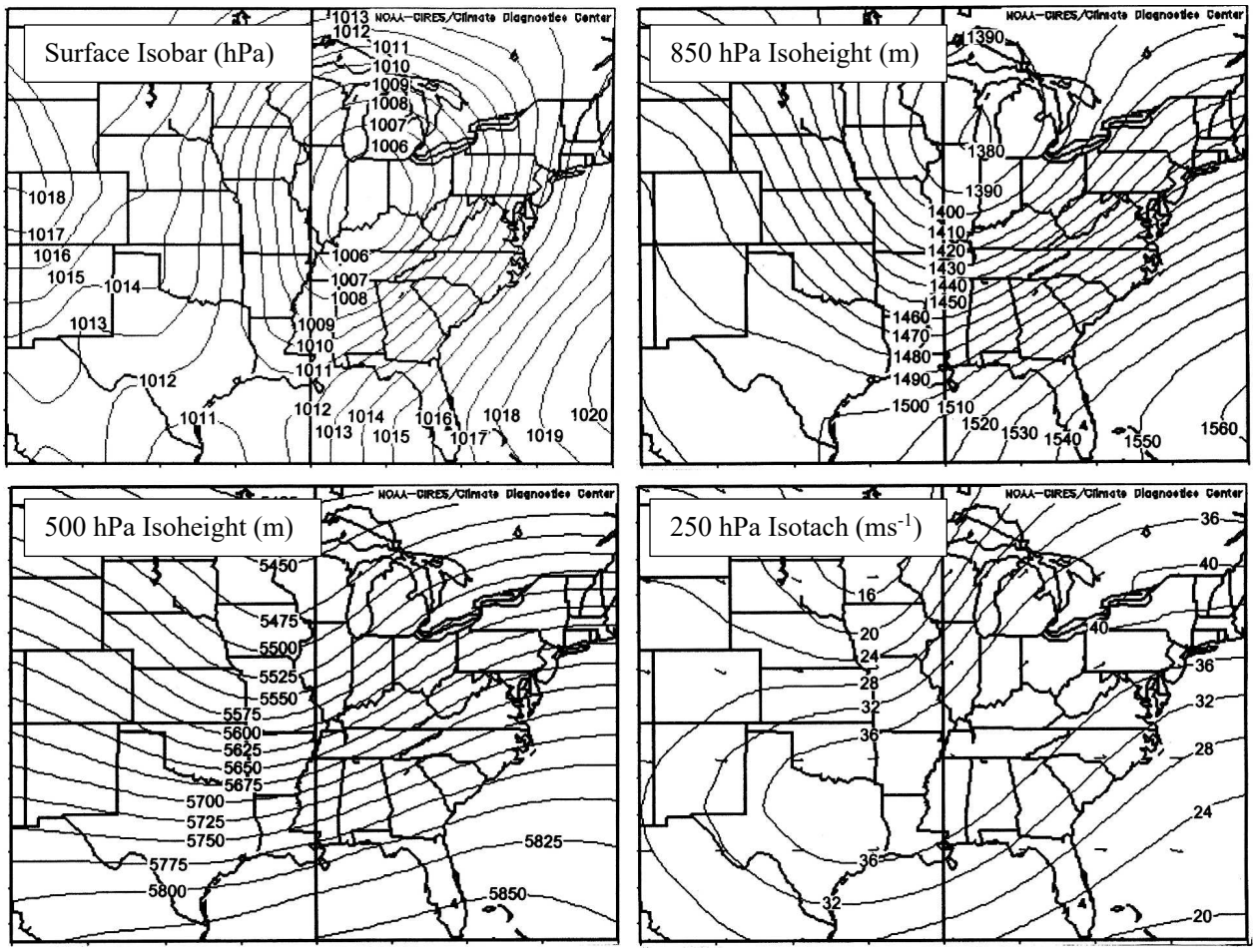

Figure 2.12: Composite synoptic maps of significant tornado events across the SAR (adapted from Gaffin and Parker 2006).

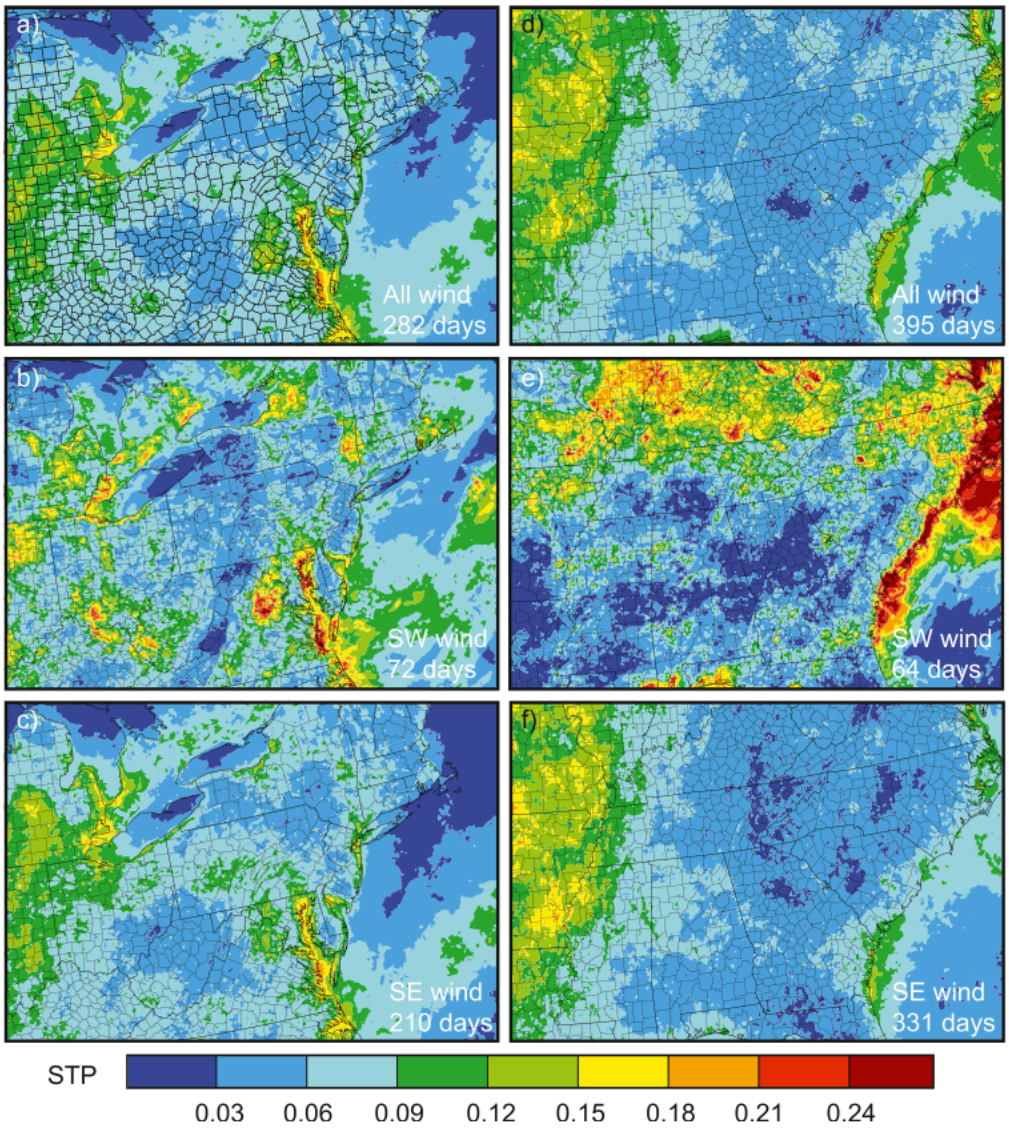

Figure 2.13: Mean Significant Tornado Parameter (STP) values derived from the HRRR for all convective days between 2013-2015 defined in Katona et al. (2016). The mean STP field is stratified by location in Northeast (left), Southeast (right), 10-m southwesterly flow (b), (e) and 10-m southeasterly flow (c), (f).

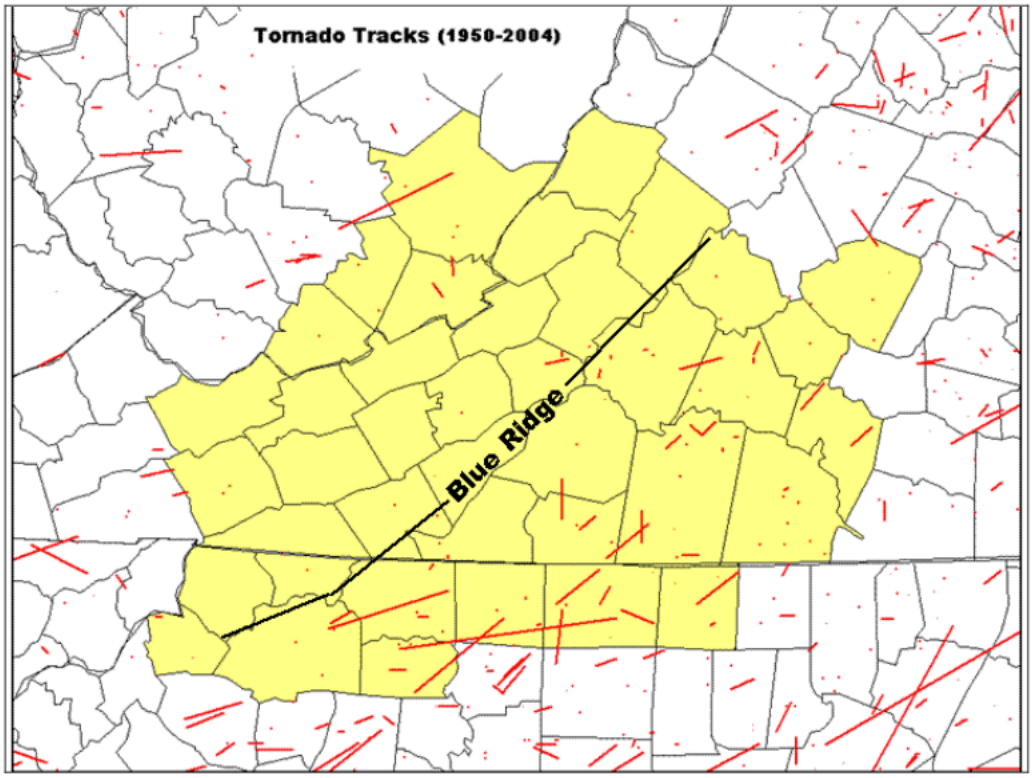

Figure 2.14: Historical tornado tracks between 1950-2004 from the Storm Prediction Center. The Blacksburg, VA CWA is highlighted in yellow. The spine of the Blue Ridge Mountains is annotated to highlight the relationship between tornado tracks and terrain (from Stonefield and Hudgins 2006).

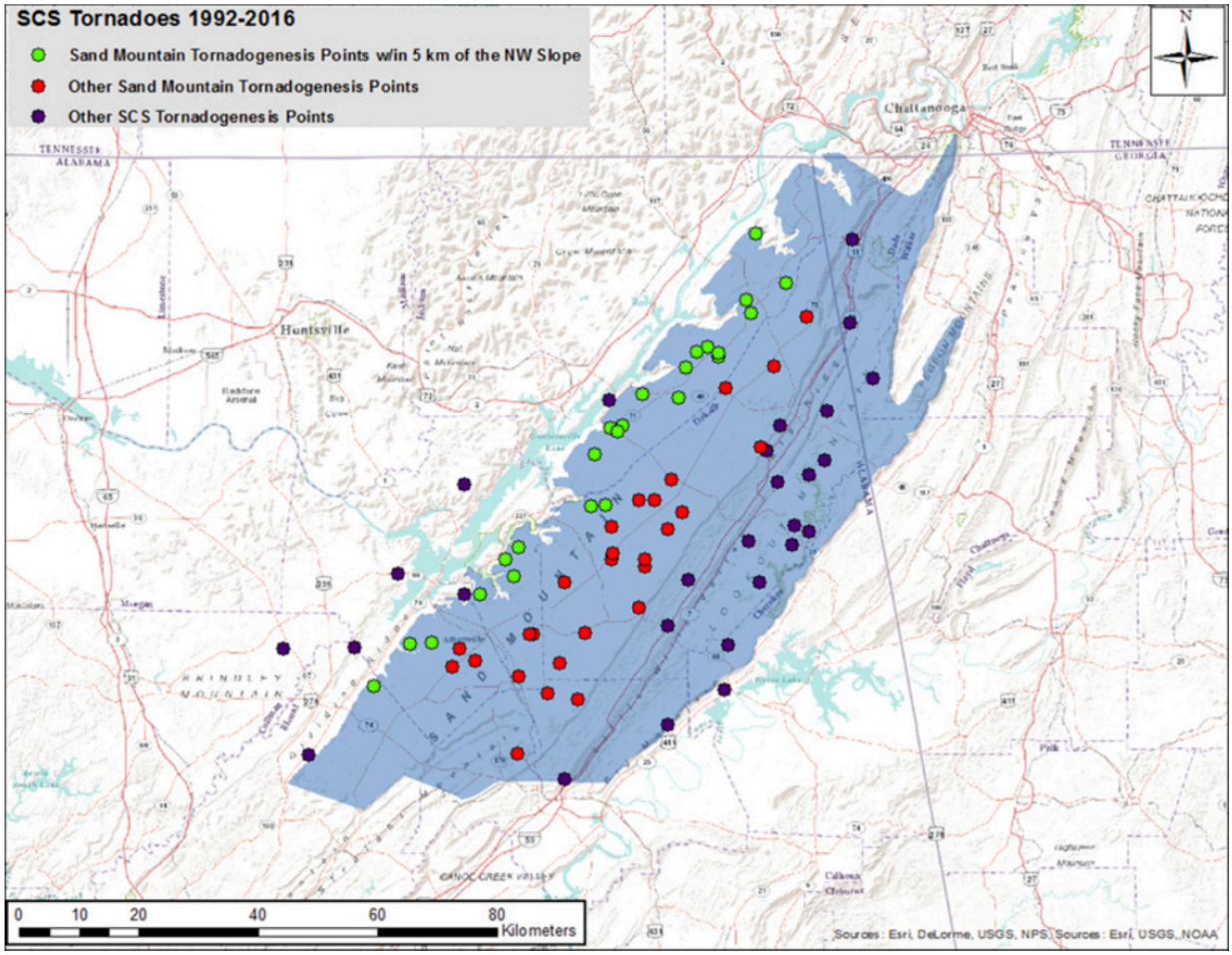

Figure 2.15: The initiation points of all tornadoes that impacted the SCS between 1992 through 2016. The points are colored based on the relationship with to the topography with red dots being associated with initiation points on top of Sand Mountain, Green dots being associated with initiation points on top of Sand Mountain that are within 5 km of a NW facing slope, and purple dots being associated with initiation points that impacted the SCS but did not form on Sand Mountain (From Lyza and Knupp, 2018).

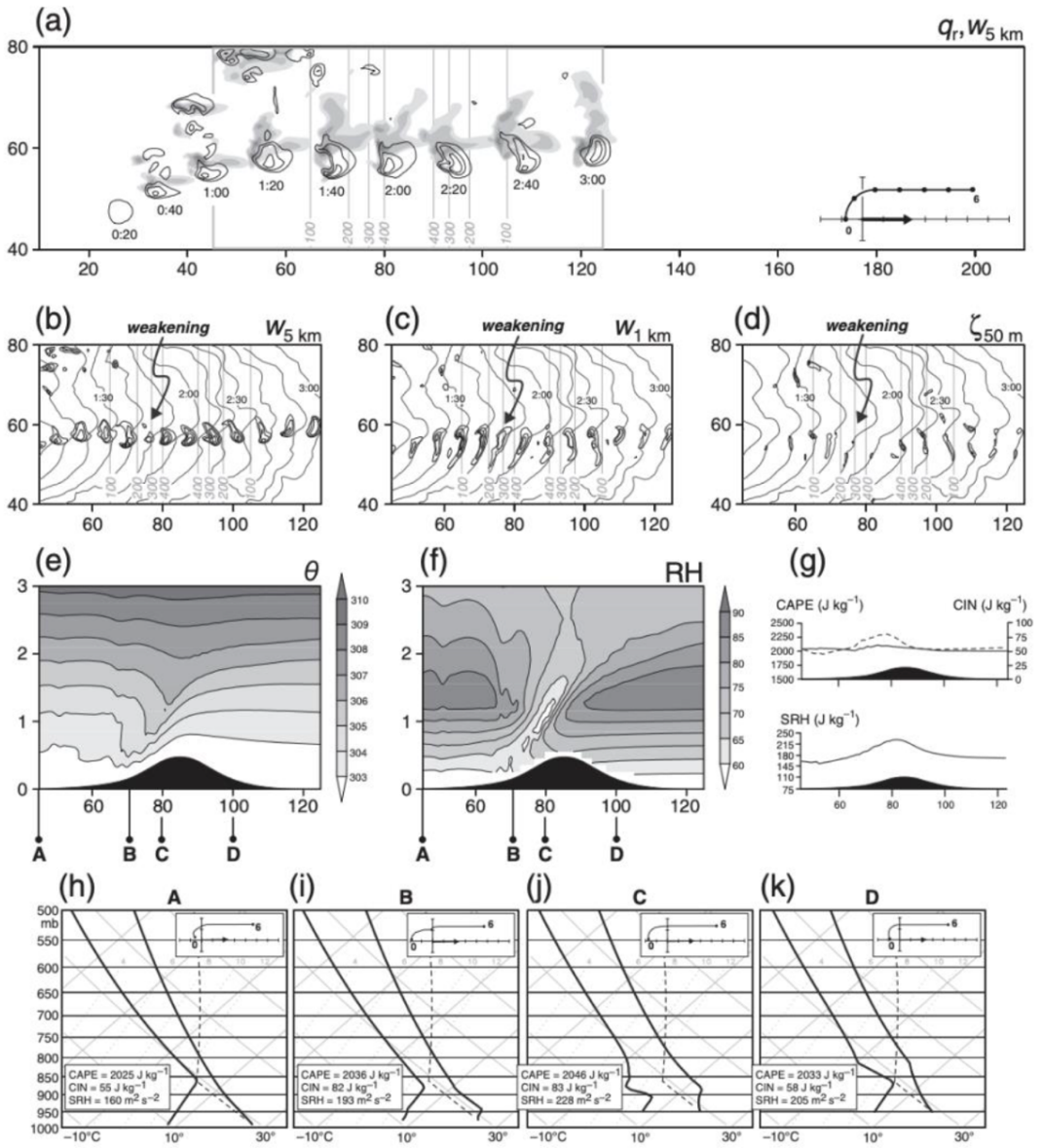

Figure 2.16: Visualized model output of a simulated supercell with easterly surface winds interacting with an idealized-bell shaped 500-m hill. Sub-plots (a-f) summarize variables to the simulated supercell and its inflow environment over 20 min intervals. An apparent weakening is noted around the 80-minute mark (b-d) which is attributed to an increase in CIN due to environmental modifications by the terrain (g-k) which were result from simulations without convective initiation to isolate terrain-influences. (Reproduced from Markowski and Dotzek 2011; See original paper for detailed description of individual sub-plots.)

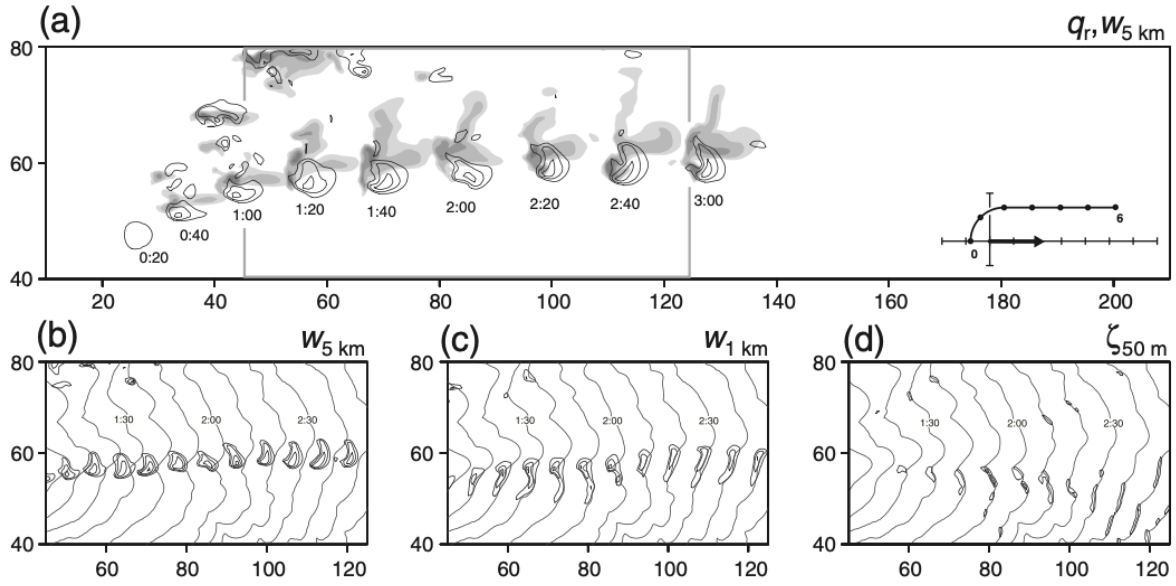

Figure 2.17: Same as Figure 2.14 (a-d) for the easterly ground-relative wind control simulation which does not include terrain. (Reproduced from Markowski and Dotzek 2011; See original paper for detailed description of individual sub-plots.)

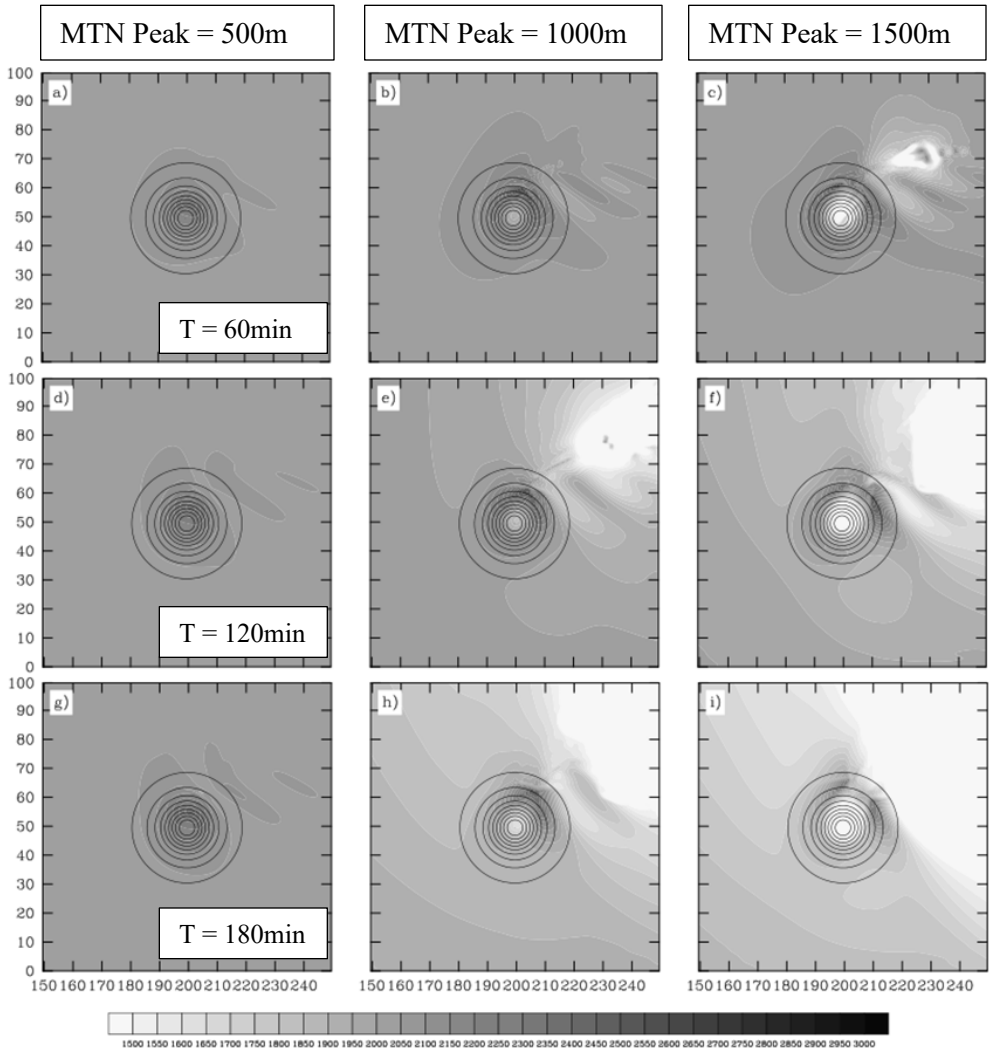

Figure 2.18: Panel plots of terrain induced MLCAPE variation with time for each of the three terrain configurations from Smith et al. (2016). Note the northeastern regions of MLCAPE depletion in panels c, e, f, h, & i are associated with convection triggered by terrain induced gravity waves. Terrain contours were drawn to represent a reduction in height by 10% from the peak to the surface to normalize terrain height for comparison.

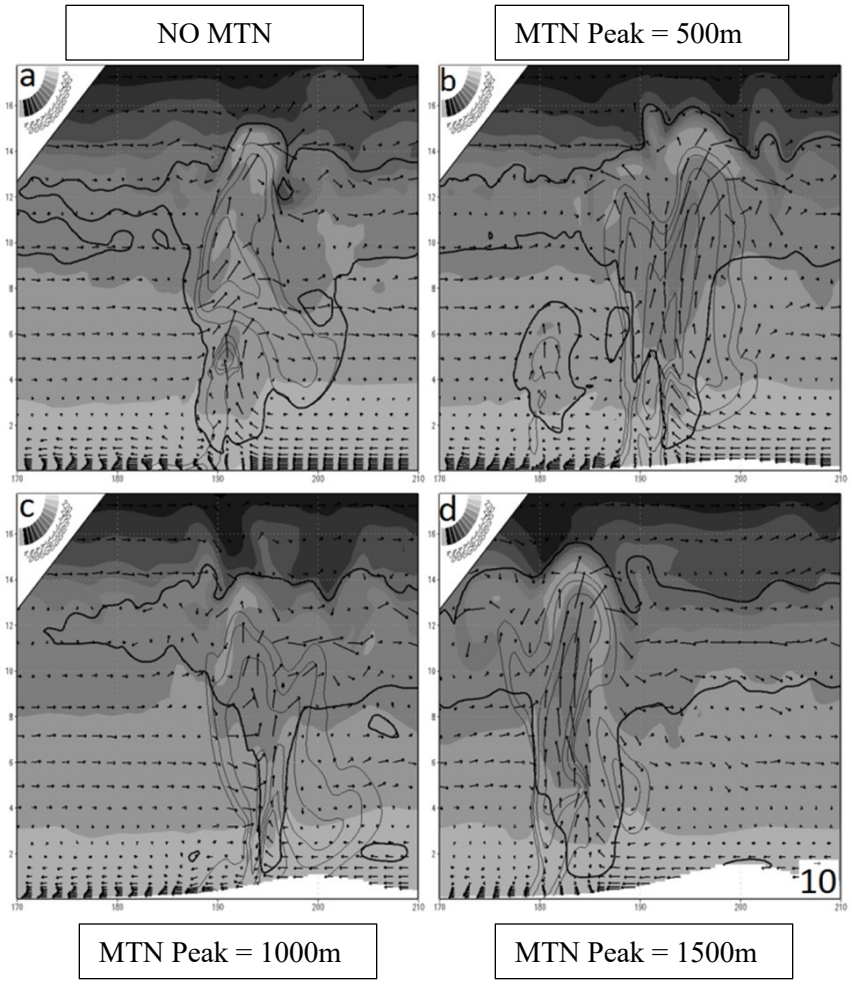

Figure 2.19: Zonal cross-sections of potential temperature (shaded), radar reflectivity (light grey contours), cloud contours (black contours), and wind vectors along the maximum updraft location for each simulation from Smith et al. (2016) at the 180-minute output time.

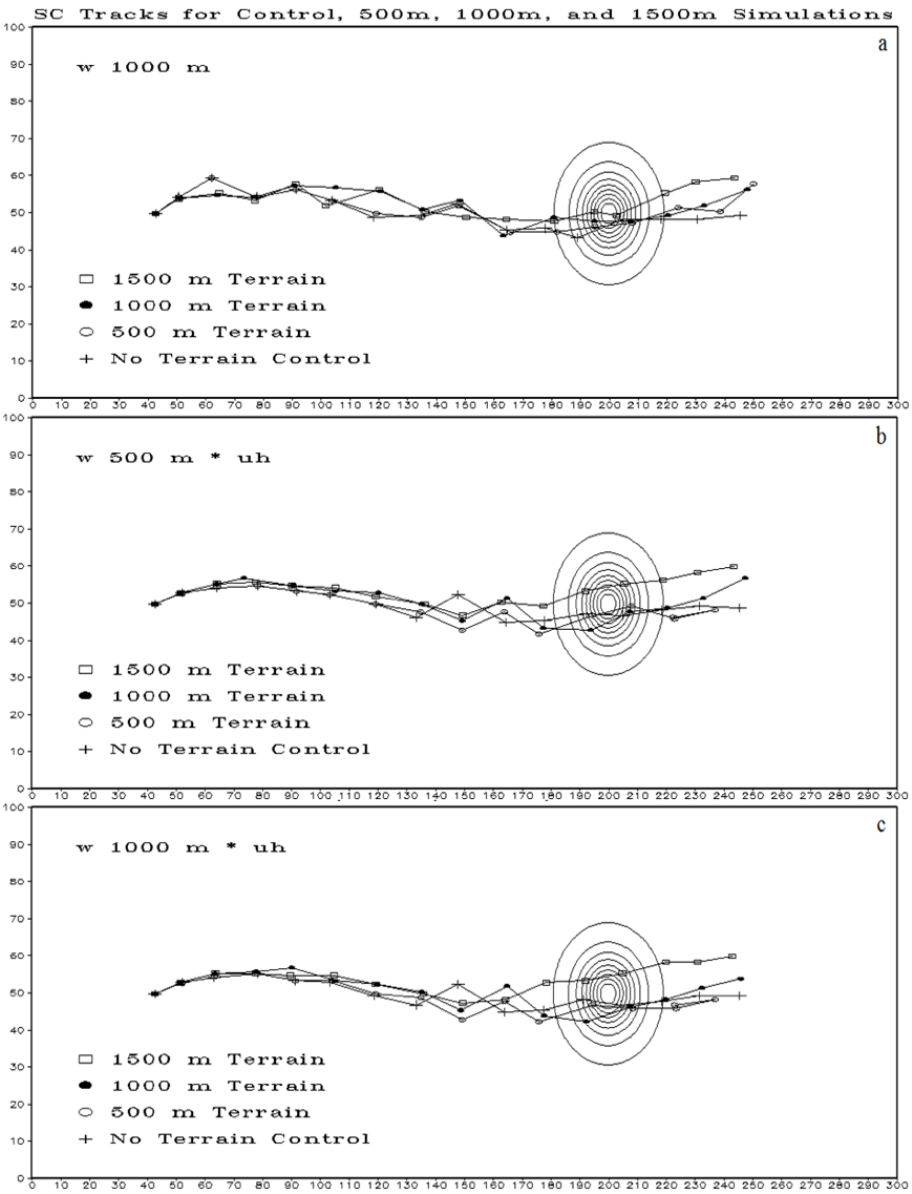

Figure 2.20: Tracks of the three simulated supercells that interacted with terrain (normalized contours) using various tracking metrics: (a) 1 km Updraft, (b) 500 m Updraft multiplied by Updraft Helicity, and (c) 1 km Updraft multiplied by Updraft Helicity (from Smith et al. 2016).

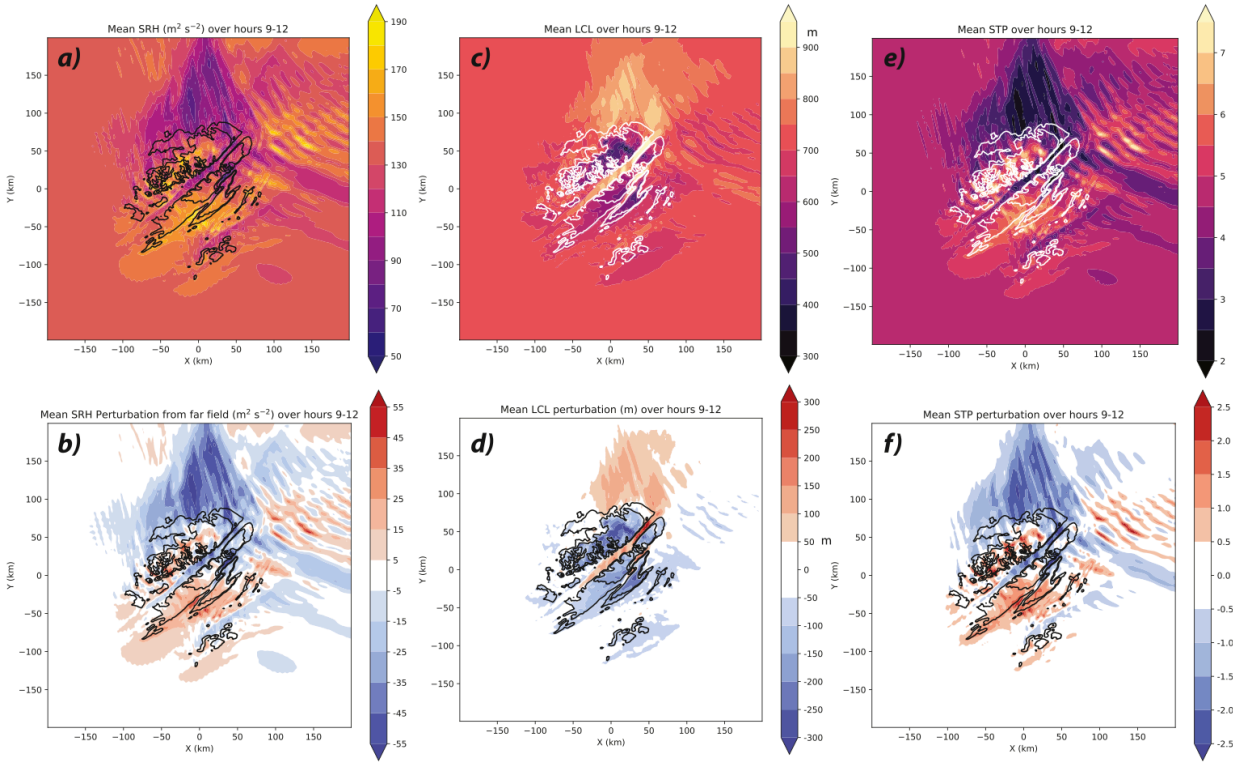

Figure 2.21: The mean and perturbation fields of SRH, LCL, and STP parameters around Sand Mountain (black and white contours) from the southerly flow regime simulations (from Katona and Markowski 2021)

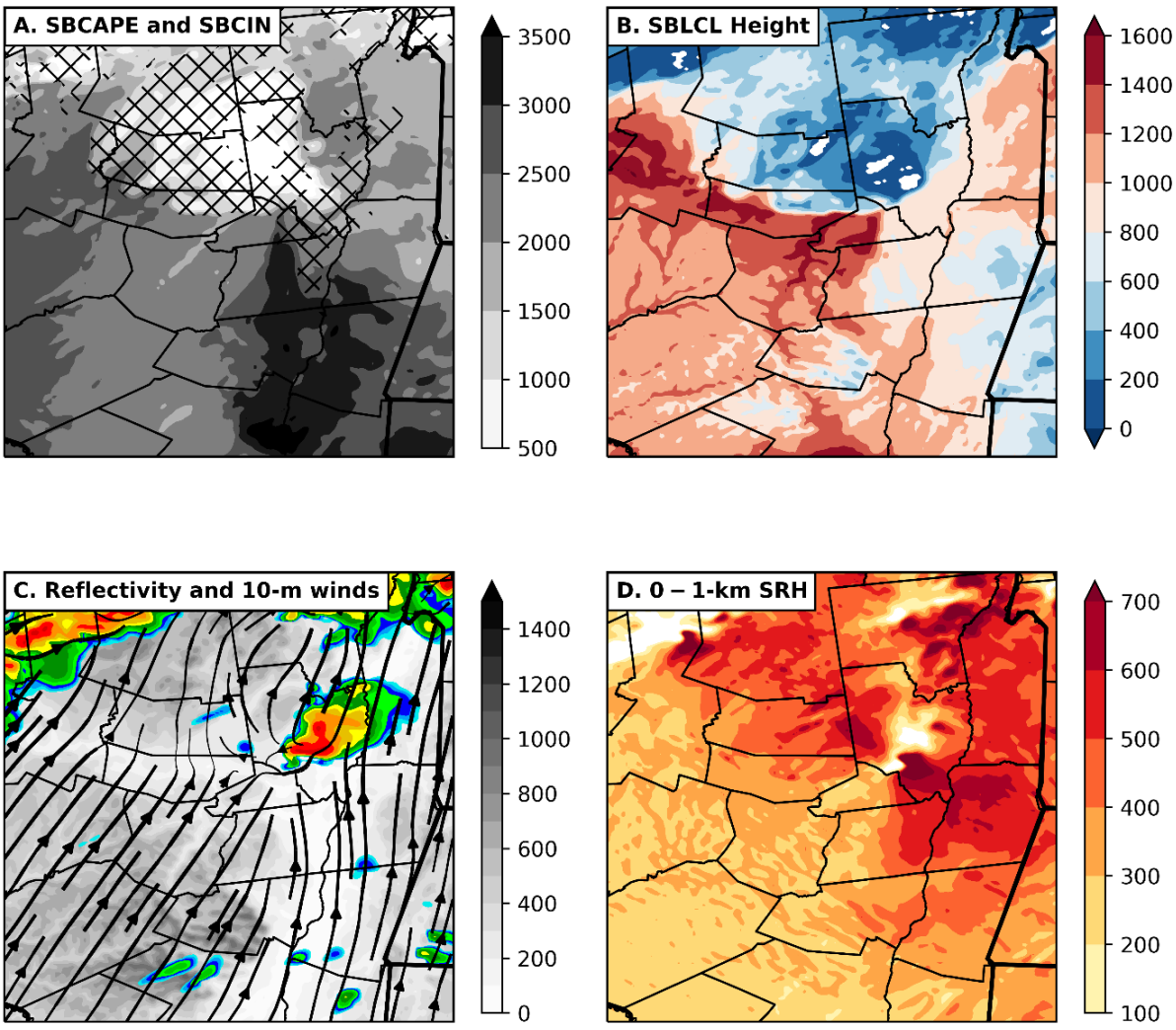

Figure 2.22: An environmental analysis of severe weather parameters around a simulated supercell as it approached the terrain-induced boundary (From LeBel et al. 2021).

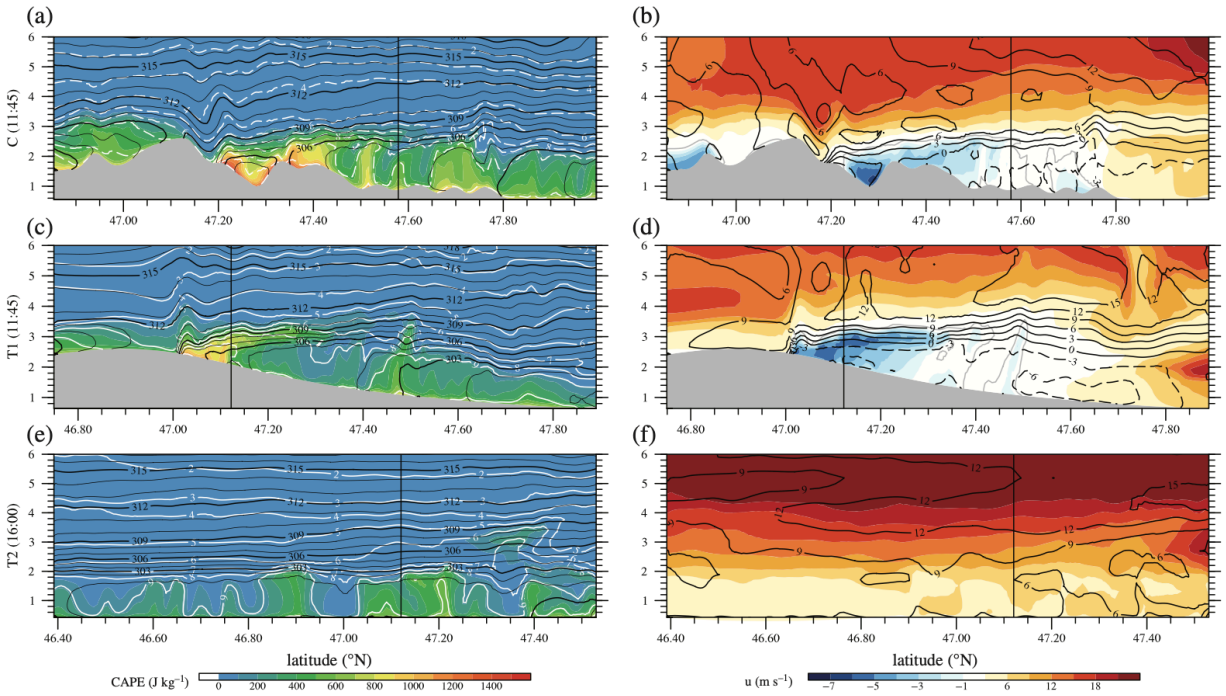

Figure 2.23: Vertical cross-sections of the pre-storm environments, specifically CAPE (left) and zonal wind (right) for the three simulations from Scheffknecht et al. (2017). The control simulation (C) with the most realistic terrain profile is shown in panels (a-b); the idealized terrain simulation (T1) is shown in panels (c-d); and the flat plateau simulation (T2) is shown in panels (e-f).

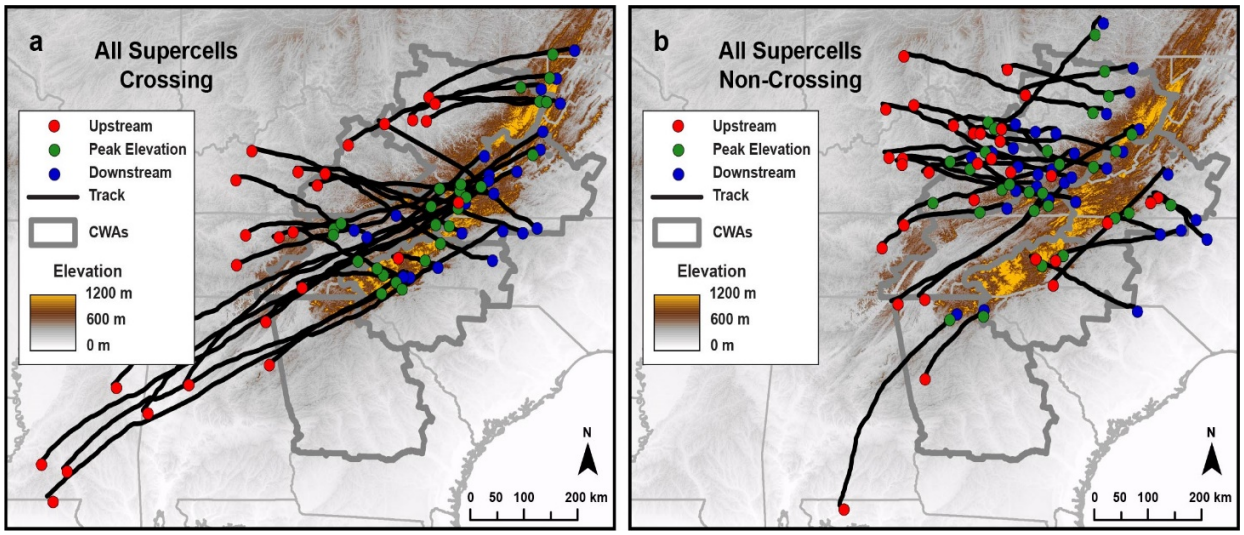

Figure 2.24: Storm tracks of the individual 62 observed supercells utilized in Purpura et al. (2022), McKeown (2021), and the current study overlaid on a DEM to highlight significant terrain in the study area. Tracks are stratified by (a) crossing and (b) non-crossing supercells. The three geographic locations in which RAP/RUC proximity soundings were pulled from are shown for each storm are also shown (Purpura et al. 2022).

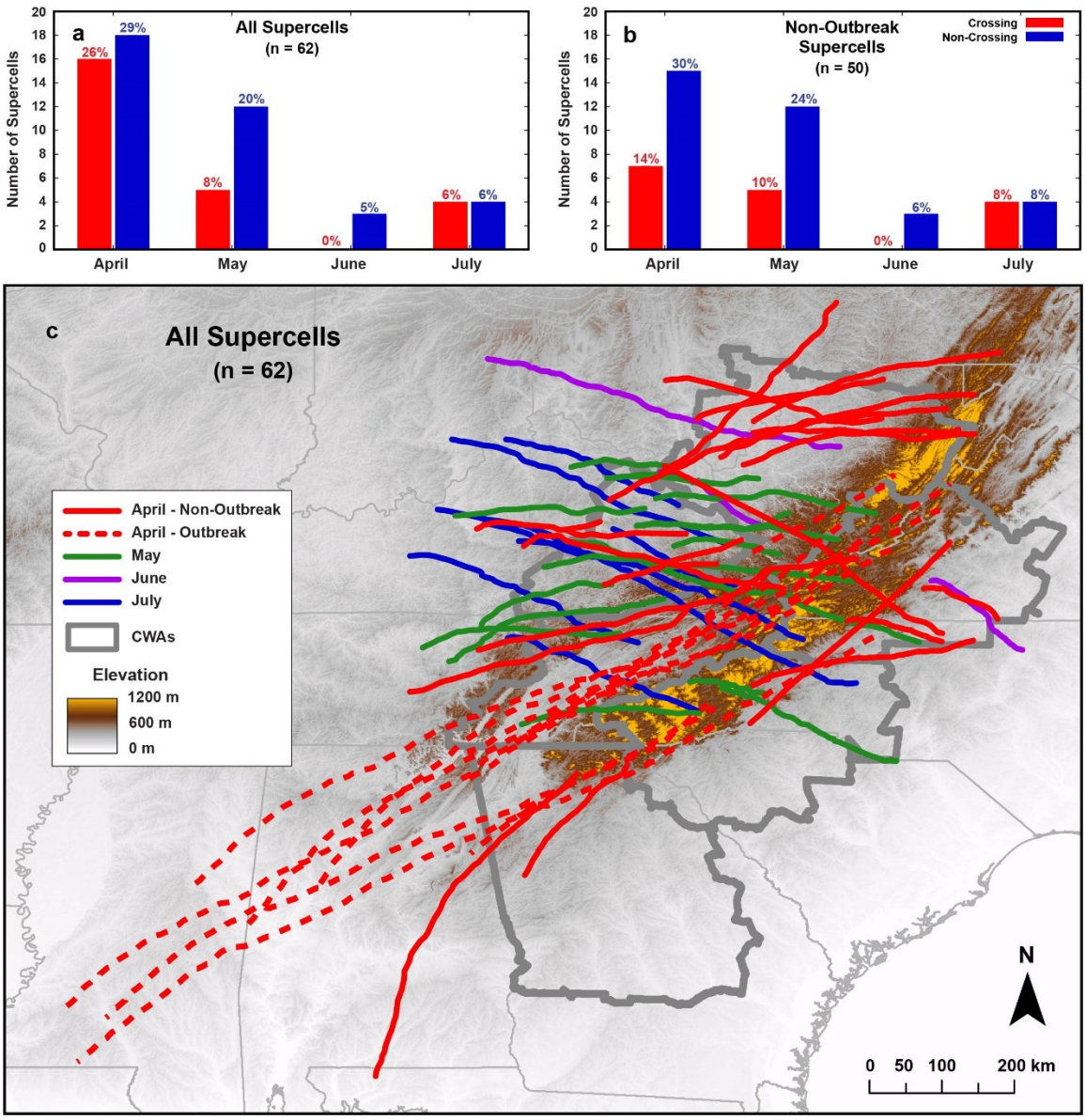

Figure 2.25: A monthly climatology of all 62 supercells tracked during the study. (a) shows the frequency of crossing vs. non-crossing supercells by month for all 62 storms; while (b) shows the same when we remove supercells occurring during the anomalous 27 April 2011 Super Outbreak event. (c) Provides a geographic climatology of storm tracks by month (Purpura et al. 2022).

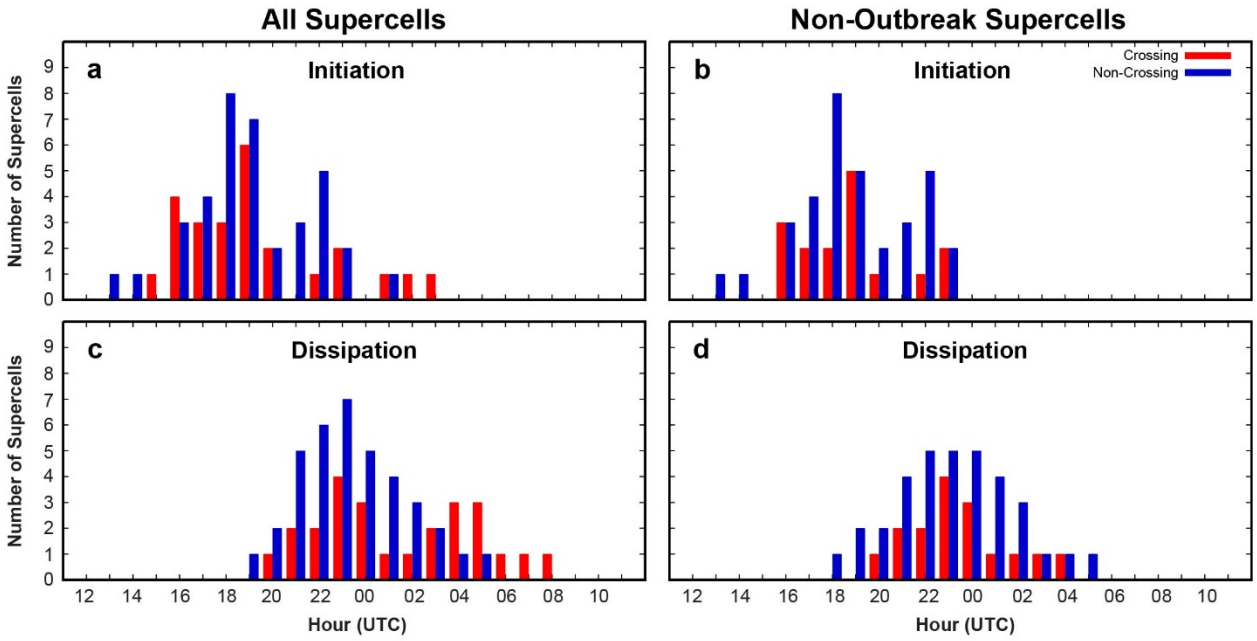

Figure 2.26: A diurnal climatology of the initiation and dissipation times of the 62 observed supercells in the south-central Appalachians after being stratified by the ability to cross significant terrain or not (Purpura et al. 2022).

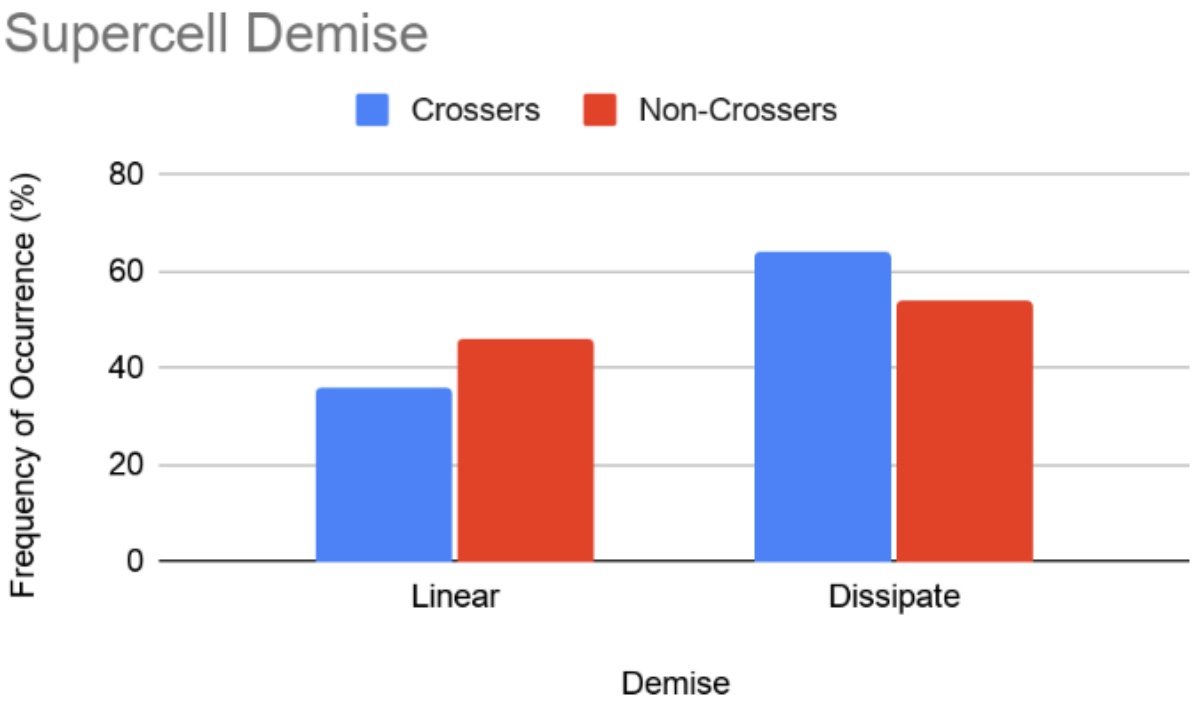

Figure 2.27: Frequency of dissipation modes seen in the 62 observed supercells in the south-central Appalachians after being stratified by the ability to cross significant terrain or not (from McKeown 2021).

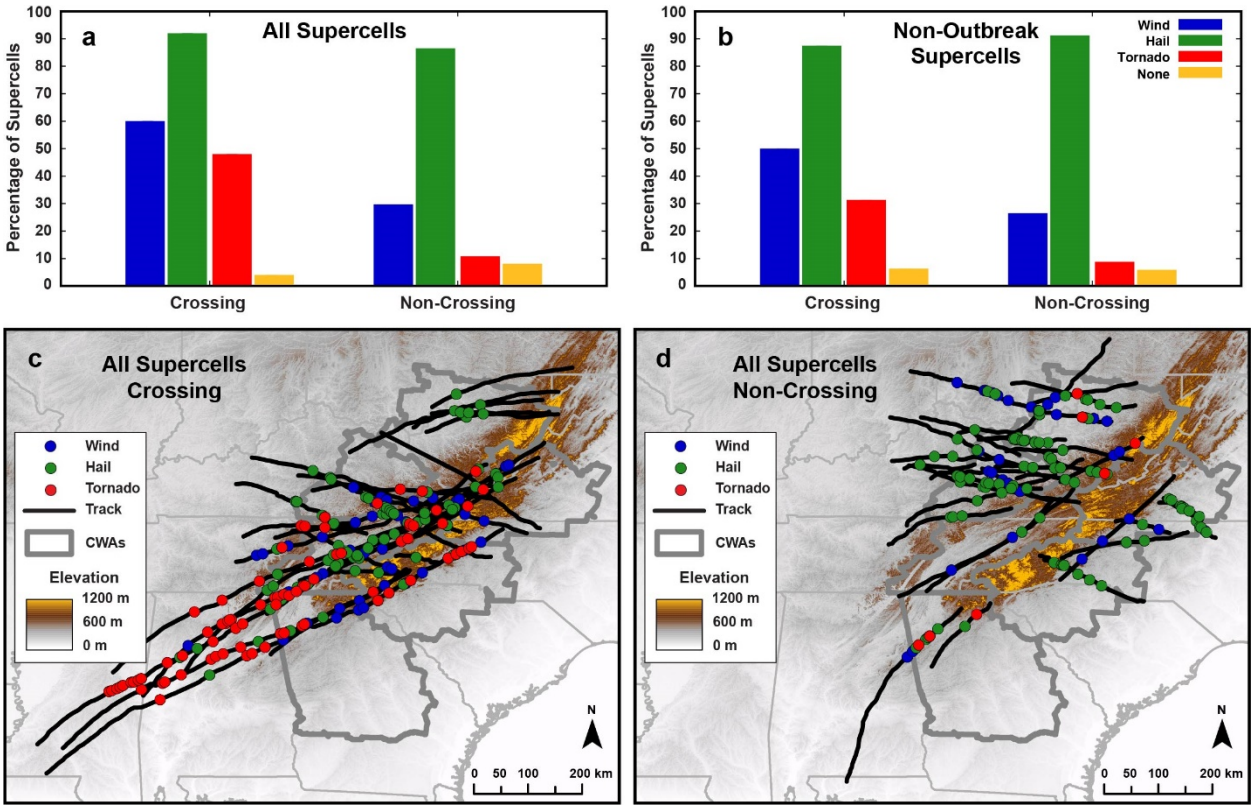

Figure 2.28: (a) Frequency of severe weather reports associated with the 62 observed supercells in the south-central Appalachians; (b) again after being stratified by the 27 April 2011 Super Outbreak; and maps of severe reports for (c) crossing and (d) non-crossing supercells (Purpura et al. 2022).

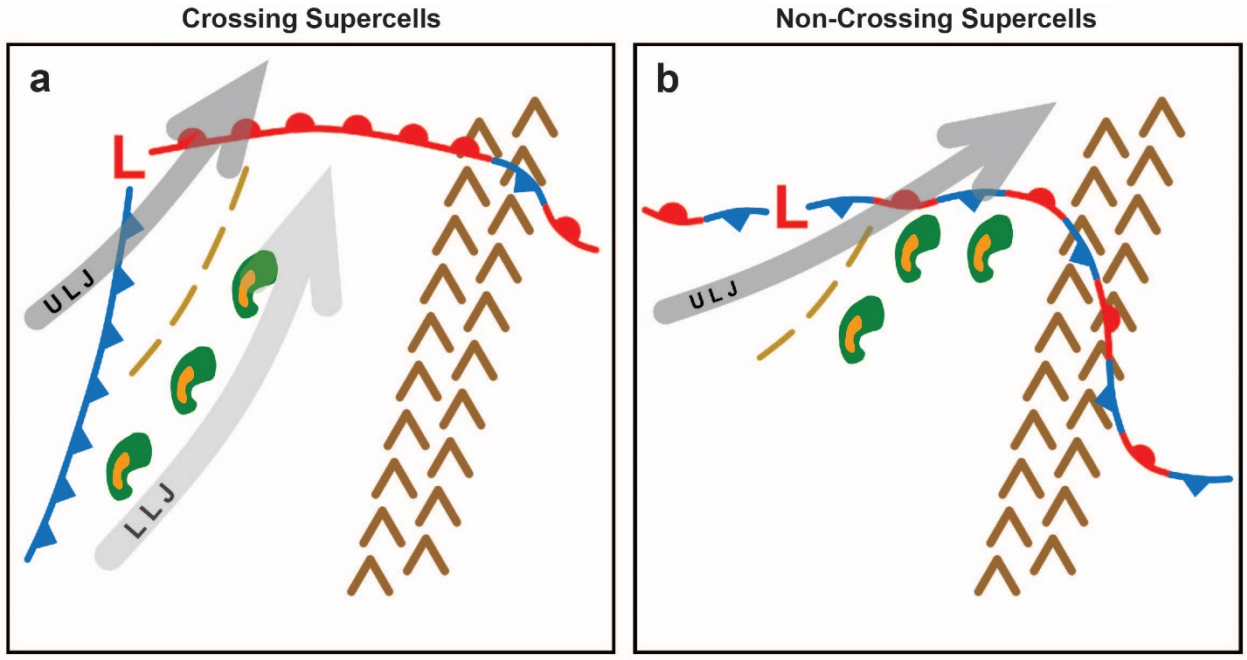

Synoptic Pattern Statistics		
	Crossing (n = 25)	Non-Crossing (n = 37)
Upper-Level (300 mb) Jet		
Right-Entrance	48%	41%
Right-Exit	36%	35%
No Jet Streak	16%	24%
Low-Level (850 mb) Jet		
Yes (> 30 knots)	88%	30%
No (< 30 knots)	12%	70%
Surface Boundary		
Cold Front	52%	8%
Warm / Stationary	20%	65%
Outflow Boundary	28%	27%
Leeward "Wedge"		
Yes	24%	57%
No	76%	43%

Figure 2.29: A conceptual synoptic-scale environment composite that favors (a) crossing and (b) non-crossing supercell events (Purpura et al. 2022).

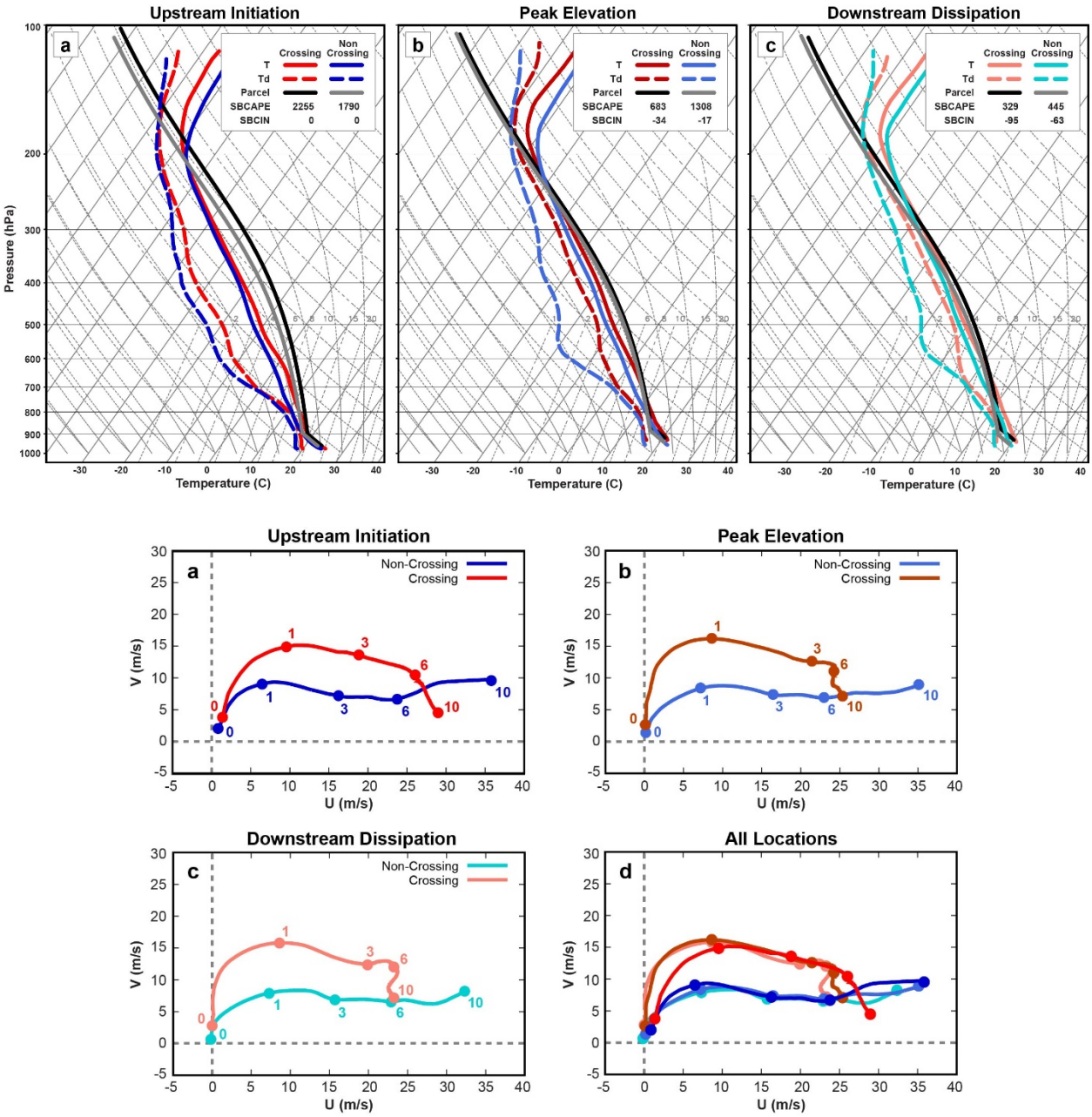

Figure 2.30: RAP/RUC derived composite proximity soundings for both crossing (reds) and non-crossing (blues) for the a) upstream/initiation, b) peak, and c) downstream/dissipation locations relative to the underlying terrain (Purpura et al. 2022).

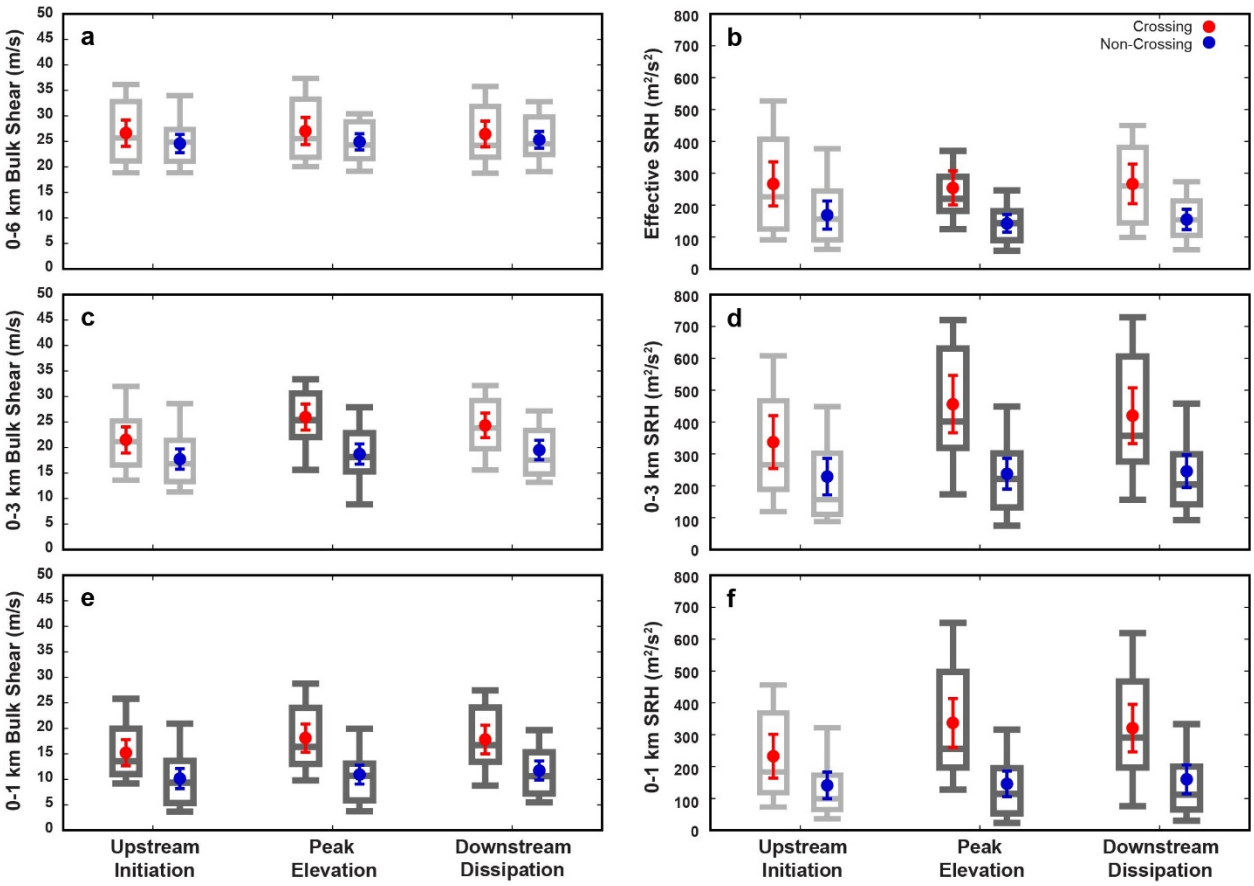

Figure 2.31: Violin plots comparing distributions of (a) 0-1 km and (b) 0-3 km Storm-Relative Helicity for crossers and non-crossers at the upstream/initiation, peak, and downstream/dissipation sounding locations (Purpura et al. 2022).

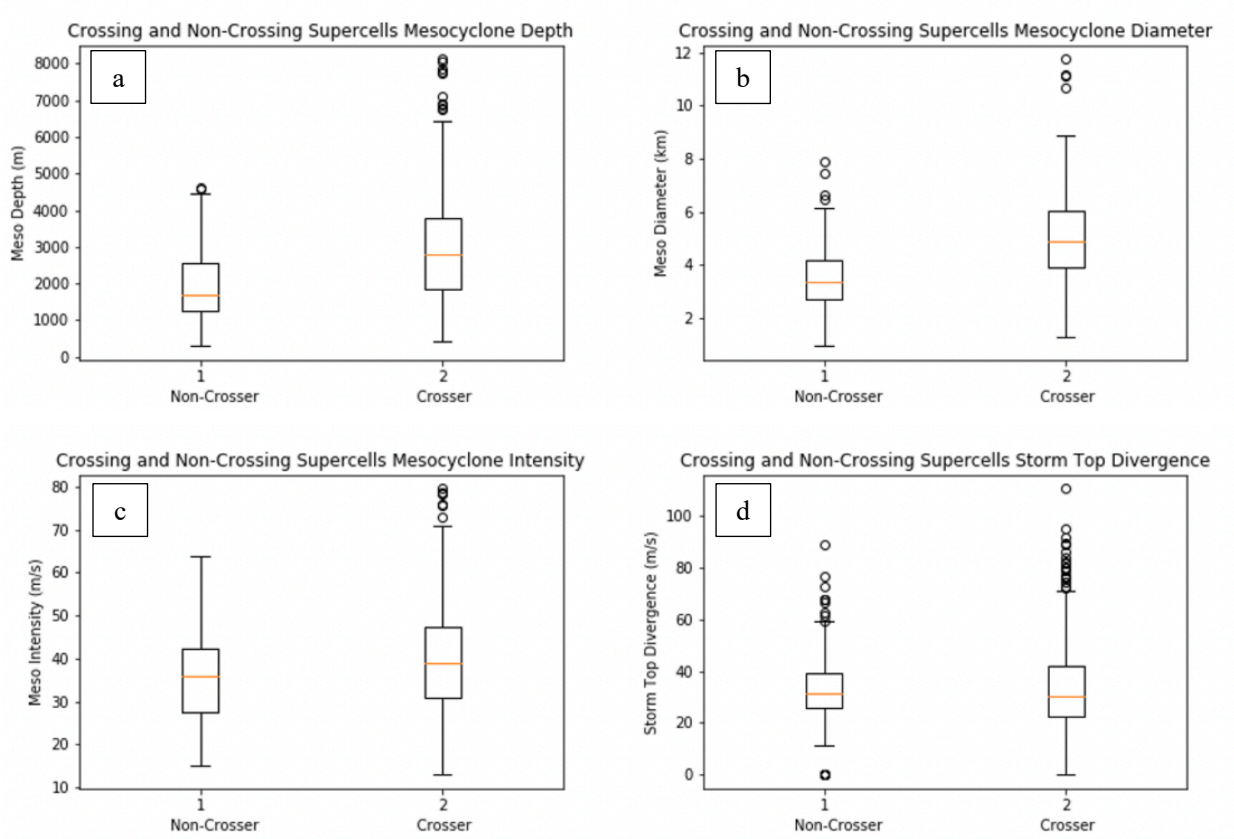

Figure 2.32: Box-and-Whiskers plots of doppler radar-derived (a) Mesocyclone depth, (b) mesocyclone diameter, (c) mesocyclone intensity, and (d) storm-top divergence for both crossers and non-crossers (From McKeown 2021).

CHAPTER 3: DATA AND METHODS

3.1 Introduction

Our primary goal is to investigate discrete simulated supercells in idealized framework, while building-up to more complex topographic configurations which are consistent with the southern and central Appalachians. Such simulations will allow us to deduce the role topography acts to modulate their structure, inflow environment, intensity, and longevity. Idealized numerical modeling permits us to investigate how a simulated storm and its environment will evolve in a controlled manner (i.e., comparing how a storm from a common environment evolves in both the presence of complex terrain and the lack thereof). This chapter is split into four additional sections to discuss our modeling methods and data collection techniques. Section 3.2 provides rationale for the numerical model chosen for this study. Section 3.3 discusses the chosen configurations used to set-up our modeling experiments. Section 3.4 introduces the sensitivity testing methods we used to evaluate terrain-influences on our idealized simulated supercell thunderstorms. Section 3.5 elaborates on our post-processing and data collection techniques to acquire useful information from each simulation.

3.2 Model Selection

All our simulations were performed using Cloud Model 1 version 20.3 (CM1; Bryan and Fritsch 2002), a three-dimensional, non-hydrostatic, non-linear, time-dependent numerical model designed for idealized studies of a wide variety of atmospheric phenomena. The idealized nature of CM1 is key for our study. We can simplify the modeling environment by choosing configurations that restrict the degree of realism but retain the ability to capture the most critical governing physical processes. More specifically, the idealized methods allow us to isolate the cause-and-effect relationships of terrain-induced perturbations to the near-storm environment

without the introduction of additional heterogeneities by other processes observed in the Earth-Atmosphere system (e.g., radiation, friction, Coriolis accelerations).

CM1 has options to include both idealized and realistic terrain, with the latter being derived from a rasterized Digital Elevation Model (DEM). The ability to study simulated storms encountering both idealized and realistic terrain is fundamental. Idealized terrain has already been used in a handful of studies exploring the relationships between severe convective storms and complex terrain (e.g., Frame and Markowski 2006; Letkewicz and Parker 2011; Markowski and Dotzek 2011; Smith et al. 2016). Fewer studies of terrain influences on severe convection have employed realistic terrain (Bryan et al., 2018; Soderholm et al., 2014; Katona and Markowski 2021). The inclusion of the realistic terrain of the southern Appalachians in our idealized simulations will be instrumental in constructing a conceptual model to aid forecasters during supercell events in proximity to the complex terrain of our study area.

3.3 Model Configurations

The following two sub-sections discuss the user-chosen model configurations to set-up our experiments. We first explore configurations that are universal to all the simulations in this study (e.g., domain size, grid-spacing, boundary conditions, microphysics, and convective initiation schemes) in Section 3.3.1. We then discuss configurations that must vary across simulations for us to explore the differences between crossing and non-crossing storm environments and the respective simulated supercell each produces. This requires individual simulations of each environment that include, no terrain as a control simulation, idealized terrain, and realistic terrain. Details of these configurations are discussed in Section 3.3.2.

3.3.1 Universal Configurations

All user-defined model configurations are provided in Table 3.1. The model domain was chosen to be 600 x 400 km with uniform horizontal grid-spacing of 250 m. The vertical extent of the domain reaches 20 km, with a stretched vertical grid in the lowest 6 km, starting at 100 m spacing near the model surface to 500 m aloft. This allows us to effectively resolve the lower-level features of interest while reducing computational costs. Rayleigh damping was applied above 14 km to limit the reflection of any gravity waves from the top of the domain back towards the surface. Free-slip boundary conditions are applied at the bottom of the domain, and all the lateral boundaries are open-radiative. Sub-grid turbulence was parameterized based on the turbulent kinetic energy scheme of Deardorff (1980). Accordingly, no surface physics were included. A constant large timestep of 1.0 s was chosen to maintain model stability.

Each simulation is integrated for a minimum of six hours (some simulations up to 8 hours), with output files being written after every five minutes of integration time to combat storage limitations. The realistic terrain simulations require an additional two hours of integration time to allow the model to adjust to the realistic terrain field before we can initialize convection, which occurs following the 2-hour initialization period. Precipitation microphysics were governed by the National Severe Storms Laboratory double-moment scheme, including both hail and graupel with an experimentally determined initial cloud condensation nuclei (CCN) concentration of 1.0×10^9 m^{-3} (Mansell and Ziegler 2013). Convective initiation (CI) occurs via an updraft nudging technique (Naylor and Gilmore 2012) to mimic forcing via a frontal lifting, a common initiation method for supercells interacting with the Appalachians (Purpura et al. 2022). Nudging is applied over a 15 x 100 x 0.75 km^3 region located towards the southwest corner of the model domain and acts to force a 10 ms^{-1} updraft for the first 15 minutes of integration before

being turned off. Again, during the realistic terrain simulations this convective initiation scheme occurs after a two-hour stabilization period. The chosen nudging height and magnitude were experimentally confirmed to be optimal for maximizing simulated supercell intensity and longevity when compared to other CI techniques (as shown in Naylor and Gilmore 2012).

All our simulations are conducted by implementing a temporally-fixed base-state conditions. In each respective simulation, the crossing or non-crossing composite upstream (relative to the terrain) environmental soundings from Purpura et al. (2022) are used as the base-state (Fig. 2.30a); any temporal and horizontal variations that arose in the model were a result of terrain interactions or perturbations from convective development. The expectations are that the crossing environmental composite sounding (shown in Fig. 3.1a) will produce a simulated supercell capable of crossing the modeled terrain feature, while the non-crossing environmental composite sounding (shown in Fig. 3.1d) will produce a simulated supercell that fails to fully traverse the modeled terrain. This hypothesis forms the basis for our simulations; where we provide the composite initial conditions in which our observed storms experienced to the model and allow it to freely evolve in a horizontally homogenous manner during integration.

Figure 3.1a-f displays the RAP/RUC composites for all three locations (upstream, peak, downstream) for both crossing and non-crossing storms after being interpolated to the CM1 model grid to provide a conceptual idea of what the background field evolution should be like during our simulations if the model evolves in a consistent manner with the observations (Purpura et al. 2022). Note that interpolating both the raw RAP/RUC upstream crossing and non-crossing composite data to CM1 resulted in super-adiabatic layers near the surface that had to be manually removed to prevent model instabilities from arising. Neither the crossing nor non-crossing peak and downstream composites required any modifications.

3.3.2 Terrain Configurations

The following section elaborates on our methods to generate both the idealized and realistic terrain fields used in our simulations. The domain remains completely flat in both the zonal and meridional directions for all control simulations. To construct the idealized terrain profile *h(x)* that is representative of the Appalachian Mountains, we employ the "Witch of Agnesi" equation shown below:

$$h(x) = \frac{h_0}{1 + (\frac{x - x_0}{a})^2}$$

The central location, x_0 was chosen to be 350 km so that our simulated supercells would have enough time to reach maturity before encountering any significant terrain slopes. The peak elevation, h_0, is set to 0.75 km and is based on the mean peak elevation of all 62 observed supercells from Purpura et al. (2022) & McKeown (2021). The half-width, *a* is set at 50 km to be representative of the entire Appalachian Mountain chain (e.g., as in Letkewicz and Parker 2011). The resulting terrain profile from this configuration varies only in the zonal direction and is shown as a cross-section in Fig. 3.2.

Generating the realistic terrain field for our simulations began with collecting the terrain heights of the Southern Appalachian's from the U.S. Geological Survey (USGS) digital elevation model for latitude/longitude between 87-78º W / 34-40º N and re-gridding it to the CM1 model grid via a bilinear interpolation technique (Fig. 3.3a). The interpolated terrain field is then passed through a 6-Δx Gaussian filter to limit potential shortwave forcing and lowered by 300 m to bring the mountain base close to sea-level (Fig. 3.3b). An ellipse is then drawn over the terrain features which corresponded with the peak observed storm track density over the study area. A linear decay towards 0 m is performed outward from the ellipse to isolate the features of interest

to remove any lateral boundary interactions with the variable terrain field (Fig. 3.3c). Lastly, the resultant terrain field is clipped to the CM1 domain (Fig 3.3d) and converted into a binary file which is then read by CM1 when integrating a realistic terrain simulation. These methods closely follow the framework provided by both Soderholm et al. (2014) and Katona and Markowski (2021), who generated realistic terrain in an idealized fashion for modeling studies focusing on different geographic locations.

3.4 Sensitivity Experiments

This section will explicitly state the storm-scale sensitivities we will be investigating and define the associated acronyms used to describe each simulation during the analysis. For each set of experiments, we will compare the crossing supercell composite environment with the non-crossing supercell composite environment. To identify the range of outcomes of supercells interacting with the Appalachians and develop a conceptual model, sensitivity tests will be used to vary the terrain configuration. We begin by investigating the upstream composite environment's ability to produce a discrete quasi-steady supercell without terrain as a control simulation (CTL). These simulations serve as a baseline of simulated supercell behavior in our model. Next, we include the idealized terrain profile (TRN) as our lower boundary to determine bulk effects of the Appalachians on supercells; note that this set of experiments include terrain-induced variations in the background environment due to airflow over the terrain.

The prior literature also emphasized the importance of cross-barrier flow in realizing terrain-induced environmental perturbations (e.g., MD2011; Smith et al. 2016; Tang et al. 2016; Lyza and Knupp 2018; LeBel et al. 2021; Katona and Markowski 2021). Where the idealized terrain profile (Fig 3.3) is oriented along the meridional axis, we've chosen to rotate the wind profiles by 25º (MOD) to reorient low-level flow with respect to the terrain in a manner

consistent with the observations. Recall that the Appalachian Mountains range is oriented roughly 25º east of north so the chosen modifications help increase the realism of our idealized MOD simulations. We hypothesize that the rotated wind profiles will better capture the terrain-induced environmental perturbations associated with cross-barrier flow. A comparison between all six composite hodographs before and after the rotation is shown in Fig. 3.4. Lastly, we utilize the realistic terrain field (RLTRN) as the lower boundary to investigate finer-scale impacts of terrain on supercell morphology.

Since the realistic terrain field is significantly more complex than the idealized terrain, we also decided to run additional simulations after sub-setting the composite environments by events occurring on 27 April 2011 Super Outbreak. Outbreak storm statistics were statistical outliers in the previous analyses (Purpura et al. 2022; McKeown 2021), which inspired us to investigate how dependent the modeling results will be on the outbreak. Also, most non-outbreak crossers maintained a NW-SE storm motion, while the outbreak crossers were primarily SW-NE (See Fig. 2.25). The additional composite stratification allows us to explore the influence of storm motion on simulated supercell evolution in the southern Appalachians (Figs. 3.5-6 a-f). It is important to note that we had to extend the model domain by 100 km to the south in all realistic terrain simulations to provide adequate space for a storm to track towards the realistic terrain field without modifying any wind profiles.

In summary, we will have a total of 6 simulation for both crossing and non-crossing composites (e.g., Control, Idealized Terrain, Modified Hodograph, Realistic Terrain, Realistic Terrain Outbreak Only, and Realistic Terrain Outbreak Removed) resulting in 12 total simulations for this study. This range of experiments allow us to compare simulated crossing and non-crossing supercells at varying degrees of realism to help consolidate supercell behavior

in the south-central Appalachians into a conceptual model. Table 3.2 provides a short summary of each experiment as an additional reference.

3.5 Model Output Post-Processing and Data Collection

Once each simulation has been fully integrated, the resulting output files are processed using a combination of Xarray (Hoyer and Hammam 2017), Matplotlib (Hunter 2007) and MetPy (May et al. 2020) packages using Python 3.10 (Van Rossum and Drake 2009). An algorithm (Fig. 3.7) is implemented to track the simulated supercell based on the maximum integrated 2-5 km Updraft Helicity (UH), given by:

$$\int_{z=2\ km}^{5\ km} w\zeta\ dz$$

where w is the vertical component of the wind, and ζ is the vertical component of vorticity (Kain et al. 2008). UH is used in this study as a proxy of the mid-level mesocyclone intensity and is readily available in CM1 output. The algorithm activates 100 minutes after convective initiation (120 min for Realistic Terrain) to provide ample time for convective development and organization into supercellular structures.

For each output timestep (5 minutes of simulation time), the grid cell containing maximum UH (UH_{max}) is identified and a grid-cell weighted areal average (5 km in diameter, centered on the maximum UH grid point, UH_{avg}) is computed to determine if UH_{max} is an anomaly or a product of a mature mesocyclone. Following experimentation, we choose to employ an UH_{avg} threshold of 150 m^2s^{-2} to distinguish when a rotating updraft can be considered supercellular, as it was found to be robust, resulting in more consistent tracking of isolated storms. To further ensure we are tracking the same convective cell over time, the algorithm

performs an additional check to verify the UH_{avg} is within 15 km of the location identified 5 min prior (Fig. 3.8).

Once a simulated storm is confirmed as supercellular, a near-storm proximity inflow sounding is defined by the grid column located 30 km to the south-southeast of UH_{max} (i.e., sampling the near-inflow environment; Parker 2014). From this inflow sounding we collect the surface elevation and data about updraft characteristics, vertical shear profile and buoyancy at different height levels. This data is used to construct a time-series of relevant mesocyclone and environmental parameters, which allows us to compare differences between crossing and non-crossing storm environments and the role terrain plays in modulating these environments.

To quantify mesocyclone characteristics, we assume that the 2-5 km UH maxima for a given time-step corresponds to the center of the storm updraft. This may not be the best assumption physically but with controls in place via our tracking algorithm it does provide consistency in our data collection. The mesocyclone will be analyzed via three key metrics: Mesocyclone Intensity via UH_{avg}; Mesocyclone Depth via the difference between the lowest and highest grid points above the local UH_{max} that exceed a vertical vorticity threshold of 0.1 s^{-1}; and Mesocyclone Diameter via the area within a 35 x 35 km^2 that exceeds a $w\zeta$ threshold of 0.1 ms^{-2} box also centered on the local UH maxima. We follow a similar methodology to quantify the near-storm surface cold pool intensity (minimum potential temperature perturbation) and size (area of grid points with potential temperature perturbations < -1 K) with in the 35 x 35 km^2 UH-centric box. Note the main limitation in our methods is the temporal resolution of our dataset; we cannot distinguish any modulations that occur on a temporal scale smaller than 5 minutes due to the output storage limitations.

Namelist Parameter Description	***Chosen Value(s)***
Number of grid points in x, y, & z directions	*Idealized Terrain (2400, 1600, 48)* *Realistic Terrain (2400, 2000, 48)*
Horizontal grid spacing in the x, y, & z directions (Note: dz is an approximate average due to stretching)	*250, 250, 100 m*
Large Time Step	*1.0 s*
Maximum integration time	*21600.0 s*
Frequency of 3D model output	*300.0 s*
CM1 Set-up to determine how turbulence is handled	*1 (Large Eddy Simulation)*
Adaptive time step flag	*0 (off)*
Sub grid-scale turbulence model for Large Eddy Simulation	*1 (TKE Scheme)*
Option for Rayleigh Damping Zone at the top of domain	*1 (On)*
Microphysics Scheme	*27 (NSSL 2-Moment Scheme)*
Include Coriolis Accelerations?	*0 (off)*
Equation set for moist microphysics	*2 (Energy & Mass conserving equation set which accounts for heat capacity of hydrometers)*
West, East, North, and South Lateral Boundary Conditions	2 (Open-Radiative)
Bottom & Top Boundary Conditions for wind	1 (Free-Slip)
Convective Initialization Option	12 (Updraft Nudging)
Base of the Rayleigh Damping Zone	14000 m
Include Atmospheric Radiation?	0 (no)
Vertical grid spacing & vertical grid stretching parameters	1 (Wilhelmson & Chen), 20000, 0 6000, 100, 500 m
Shape parameters of graupel and hail for NSSL 2-Moment Scheme	0, 2.0
Base CCN concentration for NSSL 2-Moment Scheme	1.0e9 (Med-High Continental)

Table 3.1: A list of all relevant CM1 namelist parameters relevant to the universal configuration of our simulations. Any parameters not listed in this table remain at their default settings.

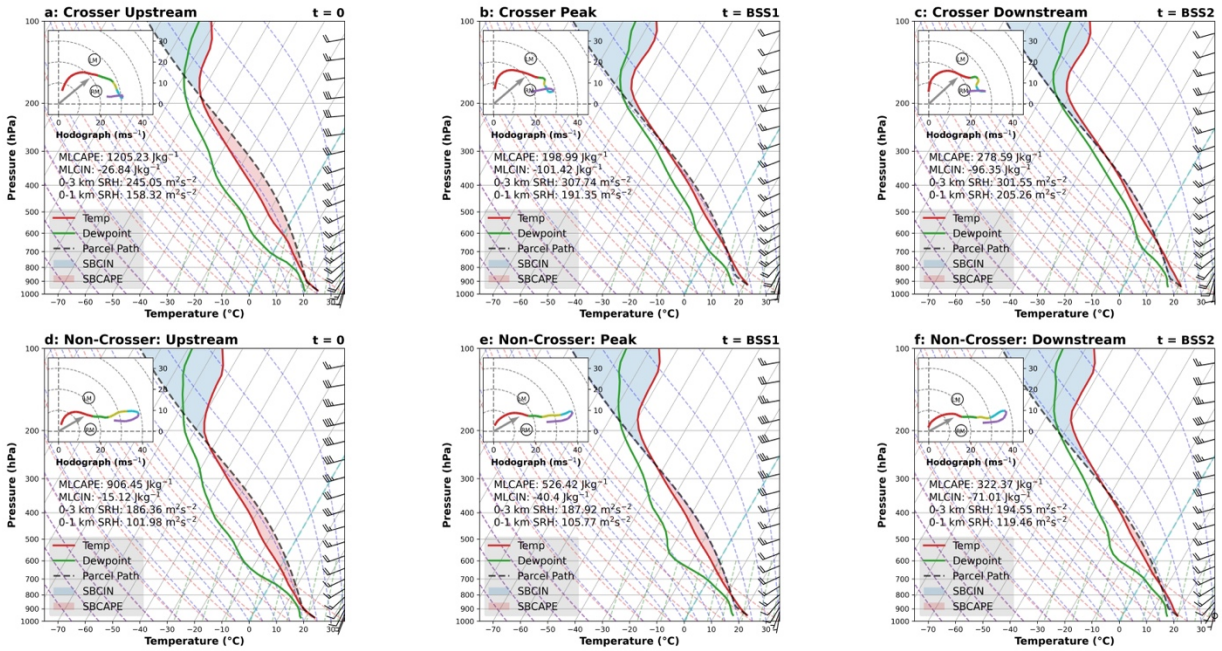

Figure 3.1: Composite environmental inflow soundings of all observed (a-c) Crossing Supercells and (d-f) Non-Crossing Supercells after being interpolated to the CM1 model grid. The upstream soundings (a, d) are used for the initial conditions for all simulations. The peak and downstream soundings (b, c, e, f) are only utilized during simulations utilizing Base-State Substitution (BSS) when we force the model background field to remain consistent with the observed environments.

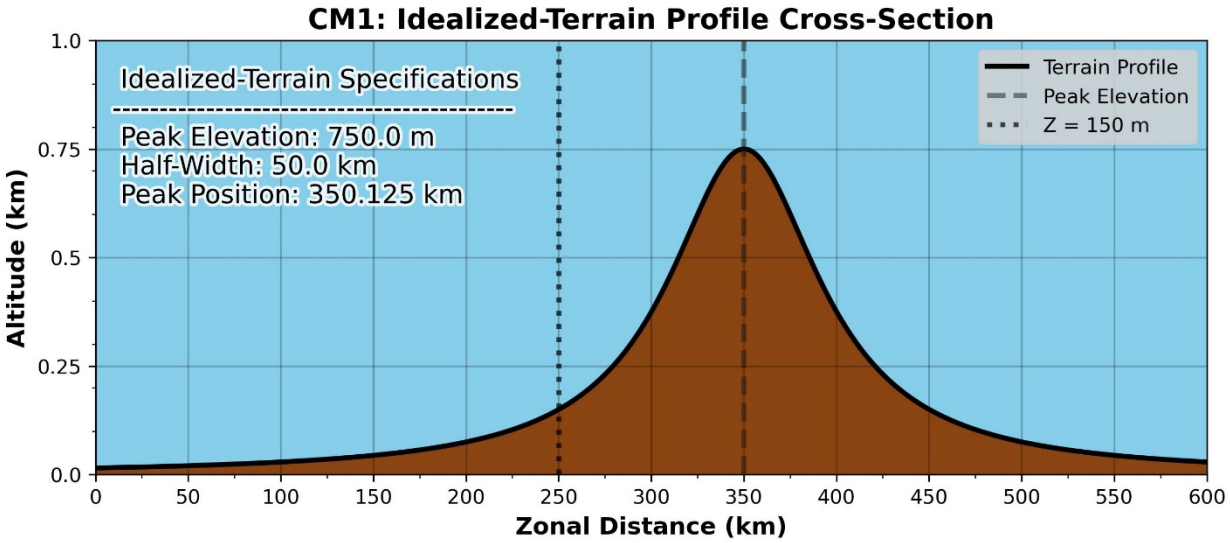

Figure 3.2: A cross-section along the zonal distance of the model domain to show how we implemented an idealized bell-shaped curve to be representative of the Appalachian Mountains in our idealized-terrain simulations. This profile remains constant along the meridional distance of the model domain.

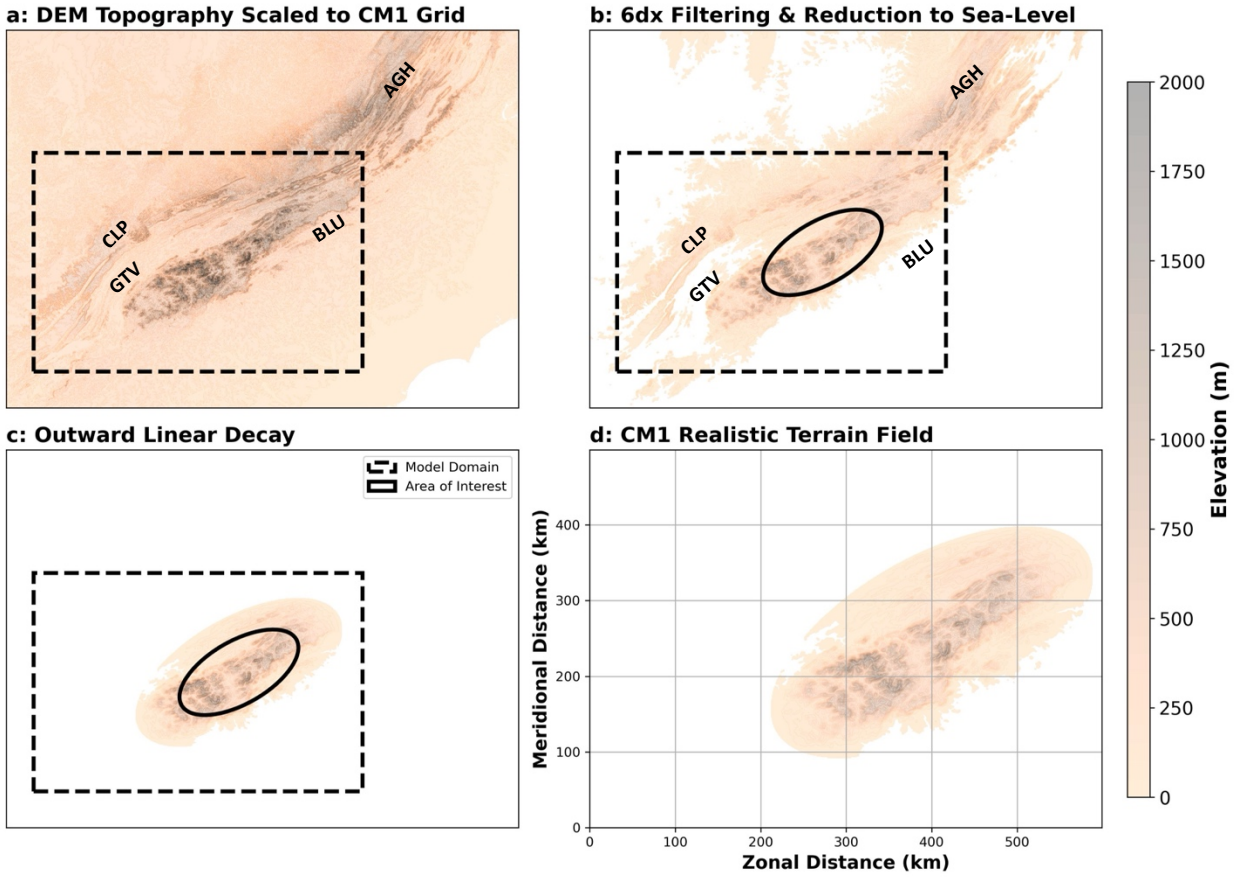

Figure 3.3: A visual representation of the transformation of the real Southern Appalachians terrain profile from a 30 m USGS DEM into an isolated series of ridges representative of the geographic area with the highest track densities of our observed storms. Key terrain features are annotated with an acronym to provide some geographic reference (Cumberland Plateau CLP; Blue-Ridge BLU; Great Tennessee Valley GTV; Allegheny Mountains AGH). (a) First the DEM data is scaled to the CM1 model grid via a bilinear interpolation from 30 m to our chosen model grid spacing of 250 m. (b) a 6-dx gaussian filter is applied to the terrain field to eliminate potential shortwave forcing; and is then lowered by 300 m to bring the base of the ridges approximately to sea-level. (c) then the terrain field within the drawn ellipse is preserved while the rest is linearly decayed towards zero within three times the radius of the ellipse. (d) displays the final realistic terrain field after being scaled down to the CM1 model domain.

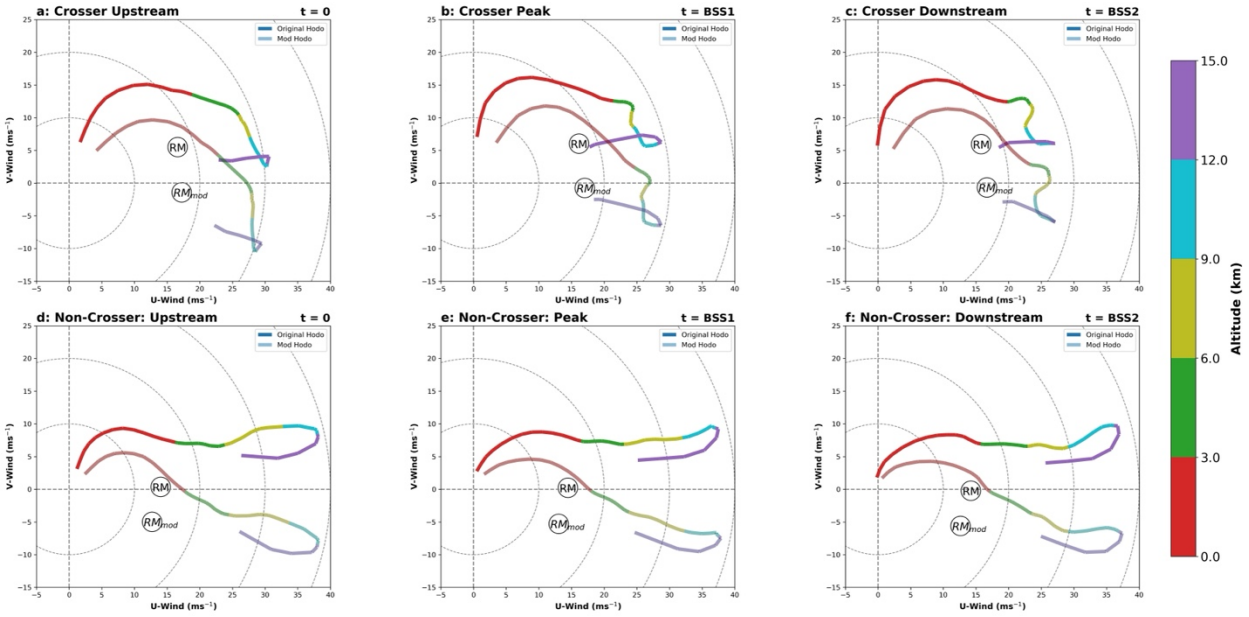

Figure 3.4: Same as Figure 3.1 but with emphasis on the composite hodographs after being interpolated to the CM1 model grid. The Bunker's Right Mover estimated storm-motions are annotated as well for both the (RM) original and (RM_{mod}) modified hodographs; rotated by 35° to increase the magnitude of cross-barrier flow in our idealized terrain simulations. Again, the upstream hodograph (a, d) are used for the initial conditions for all simulations (Steady-State & Variable-State). The peak and downstream hodograph (b, c, e, f) are only utilized during simulations utilizing BSS.

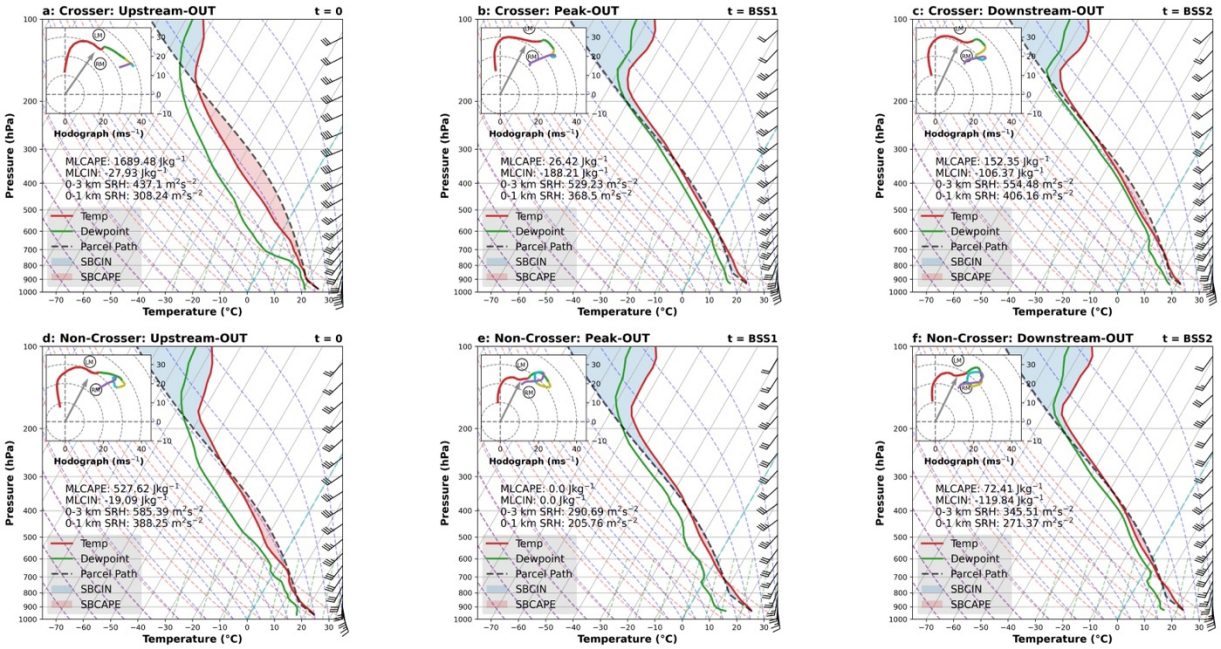

Figure 3.5: Same as in Figure 3.1 but for composite soundings of only the observed storms occurring during the 27 April 2011 Super Outbreak.

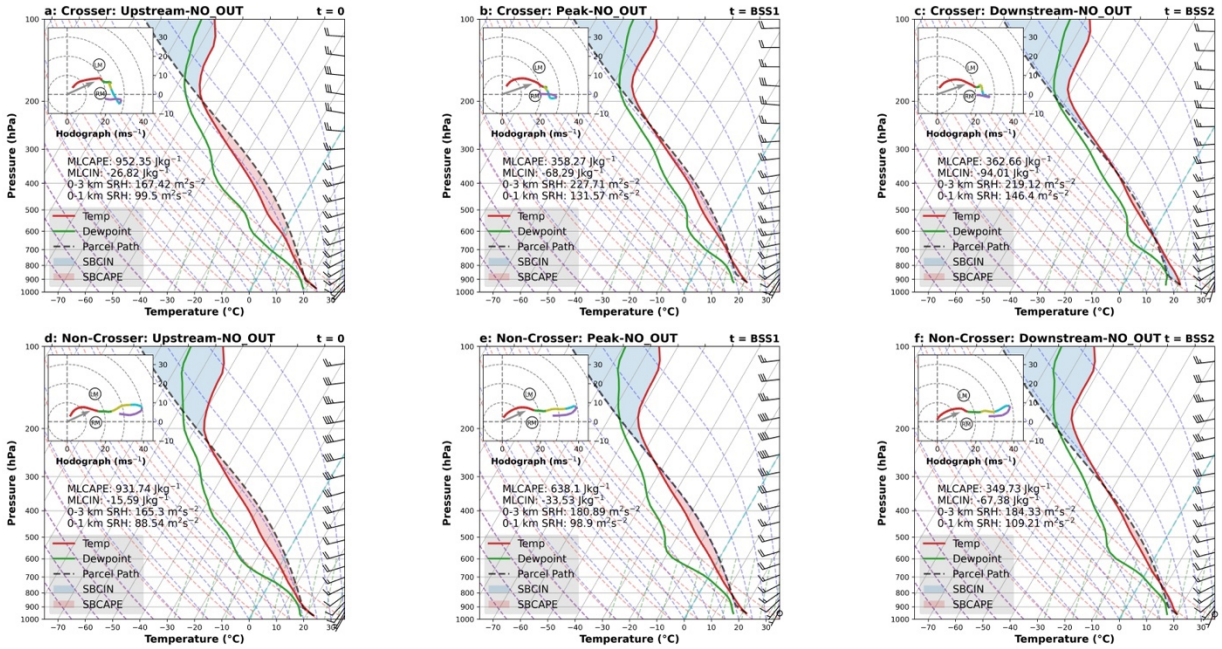

Figure 3.6: Same as in Figure 3.1 but for composite soundings of all the storms in our dataset that did not occur during the 27 April 2011 Super Outbreak.

Experiment	**Description**
CTL	*Initial Conditions: Upstream Composite* *Terrain: Flat/No Terrain*
TRN	*Initial Conditions: Upstream Composite* *Terrain: Idealized Bell-Shaped Curve*
MOD_HODO	*Initial Conditions: Upstream Composite (Wind profile rotated 25°)* *Terrain: Idealized Bell-Shaped Curve*
RLTRN_ALL	*Initial Conditions: Upstream Composite* *Terrain: Isolated Realistic Terrain Field*
RLTRN_OUT	*Initial Conditions: Upstream Composite (Outbreak Storms Only)* *Terrain: Isolated Realistic Terrain Field*
RLTRN_NO_OUT	*Initial Conditions: Upstream Composite (Non-Outbreak Storms Only)* *Terrain: Isolated Realistic Terrain Field*

Table 3.2: A table summarizing the twelve key experiments ran to investigate simulated supercell sensitivity to terrain. The simulation short names are listed in the Experiment column. Key features of each experiment are listed in the Description column. Each experiment was ran twice, once using the crossing composites and again with the non-crossing composites.

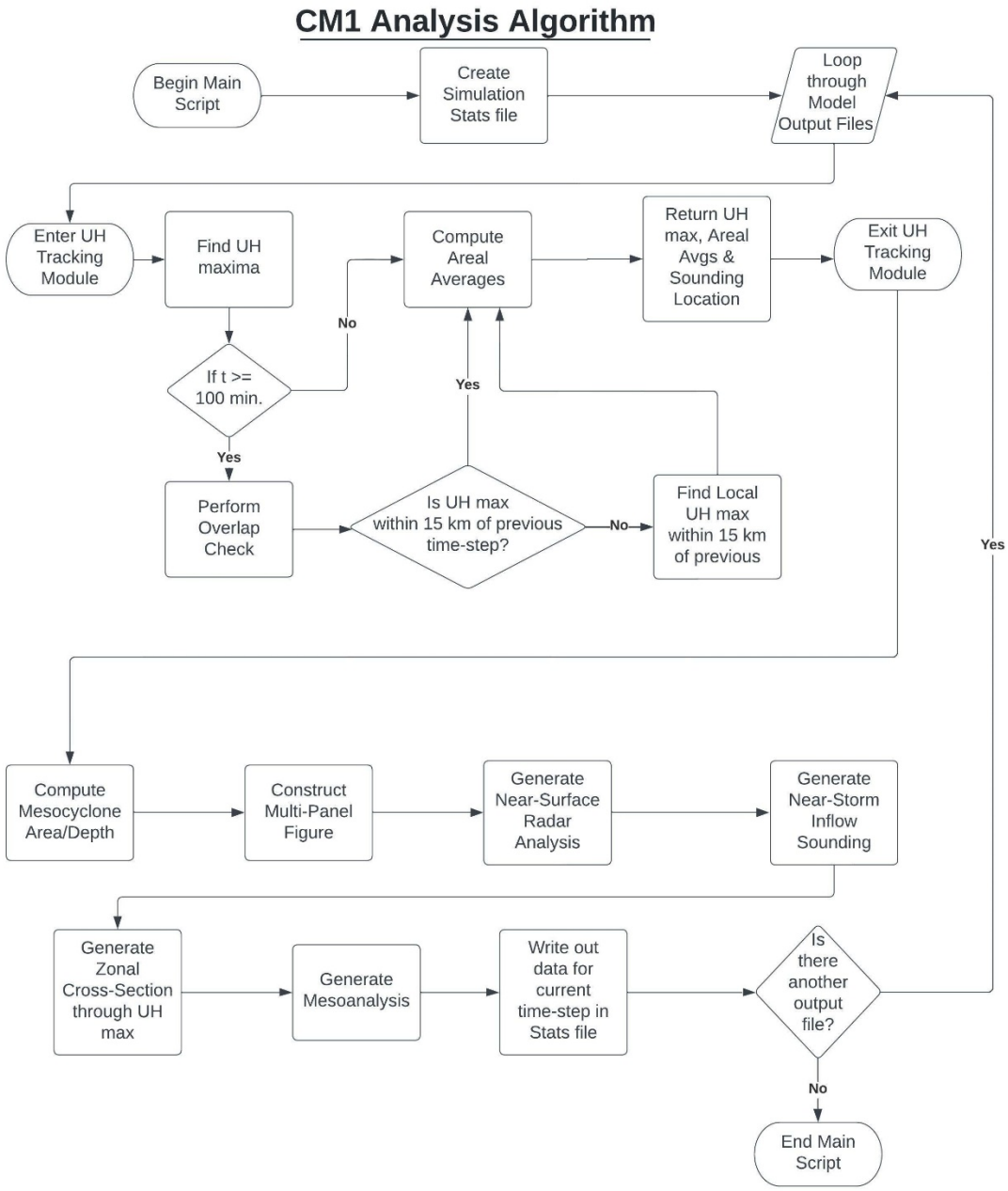

Figure 3.7 A flowchart algorithm that explains the decision-based logic for determining and tracking supercellular convection from the output CM1 model data implemented in our post-processing analysis script.

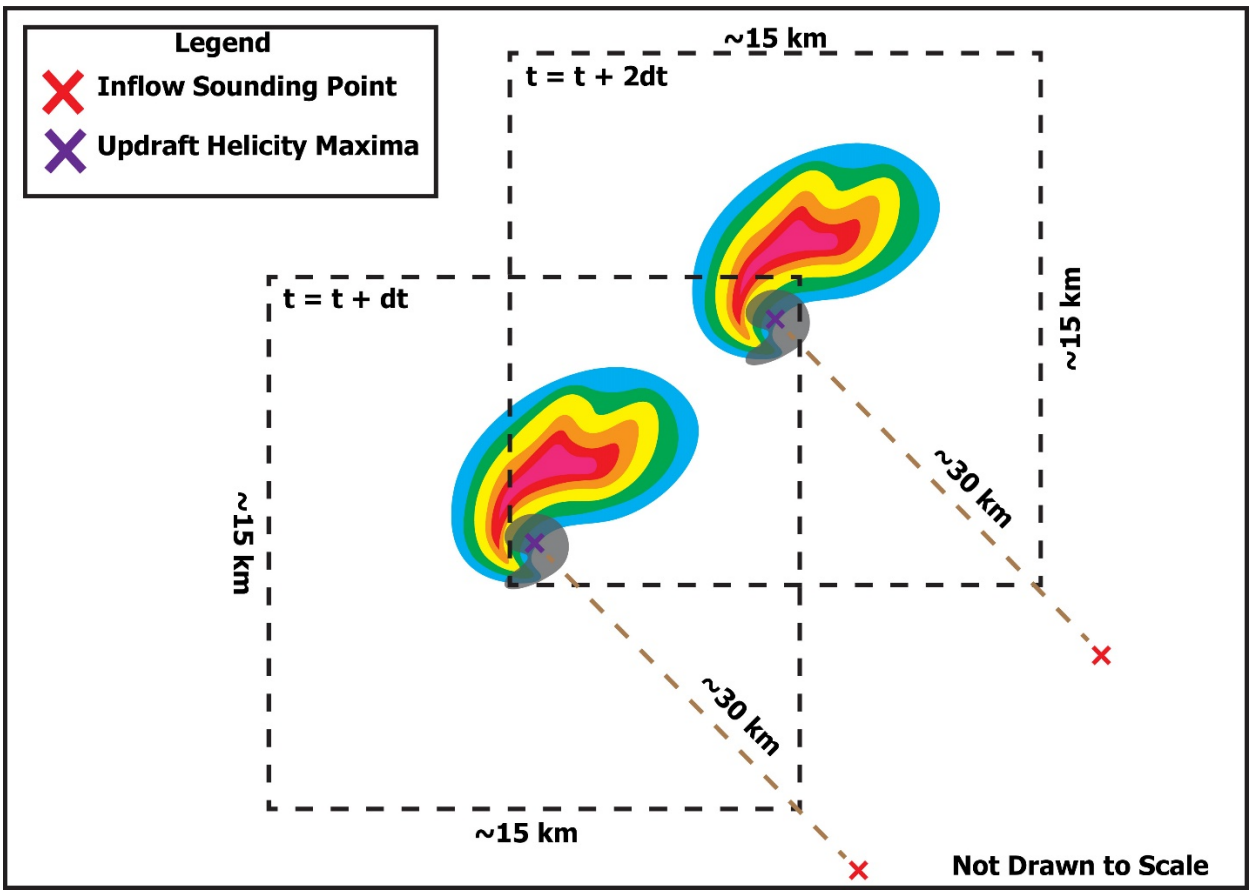

Figure 3.8 A conceptual diagram of our storm-tracking algorithm in action. Once activated, it identifies the absolute updraft helicity maximum (UH_{max}), then checked to see if its location is within 15 km of the location from the prior output file. If this overlap check fails, then the algorithm finds the local UH_{max} within the overlap area to ensure consistent tracking.

CHAPTER 4: RESULTS

4.1 Introduction

The following chapter elaborates on the results of each set of idealized experiments. The primary goal of these experiments was to provide additional insight into the interplay between complex terrain and the mesoscale environment in modulating supercell intensity and behavior. Such insight will be combined with the observational results from McKeown (2021) and Purpura et al. (2022) to improve our current conceptual model of supercell behavior when traversing complex terrain. The discussion is organized so that the level of realism increases throughout each section, beginning with the Idealized Terrain Simulations in Section 4.2.1, moving to the Realistic Terrain Simulations in 4.2.2. Within each section we will explore the differences between crossing and non-crossing environments on supercell morphology.

4.2 Individual Simulations

The following section discusses the spatiotemporal evolution of all simulations with a fixed, horizontally homogenous steady-state background environment. We begin by introducing the control simulations for both the upstream crossing (CS_CTL) and non-crossing (NC_CTL) to gain a solid understanding of the simulated storm these environments can produce without any environmental variability, terrain-induced or otherwise. We will then transition into the idealized terrain simulations (CS_TRN, NC_TRN) to explore the broad impacts that the Appalachians have on supercell morphology via an idealized bell-shaped terrain field that is representative of the Appalachian chain; the background environment is fixed over time, but varies horizontally as a result of the imposed terrain. We further investigate these broad impacts by exploring the sensitivity to the degree of cross-barrier flow in our modified hodograph simulations (CS_MOD, NC_MOD) while continuing to use the idealized terrain.

Section 4.2.2 explores more of the finer details of terrain-induced modulations via simulations utilizing a realistic terrain field derived from the USGS DEM model around the peak storm track density region to ensure our simulated storms interact with common terrain features from the observational studies. The discussion begins with focus on the simulations using full upstream composites as initial conditions (CS_RLTRN_ALL; NC_RLTRN_ALL) to evaluate any differences in storm evolution across the differing terrain configurations. We then explore the sensitivity of the 27 April 2011 Outbreak on the modeling results, given that this single event contributed to 9 of the 25 crossing cases, thereby substantially influencing the composite soundings; the simulations using stratified upstream composites as the initial conditions are revisited by testing the inclusion of cases from that single event. First, we look at simulations where the outbreak was removed from the composite environment (CS_RLTRN_NO_OUT; NC_RLTRN_NO_OUT) to elaborate on the more commonly observed supercell behaviors across the study area. Then, we transition to simulations using composites consisting of only the storms occurring during the outbreak (CS_RLTRN_OUT; NC_RLTRN_OUT) to isolate the outlying effects of the anomalous convective parameter space have on supercell behavior while traversing the Appalachian region.

4.2.1 Idealized Terrain Simulations

In all six idealized terrain simulations, our storm of interest begins as a large area of linear convection initiated via artificial updraft nudging to mimic frontal initiation. The southern-most flank of this cluster begins to develop supercellular characteristics in all six simulations and will be the focus of the individual analyses. The storm tracks and convective mode of all six steady-state idealized terrain simulations are summarized in Fig. 4.1.

Crossing Control (CS_CTL)

For CS_CTL, convection begins to organize into a supercellular mode between t= 90-105 min with the storm officially flagged as supercellular by the tracking algorithm at t= 110 min (not shown). Per a variety of storm metrics, including updraft helicity, mesocyclone depth, and mesocyclone area, the supercell continues to intensify, peaking at t= 195 min (Fig 4.2 a-c); at this time, the mesocyclone characteristics are above typical crossing thresholds seen in McKeown (2021), with about a 7.5 km deep and 7 km^2 area at z= 5 km. Following this peak, the supercell steadily weakens until it completely dissipates (cf. Figs. 4.2a-c and 4.3a), which occurs despite the convectively supportive steady-state background environment. It is suspected that internal storm processes contributed to demise; by t= 230 min, the surface cold pool weakened significantly (Figs. 4.2h and 4.3b), combined with some marginal storm-induced variability in the inflow environment leading to a small increase in LCL-LFC separation by about 50-75 hPa (not shown), the combination of which suggests there is not enough mesoscale forcing to maintain the adequate parcel ascent into the storm. As such, it loses supercellular characteristics by t= 250 min. The remnant convection continues to propagate northeastward and completely dissipates by t= 300 min (Fig. 4.3a).

Throughout the entire simulation the near-storm inflow environment remains favorable for supercellular convection and comparable to the upstream crossing composite from Purpura et al. (2022). The main finding from CS_CTL is that the near-storm environment does not natively evolve in a consistent manner with the observations. However, we suspect that this is a natural outcome from imposing a fixed background environment; as hypothesized in Purpura et al. (2022), environmental variability plays a key role in supporting sustained supercellular

convection. CS_TRN and CS_MOD are designed to address what role the terrain plays in the simulated supercell's evolution and will be discussed shortly.

Non-Crossing Control (NC_CTL)

NC_CTL initially evolves in an analogous manner to CS_CTL, as a messy convective cluster (not shown). The storm begins to take on supercellular characteristics around t= 110-130 min (Fig. 4.5a), though regular storm-splitting because of the linear hodograph (Fig. 3.1d) introduces some uncertainty in convective classification. However, using the algorithm as guidance, we subjectively classified this supercell as discrete by t= 135 min (25 min later than CS_CTL), as the algorithm had locked on to a supercell mode and the reflectivity appeared to be semi-discrete. The observational studies suggest that crossing supercells usually initiated slightly earlier (~1 hour or less) than the non-crossing counterparts (Purpura et al. 2022) suggesting our simulations are developing in a somewhat consistent manner to observed storms (Markowski and Richardson 2010).

The NC_CTL supercell has a clear cyclic pattern noticeable in all three-mesocyclone metrics, suggesting the storm does not reach a quasi-steady state as seen with CS_CTL. Instead, we see fluctuations in intensity, depth, and area throughout the entire simulation (Fig. 4.4 a-c). Peak intensity occurs at t =190 min, where the mesocyclone is significantly wider and deeper than seen in most observed non-crossing storms (McKeown 2021). However, the supercell is unable to maintain such intensity for an extended period. Note that the inflow environment remains stable throughout the mature stage, suggesting the cyclic nature of the supercell is a function of internal storm dynamics instead of environmental variability (Fig 4.4 a-f). Enhanced mesoscale forcing from a more consistent cold pool (Fig. 4.4h), along with smaller LCL-LFC

separation, likely trigger RFD surges leading to the variable intensity and cyclic nature observed in this simulation (Adlerman et al. 1999). This cyclic behavior is observed through t= 335 min when the storm becomes more elongated and falls below our defined supercell threshold. It holds together this linear structure though the end of the simulation (t=360 min; Fig. 4.5a). Linear transition was more common than dissipation with observed non-crossing storms, showing additional consistency with prior studies (i.e., McKeown 2021; Purpura et al. 2022).

Crossing Idealized Terrain (CS_TRN)

CS_TRN is designed to be identical in every manner to CS_CTL, except now we have introduced an idealized bell-shaped curve scaled to be broadly representative of the Appalachian Mountains as the model's lower boundary (see Fig. 3.3). As in prior studies (e.g., MD2011; Smith et al. 2016; Scheffknecht et al. 2017), we expect the inclusion of idealized terrain to modify the inflow environment of the simulated supercell. How the storm responds to such modulations, and whether it can successfully cross the idealized terrain will be key areas of discussion for this simulation.

CS_TRN initiates and develops in an analogous manner to CS_TRN, becoming a discrete supercell by t= 120 min (10 min later than CS_CTL) when it is approximately 160 km from the terrain peak. Rapid intensification follows, leading to a quasi-steady state and a peak intensity by t= 175 min (20 min earlier than CS_CTL) when it is ~115 km from the mountain peak (Fig. 4.6). During this intensification phase the mesocyclone depth remains relatively constant ~6 km and both the low and mid-level mesocyclones maintaining an area > 2 km^2 (Fig. 4.2a-c). The depth aligns well with the observed distributions of crossing supercell mesocyclone diameters which had a median value of ~5 km in McKeown (2021; see Fig. 2.32). The mesocyclone appears

vertically stacked throughout the depth which has been shown to be influential in enhancing near-surface circulation in prior literature (e.g., Guarriello et al. 2018; Brown and Nowotarski 2019) which may explain the presence of cyclonic vorticity in the lowest grid points during towards the end of this intensification phase (Fig. 4.6).

The inflow environment has remained comparable to CS_CTL through this point. A notable divergence begins around t= 200 min when the supercell approaches the steeper slope (< 100 km from the peak) of the idealized terrain (Fig 4.2d-g); this is consistent with the idealized experiments in MD2011 and Smith et al. (2016). Specifically, we see a decrease in MLCAPE (from roughly 1250 to 1000 Jkg^{-1}) and 0-3 km SRH (from roughly 300 to 200 m^2s^{-2}) when compared to CS_CTL during the storm's ascent upslope (Fig 4.2d-f). MD2011 showed that it is the ground-relative wind profile that dictates how the inflow environment is modulated. In this experiment, surface winds contain a significant southerly component which parallels the terrain contours, which results in little influence on the near-storm wind profile due to upslope flow. Even so, some terrain-blocking effects (seen in Smith et al. 2016) may be helping to spin-up additional horizontal vorticity available for vertical stretching during the initial ascent upslope. This would likely explain the longer quasi-steady intensity in mesocyclone metrics for CS_TRN when compared to CS_CTL (Fig 4.2a-c). Regardless of the cause for inflow modulation, a critical finding is that these changes do not reflect a transition towards the composite peak environment (see Fig 3.1b), which was characterized by significantly less favorable thermodynamics (~200 Jkg^{-1}) with enhanced helicity (~300 m^2s^{-2}) and shear in the 0-3 km layer (Purpura et al. 2022).

The supercell continues to weaken during its ascent along the windward slope, with the first clues unveiled at t= 225 min (Fig. 4.7) as the cold pool begins to rapidly weaken (Fig. 4.2h),

resulting in weaker mesoscale forcing for parcels into the updraft. Vertical vorticity through the storm's depth also decreases during this time, suggesting the remaining parcels do not contain appreciable baroclinically-generated horizontal vorticity for dynamic stretching, which is consistent with observed supercell dissipation (Zeigler et al. 2010; Davenport and Parker 2015). A continued decline in mesocyclone metrics and storm size continues through t= 235 min when our tracking algorithm identifies the storm as no longer supercellular. Even so, appreciable mesocyclone depth and area in the mid-levels calls for continued tracking on a subjective basis given the favorable inflow environment and the proximity to the peak (~75 km). The storm is subjectively considered non-supercellular by t = 255 min (5 min. later than CS_CTL), with a surface elevation just over 400 m, before reaching the mountain peak; and fully dissipates by t = 335 (35 min later than CS_CTL) on the leeside of the terrain. A review of the entire CS_TRN storm track (Fig. 4.1) shows that the inclusion of terrain results in a northward shift when compared to CS_CTL which is also seen in Smith et al. (2016). Figure 4.8a-f summarizes the CS_TRN simulation through an hourly time-series.

The root cause of the supercell's demise appears to be rooted in reduced cold pool forcing over time which can best be seen in Figs. 4.2h and 4.8b, between t= 3-4 hrs. Minimizing the forcing from the cold pool effectively reduced lift of parcels containing baroclinically-generated vorticity available for stretching to the LFC, resulting in a weakening mesocyclone upon the upslope ascent. As such, CS_TRN did not successfully cross the terrain as expected, nor did the inflow environment evolve in line with the observations. These findings are key to support the need for the MOD simulations, which are designed to emulate cross-barrier flow in a more realistic manner than was seen in CS_TRN. Recall the Appalachian spine is oriented from SW to NE by about 25° (see Fig. 1.1). The rotated hodographs could help to capture more of the

cross-barrier flow and lead to low-level shear modifications (which are modulated based on ground-relative winds per MD2011) which was observed while maintaining the idealized terrain configuration that is comparable to TRN. Minimal cross-barrier flow in CS_TRN may explain to some degree why we did not see the storm successfully cross or the expected evolution of the inflow environment in this simulation.

Non-Crossing Idealized Terrain (NC_TRN)

NC_TRN mimics the design of CS_TRN while utilizing the non-crossing upstream composite (Fig. 3.1d) as the initial background field. Again, the key focus of analysis is related to how the storm responds to terrain-induced modulations, and whether or not it can successfully cross the idealized terrain. However, unlike CS_TRN, the expectation is that the supercell will not cross the idealized ridge in this simulation. Differences between CS_TRN and NC_TRN should provide some insight regarding the superposition of terrain-induced environmental perturbations to create constructive and/or destructive convective environments. As such it is important to compare this simulation to both NC_CTL to uncover terrain induced differences, and CS_TRN to see how those differences vary across the differing background environments.

NC_TRN develops supercellular characteristics as early as t= 90 min, being officially flagged by the algorithm at t= 110 min (25 minutes earlier than NC_CTL). Storm-splitting does not cause any tracking disruptions such as those seen in NC_CTL. However, NC_TRN immediately experiences some mesocyclone variability upon its initial supercellular classification between t =125-155 min (Fig. 4.4a-c). Such fluctuations are likely a combination of a left-split interference and small storm size making it susceptible to internal dynamic variability. The supercell overcomes its initial struggles and intensifies again between t= 160-195

min. During this phase, we observed a weaker and less-organized cold-pool than NC_CTL, but still much more defined than seen in CS_TRN (Figs. 4.5 and 4.9b). The non-crossing upstream composite (Fig. 3.1d) is characterized by drier mid-level air than the crossing upstream composite (Fig. 3.1a), which can enhance evaporative cooling and thus stronger and more consistent cold pool signals from the NC simulations (Fig. 4.4h).

NC_TRN reaches a peak intensity at t= 210 min, maintaining such strength through t = 225 min. So far, the NC_CTL mesocyclone has been more intense, deeper, and composed of a larger area. During NC_TRN peak intensity, the mesocyclone area at 3 and 5 km exceeds higher values than observed during the NC_CTL or CS simulations, approaching 10 km^2 at 5 km (Fig. 4.4c), which appears to be wider than observed non-crossing storms (see Fig. 2.32; McKeown 2021). NC_TRN is about 110 km from the mountain peak at this time, meaning it is approaching the more significant slope of the terrain. The near-storm inflow environment has experienced very little change through this point in integration and as such, the modeled environment exhibits more favorable conditions for supercellular convection than was observed in non-crossing storms approaching elevated terrain (Purpura et al. 2022). This result supports the need for the variable base-state simulations in the future, which would allow for changes to be made to the background field that reflect a realistic transition from upstream to peak composite environments.

Another interesting observation during the peak intensity phase is the apparent pooling of favorable CAPE and 0-1 km SRH along the windward edge of the terrain (Fig. 4.9). The SRH field in particular parallels the terrain peak suggesting terrain blocking is maintaining low-level shear. We refrain from using the term “enhanced” here as both the vertical shear and SRH time-series (Fig. 4.4e-f) remain steady throughout the storm’s lifecycle. Also, note that the near-

surface flow is nearly parallel to the terrain contours limiting any orographic enhancements. As such, the terrain is likely maintaining a favorable supercell environment in this simulation. SRH does not vary significantly between NC_CTL and NC_TRN, but the pooling along the terrain spine was not observed in NC_CTL (not shown), leading to these speculations. This may also help explain why NC_TRN maintains intensity longer than NC_CTL.

NC_TRN quickly weakens post-peak intensity, which appears to be associated with strong outflow undercutting the mesocyclone via RFD surges (Fig. 4.9b). The strong outflow appears to initiate linear transition between t= 230-270 min (consistent with observed non-crossing storms dissipating in this manner more commonly than crossing storms; Purpura et al. 2022), while the storm loses supercellular characteristics (i.e., hook-echo, BWER, reflectivity gradient, etc.) without dissipating (65 min. earlier than NC_CTL). The storm was approximately 65 km away from the terrain peak, with a surface elevation of 300 m, when identified as linear at t= 270 min. Figure 4.9a-f summarizes the entire NC_TRN simulation through an hourly time-series.

Overall, NC_TRN's inflow environment appeared to reflect the observed variability towards the non-crossing peak composite (Fig. 3.1d-f), producing an overall reduction in thermodynamics (to ~500 Jkg^{-1}) but steady kinematics (0-3 km SRH ~200 m^2s^{-2}) by the end of the supercell's lifecycle (Fig. 4.4d-f). Though it is important to remember that the downstream composite (Fig. 3.3f) truly represents the dissipation/transition environment. As such, the is still some degree of environmental heterogeneity not being captured by the model, supporting the need to revisit these simulations utilizing techniques to capture horizontal environmental heterogeneity, such as Base-State Substitution (BSS; Letkewicz et al. 2013; Davenport et al. 2019). Additionally, even though NC_TRN did not traverse to far upslope (peak elevation ~

300m), it is still important to explore the sensitivity of cross-barrier flow on the non-crossing environment via NC_MOD.

Crossing Modified Hodograph (CS_MOD)

The MOD simulations were designed to test the sensitivity of the upstream composite environments with a more realistic degree of cross-barrier flow seen during observed storms. Given the identical environments to the TRN simulations, the discussion will be centered on whether cross-barrier flow results in more terrain-induced environmental variability and how the simulated supercell responds to those differences.

CS_MOD develops into a discrete supercell by t= 100 min. (20 min. earlier than CS_TRN), (Fig. 3.8). The mesocyclone is notably larger (~2 km^2) and deeper (~ 2 km) during the intensification phase than seen in the other CS simulations (Fig. 4.2b-c). CS_MOD rapidly intensifies to an overall peak intensity by t= 125 min. (Fig 4.2a), which is significantly earlier than the other two CS simulations (CS_CTL peak intensity occurred at t=195 min, and CS_TRN at t= 175 min.). Storm-scale dynamics appear to be responsible for the rapid intensification as the near-storm inflow environment does not vary significantly from the other simulations and CS_MOD is still well away from any significant terrain (Fig. 4.2d-f).

CS_MOD then weaken some before becoming quasi-steady through t= 150-200 min. Up through this point it maintained a well-defined mesocyclone supported by all three metrics (Fig. 4.2a-c). At t= 200 min. the storm is approximately 100 km away from the peak with surface wind clearly having more of an upslope component. This provides additional orographic lift, which was shown to enhance cold pool forcing through enhanced precipitation production in Smith et al. (2016). CS_MOD has consistently shown a larger precipitation field via radar reflectivity than

the other two CS simulations, suggesting terrain-enhanced precipitation via orographic lifting is also occurring in this simulation which maintains the cold pool forcing longer than we saw in CS_TRN (Figs. 4.2h, 4.8, and 4.12).

CS_MOD undergoes a weakening phase between t = 205-245 min which closely resembles the intensity decline seen in both CS_CTL and CS_TRN (Fig 4.2a). The additional orographic lift maintains trailing convection causing competition for inflow. It quickly becomes impractical to attempt to decipher which influences are terrain-related as CS_MOD is no longer discrete. As such, CS_MOD is no longer considered supercellular at t= 250 min., which is roughly the same time as the other CS simulations were unflagged. The remnant convection of CS_MOD continues to decay through t= 300 min. when it finally dissipates just at the terrain peak. Fig 4.12 a-f summarizes the entire CS_MOD simulation through an hourly time-series.

Non-Crossing Modified Hodograph (NC_MOD)

NC_MOD is first identified as a semi-discrete supercell at t= 125min (10 min. earlier than CTL, 15 min. later than TRN). It varies from the other NC simulations initially due to a much more elongated radar-reflectivity field and stronger cold pool by about 1-2 K (Fig. 4.4h). These differences are most likely attributed to the updraft nudging effectively initiating more convection than seen in the other simulations, though the settings are identical in location and intensity across all six simulations. NC_MOD reaches an overall peak intensity (Fig. 4.13) at t = 165 min (~ 30 min. earlier than CTL and TRN). The intensity magnitude (based on areal UH avg) is comparable to NC_TRN and slightly weaker than NC_CTL (Fig. 4.4a). Mesocyclone area at both z= 3 and z= 5 km quickly ramps up during intensification and maintains a quasi-steady state around 7-9 km^2 at z= 5 km for the longest duration of any of the six simulations

(compare Figs. 4.2.c and 4.4c). Mesocyclone area has been notably larger in the NC simulations than expected based on the results of McKeown (2021) alone. This is likely an artifact of a larger updraft due to a combination of stronger cold-pools and linear transition and does not suggest that NC supercells are necessarily wider than CS storms, where confidence in this metric is higher due to a more pro-longed discrete supercell mode than seen with NC simulations. NC_MOD in particular struggles the most to be discrete during its time as a supercell given the increased convection during initiation and continual left-splits.

NC_MOD does not maintain peak intensity long and begins to weaken between t= 170-200 min. The inflow environment remained marginally favorable for supercellular convection given MLCAPE ~800 Jkg^{-1}, 0-3 km SRH ~250 m^2s^{-2}, and minimal CIN during this period. Storm-scale dynamics appear rather healthy throughout this period as well given the enhanced 0-1 km SRH field co-located with a well-defined hook-echo at t= 180 min. (Fig. 4.14a-d). The mesoanalysis during this output time provides insight suggesting outflow from the trailing storm is amplifying the RFD. In the short-term this is favorable and maintains the storm by provide ample baroclinically-generated horizontal vorticity for dynamic stretching almost directly under the updraft. We also see the CIN > 50 Jkg^{-1} field (Fig. 4.14d) beginning to approach the updraft region of NC_MOD, which continues to spread overtime. By t= 200 min the RFD has completely undercut the mesocyclone effectively weakening the storm as the two convective cells begin to merge. Given that the storm is still ~150 km from the terrain peak, it is unlikely experienced any significant modulations during this time.

NC_MOD can no longer be declared discrete past t= 200 min, though it does continue to show some supercellular characteristics as linear transition continues. By t= 240 min the remnant NC_MOD has completely merged with trailing convection, taking on a QLCS appearance (Fig

4.15). It is completely outflow dominant and still ~ 110 km from the terrain peak. We end our analysis here even though there is a brief period where it regains semi-discrete supercellular characteristics (t= 295-320 min.) as differentiating terrain-influences from convective interference would be too convoluted. We will note of some enhanced FFD-like precipitation at t= 320 min. (Fig. 4.16 when the remnant storm is ~70 km from the terrain peak, which likely is enhanced by upslope flow as we seen in CS_MOD. The storm quickly returns to a more linear mode by the end of the simulation (t = 360 min.) about 40 km from the peak. Evidence for the linear transition and outflow dominance can be seen in the hourly time-series for NC_MOD as well (Fig. 4.17).

Overall, comparison between MOD and TRN simulations highlights two different terrain-induced perturbation mechanisms that modulate our simulations. In both CS_TRN and NC_TRN, the terrain largely leads to blocking effects that maintained vertical wind shear in the 0-3 km layer, which should be pertinent for prolonged supercellular convection. CS_MOD showed little evidence of blocking, but obvious impacts via orographic lift on the windward slope amplifying precipitation production. This was briefly observed in NC_MOD as well, though that supercell did not remain discrete long enough for effective analysis. None of the simulation results in successful crossing (i.e., sustain supercellular storm characteristics in the lee of the terrain peak), suggesting that there is a fine balance between both types of terrain-effects required to realize the environment that maintain a supercell upon its ascent. It is likely the idealized terrain field is not complex enough the accurate emulate the observed terrain-induced effects as was seen in studies such as Scheffknecht et al. (2017), supporting the need for the RLTRN simulations. Also, note that the crossing composites are highly skewed by synoptic influences of the 27 April 2011 outbreak. Such synoptic-scale support would not be well

emulated by an idealized mesoscale model and should also be considered when determine how crossing supercells successfully traverse complex terrain.

4.2.2 Realistic Terrain Simulations

In all six realistic terrain simulations, our storm of interest begins as a large area of linear convection initiated via artificial updraft nudging to mimic frontal initiation. The southern-most flank of this cluster attempts to develop supercellular characteristics in all six simulations and will be the focus of the individual analyses. Five of the simulations resulted in the development of a discrete supercell, which is the base requirement for continued analyses. The discussion regarding the one simulation that failed to produce a supercell will include some insight as to why sustained convective maintenance of a supercell failed to occur. Also, using realistic terrain introduced an additional caveat to our study. Each simulated supercell will be highly sensitive to the location of convective initiation and resultant storm track with respect to the underlying terrain. The initiation location for each simulation (Table 4.1) was experimentally selected via trial and error with the goal of producing a prolonged supercell. As such, the simulations cannot possibly capture all possible outcomes. However, the results still address our primary goal to improve the understanding of supercell behavior in the Appalachians. The storm tracks of all five steady-state realistic terrain supercells are summarized in Fig. 4.18.

Crossing Realistic Terrain Full Composite (CS_RLTRN_ALL)

CS_RLTRN_ALL quickly develops into a discrete supercell by t= 210 min, roughly 90 minutes after CI. The developmental stage is slightly faster than seen in the CS idealized simulation by about 20 minutes, further supporting the general notion that crossing storms tend to develop faster than their non-crossing counterparts, largely due to environmental differences

in the upstream hodographs (Figs. 3.1a and d; Purpura et al. 2022). The mesocyclone is initially robust and continues to intensify (Fig. 4.19a-c) while approaching the western periphery of the realistic terrain field. The storm quickly achieves peak intensity by t= 230 min (Fig. 4.20) with a large (z= 5 km area ~ 9 km^2), deep (~9 km), and intense mesocyclone (UH_{avg} ~ 500 m^2s^{-2}). Both the mid- and lower-level mesocyclones also appear to be vertically stacked which can enhance dynamic stretching processes (Brown and Nowotarski 2019). CS_RLTRN_ALL appears to become quasi-steady from this point forward as it begins to track upslope into more variable terrain.

All three-mesocyclone metrics begin to wane after peak intensity (Fig. 4.19a-c), with the most remarkable decline noted in the 3 and 5 km mesocyclone area between t= 240-280 min. The base elevation of the inflow sounding gently increases to about 200 m during this period as well while remaining favorable for supercellular convection (Fig. 4.19d-g). Structural changes such as the dissipation of the hook echo and increasing hydrometer advection downstream into the FFD suggest the storm is weakening (Ziegler et al. 2010; Davenport and Parker 2015). Additionally, the cold pool has been shrinking and warming since the storm reached peak intensity (Fig. 4.19h) which has been a reoccurring observation during the dissipation stages of our CS simulations. This trend continues through t= 300 min when the cold pool has essentially dissipated. The supercell persists a bit longer, likely due to terrain-channeling providing some short-term dynamic enhancements as the storm parallels a localized valley (Bunker's Right Motion ~ 250°; Figs. 4.18 and 4.21). The storm becomes unflagged by the algorithm at t= 320 min and slowly continues to wane, dissipating by t= 380 min. Figure 4.22 a-f summarizes the entire CS_RLTRN_ALL simulation through an hourly time-series.

Comparison of CS_RLTRN_ALL with CS_TRN highlights the impacts of the realistic terrain field on supercell morphology. Both simulations produce robust, long-lived (~2 hrs), and discrete supercells that dissipate during upslope ascent (Figs. 4.2 and 4.19a-c & h). Unsurprisingly, realistic terrain results in more environmental heterogeneity than idealized terrain (Figs. 4.2 and 4.19d-f), as expected (e.g., Scheffknecht et al. 2017). Thermodynamic parameters in particular show the most variability, highlighting the role of the ground-relative wind profile interacting with the terrain to weaken or enhance relative humidity and related parameters (e.g., MD2011; Katona et al. 2016). Most importantly, the environmental heterogeneities were unfavorable for continued supercell maintenance in CS_RLTRN_ALL. An inverse relationship between mesocyclone intensity (UH_{avg}) and inflow sounding elevation (Fig. 4.19a & h) eludes to a simple dynamical rationale as to why the storm dissipated. Conservation of potential vorticity suggests that as the atmospheric column is compressed by the increasing surface elevation, rotational velocity must decrease (Prociv 2012). With this in mind, the combination of vorticity compression and reduced cold pool forcing (Fig. 4.19h) provides a plausible argument as to why CS_RLTRN_ALL dissipated before crossing the entire terrain field.

Non-Crossing Realistic Terrain Full Composite (NC_RLTRN_ALL)

NC_RLTRN_ALL also quickly develops into a discrete supercell by t= 220 min, roughly 100 min after CI. There are significant modulations to the inflow environment from the base-state (Fig. 3.1d) noticeable at this time. MLCAPE has fallen from roughly 900 to 600 Jkg^{-1}, while SRH increased from 200 to 300 m^2s^{-2} in the 0-3 km layer (Fig 4.23d-f).

Thermodynamic variability is a result of the model environment adjusting to the terrain field before CI (Katona and Markowski 2021). Though there is sufficient evidence to show that the SRH enhancements are terrain-induced via blocking. Inflow winds are out of the south-southeast paralleling a north-to-south oriented ridge line. The 0-1 km SRH > 200 m^2s^{-2} field contours are spatially correlated with this ridge in the mesoanalysis (Fig. 4.24d). These kinematic enhancements continue through t= 240 min, which is about the time the supercell moves east of the localized terrain peak responsible for the blocking effect.

NC_RLTRN_ALL remains quasi-steady for most of its life, with the only variable mesocyclone metric being the area (Fig. 4.23a-c). Both the 3 km and 5 km areas quickly reach their respective peaks around t= 250 min. This also coincides with a peak in the cold pool area (~500 km^2) and intensity (-5 K; Fig. 4.23h). It appears that the mesocyclone area metrics were temporarily inflated due to cyclic behavior initiated by an RFD surge between t=255-275 min (not shown), resulting in structural variability. The storm survives these disruptions and continues to track through an east-to-west oriented valley (Fig. 4.18). Between t= 290-320 min., inflow is channeled through a southern opening in the valley, resulting in a brief intensification period.

Channeling effects appear to be highly localized to the immediate storm environment (~20 km from the updraft), making it difficult to quantify the enhancements. However, the storm does reach an overall peak intensity at t= 305 min, when there is a clear localized enhancement of the 0-1 km SRH field in the mesoanalysis (Fig. 4.25d). The 200 m^2s^{-2} SRH contour shows a strong correlation with the valley opening, supporting the argument for terrain-channeled enhancements. Such enhancements appear responsible for maintaining the storm as it immediately loses supercellular characteristics at t= 330 min, after passing the valley opening.

The remnant convection persists through the rest of the simulation (t= 480 min). Figure 4.26 a-f summarizes the entire NC_RLTRN_ALL simulation through an hourly time-series.

Comparison of NC_RLTRN_ALL with NC_TRN continues to highlights the impacts of the realistic terrain field on supercell morphology. Each supercell exhibited a fairly different evolution highlighting the sensitivity of storm morphology on exact positions of interaction and the details of the terrain (e.g., slope, elevation). NC_TRN maintained supercellular properties longer (~45 min) than NC_RLTRN_ALL, likely attributed to a more stable inflow environment and weaker terrain-induced modulations over time (Figs. 4.4 and 4.23d-f). Both exhibited evidence of RFD surges resulting in structural modifications. In NC_TRN this ultimately results in upscale growth due to stronger cold pool (Fig. 4.4h). NC_RLTRN_ALL maintained supercellular characteristics due to a weaker cold pool and terrain-channeling enhancing ambient helicity, effectively maintaining the updraft (e.g., Bosart et al. 2006; Tang et al. 2009; LeBel et al. 2021). These evolutionary differences highlight the role more realistic terrain plays in maintaining a supercell in an otherwise hostile environment. Again, realizing such enhancements is a critical function of storm track with respect to the underlying terrain.

Crossing Realistic Terrain Outbreak Removed (CS_RLTRN_NO_OUT)

CS_RLTRN_NO_OUT is initiated from the upstream composite environment of the 16 observed crossing supercells that occurred outside of the 27 April 2011 Super Outbreak (Fig. 3.7a). It is first flagged as a discrete supercell at t= 215 min, located approximately 30 km from the western periphery of the realistic terrain field. The mesocyclone is significantly weaker (UH_{avg} ~ 150 m^2s^2), smaller ($Area_{5km}$ ~0.5 km^2), and shallower (Depth ~ 4.0 km) than seen during the development of the other CS simulation (Figs. 4.2 and 19a-c), which emphasizes the

impact of the outbreak environment on the full composite. This notion is highlighted further when the storm reaches peak intensity at t= 240 min, just 25 minutes after becoming supercellular (Fig. 4.27). Terrain-blocked inflow from a localized north-to-south oriented ridge is likely enhancing SRH in a similar manner discussed during the development of NC_RLTRN_ALL. The enhancement is a notable increase from the base-state environment by roughly 100 m^2s^{-2} and is likely crucial to the maturation of the mesocyclone.

CS_RLTRN_NO_OUT quickly weakens between t=245-260 min during its initial approach to the realistic terrain field. The blocking effects continue through this period but appear to be negated by several other factors. The most notable being a rapid trend towards a more hostile thermodynamic inflow environment. MLCAPE is effectively reduced from 900 to 500 Jkg^{-1}, MLCIN remains around -50 Jkg^{-1} (Fig. 4.19d), and steady LCL-LFC separation of about 50-75 hPa during this time (not shown). Simultaneously, the cold pool shrinks by about 250 km^2 while warming by about 1.5 K (Fig. 4.19h). The storm is passing just north of some localized ridge, suggesting southerly low-level flow is moving downslope (Fig. 4.27a) resulting in unfavorable thermodynamic modifications. The supercell is unable to maintain a robust mesocyclone in this environment and becomes unflagged by the algorithm at t=265 min. Figure 4.28 a-f summarizes the entire CS_RLTRN_NO_OUT simulation through an hourly time-series.

Though its lifecycle is significantly short compared to the other simulations, these results continue to reflect how sensitive supercell maintenance is to its track across the complex terrain. This simulation presented a case where a marginal supercell was highly sensitive to terrain-induced modulations. The initial blocking effects helped to prime the kinematic environment for supercellular convection by doubling the base-state 0-3 km SRH (~300 m^2s^{-2}). However, the marginal base-state thermodynamics (~900 Jkg^{-1}) quickly became unfavorable for continued

supercellular convection as result of downslope flow modifications. Also remember that the model environment is spatially homogeneous (except for terrain-induced perturbations). Therefore, synoptic scale forcing is not emulated and could be critical for maintenance in hostile environments as well. Future studies should consider an ensemble approach wherein multiple initiation locations and track speeds are tested using realistic terrain to fully assess the spectrum of storm behaviors and longevity.

Non-Crossing Realistic Terrain Outbreak Removed (NC_RLTRN_NO_OUT)

NC_RLTRN_NO_OUT is initiated from the upstream composite environment of the 34 observed crossing supercells that occurred outside of the 27 April 2011 Super Outbreak (Fig. 3.7d; Purpura et al. 2022). As such, the stratified composite environment varies little from the full composite used in NC_RLTRN_ALL (Fig. 3.2d). We chose to initiate NC_RLTRN_NO_OUT further east (75 km; Table 4.1) to further explore supercell sensitives to storm track and intensity during terrain interactions. The results of this simulation will be compared with NC_RLTRN_ALL to emphasize such sensitivities.

NC_RLTRN_NO_OUT is first flagged as a discrete supercell at t= 220 min., roughly 100 min after CI. Thermodynamic parameters are marginal (MLCAPE ~750 Jkg^{-1}, MLCIN ~25 Jkg^{-1}) but remain stable as the storm continues to intensify (Fig. 4.23d). SRH is notably higher than the base-state environment (~100 m^2s^2) while the storm was approximately 80 km from any localized terrain peaks. Smith et al. (2016) found that blocking effects enhance inflow and could be observed as far as 100 km away from the mountain peak, supporting the argument that the SRH enhancements are terrain-induced. The supercell reaches an overall peak intensity (UH_{avg} ~ 300 m^2s^{-2}) at t= 240 min. During this time the 0-1 km SRH > 100 m^2s^{-2} field shows a strong

spatial correlation with the western terrain field, extending ~30 km out towards the supercell's inflow environment further supporting blocking enhancements (Fig. 4.29d).

NC_RLTRN_NO_OUT quickly experiences a prolonged period of structural variability post-peak-intensity, primarily induced by RFD surges between t= 245-310 min. The cold pool remains large (~500 km^2) and intense (-5 K) throughout the simulation (Fig. 4.24h), showing more agreement with the NC idealized terrain simulations than NC_RLTRN_ALL. Both mesocyclone area and depth show a cyclic pattern during this period (Fig. 4.23b-c), emphasizing the effects of the RFD surge. The earlier discussed blocking effects may be partially responsible for the RFD surges due to enhanced precipitation production as discussed in Smith et al. (2016). The storm appears to recover by t= 330 min; however, the radar structure is more elongated which could be indicative of upscale growth (Fig. 4.30a). A waning cold pool (250 km^2) along with an orographically enhanced FFD appear to prolong a supercellular mode through t= 375 min. The storm then again exhibits subjective signs of upscale growth and becomes unflagged by the algorithm at t= 410 min. A linear convective mode is observed through the rest of the simulation, t= 480 min. Figure 4.31 a-f summarizes the entire NC_RLTRN_NO_OUT simulation through an hourly time-series.

Overall, NC_RLTRN_NO_OUT showed more consistency with the NC idealized terrain simulations than NC_RLTRN_ALL. Specifically, we observed a more constant inflow environment along with linear transition in NC_RLTRN_NO_OUT. NC_RLTRN_ALL exhibited much more terrain-induced horizontal heterogeneity (Figs. 4.4 and 4.23d-g), likely attributed to its track through the east-to-west oriented valley. NC_RLTRN_NO_OUT encountered more localized peaks likely contributing to the continual variability noted before becoming linear (Fig. 4.18). Both NC RLTRN simulations exhibited smaller and warmer cold

pools during their encounters with the terrain (Figs. 4.22 and 4.31b). This suggests the more complex terrain field is disruptive to cold pool maintenance given the more consistent cold pool metrics from the idealized terrain simulations (Figs. 4.4 and 4.23h). All of our simulations highlight cold pool forcing as a key area of interest in supercell maintenance while traversing complex terrain. Additional work is needed to gain a better understanding of the factors influencing the cold pool variability seen in our simulations.

Crossing Realistic Terrain Outbreak Only (CS_RLTRN_OUT)

CS_RLTRN_OUT is initiated from the upstream composite environment of the 9 observed crossing supercells that occurred during the 27 April 2011 Super Outbreak (Fig. 3.6a; Purpura et al. 2022). It is first flagged as a discrete supercell at t = 215 min as it approaches the western periphery of the terrain field. The anomalous base-state shear parameters associated with the 27-28 April 2011 Super Outbreak (Knupp et al. 2014) appear to be amplified by terrain-blocking effects during the storm's developmental stage (Fig. 4.19e-f). Some shear augmentation is also likely contributed to strong pressure perturbations associated with the incredibly large (mesocyclone area at 5 km ~ 7 km^2), deep (9 km), and intense mesocyclone (UH_{avg} > 700 m^2s^2) generating dynamically forced accelerations within the inflow region. Additionally, the storm is traversing between two localized ridges likely leading to terrain-channeled accelerations on parcels being recycled into the updraft from the FFD region. This notion is consistent with development and intensification of observed supercells due to terrain-channeled flow during the 2011 Outbreak (Gaffin 2012). The combination of these processes results in a significant lengthening of the 0-3 km hodograph when compared to the base-state environment (~300 m^2s^2

increase in 0-3 km SRH). As a result, CS_RLTRN_OUT quickly reaches its peak intensity early in the simulation, at t= 235 min (Fig. 4.32).

CS_RLTRN_OUT then reaches a quasi-steady state as it continues to track deeper into the terrain field, indicated by minimal variability in the mesocyclone depth and area metrics between t= 240-325 min (Fig. 4.19b-c). Mesocyclone intensity does begin to wane immediately after peak intensity, though remaining well above our supercell threshold, while showing an inverse relationship with the inflow sounding elevation (Fig. 4.19a and f). Complimenting this relationship is a marginal decrease in MLCAPE during the same period (~250-300 Jkg^{-1}), showing some minor thermodynamic variability due to terrain interactions (e.g., MD2011; Katona et al. 2016). By t= 315 min the supercell begins to rapidly weaken. The primary mechanisms responsible for this decline appear to be a combination of downslope enhanced CIN and reduced cold pool forcing (Area < 100 km^2), the latter has been detrimental in all other CS simulations (Fig. 4.19h).

Mesoanalysis at t= 300 min. (Fig. 4.33c-d) shows a downslope enhanced CIN field encroaching up the immediate upstream portion of the storm track, also consistent with MD2011. The CIN field is located just north of series of local north-to-south oriented peaks experiencing strong southerly low-level flow. While the inflow region remains favorable, the local storm environment is becoming more capped with time. Unfavorable thermodynamics combined with reduced cold pool forcing quickly weaken the mesocyclone. By t = 330 min, the algorithm no longer considers the storm to be supercellular. Convection persists with some variable supercellular characteristics between t= 335-365 min while continuing to weaken. The remnant CS_RLTRN_OUT officially dissipates at t= 395 min., after a long track through the middle of

the realistic terrain field. Figure 4.34 a-f summarizes the entire CS_RLTRN_OUT simulation through an hourly time-series.

Overall, CS_RLTRN_OUT showed substantial consistencies with prior observational and modeling studies. Most notably this simulation highlights the overlap of favorable enhancements to maintain supercellular convection while interacting with complex topography. The most significant enhancements occurred early in the supercell's lifecycle when blocking/channeling effects combined with orographic ascent were both sources of vorticity-rich inflow to amplify the mesocyclone (e.g., Bosart et al. 2006; Gaffin 2012; Smith et al. 2016; LeBel et al. 2021). Conversely, as the storm continued onward through the terrain field, it encountered enhanced CIN because of downsloping wind, effectively capping the updraft resulting in rapid weakening (MD2011). Additionally, we did not see any conclusive evidence of vortex stretching during the storm's descent off any local terrain peaks as would be expected based on Prociv (2012). While the storm failed to cross the terrain in its entirety, the results still paint a clear picture that terrain-enhancements can significantly amplify an already favorable convective environment to maintain supercellular convection in areas of complex terrain.

Non-Crossing Realistic Terrain Outbreak Only (NC_RLTRN_OUT)

NC_RLTRN_NO_OUT is initiated from the upstream composite environment of the 3 observed non-crossing supercells that occurred during the 27 April 2011 Super Outbreak (Fig. 3.6d). It is the only simulation that failed to produce a discrete supercell for analysis. The base-state environment is characterized by weak thermodynamics (MLCAPE ~ 500 Jkg^{-1}), which is further modified by the introduction of realistic terrain (Not shown). As such, CM1 is unable to initiate sustained deep convection from this environment. Crossing supercells accounted for 75%

of the 27 April 2011 Outbreak storms (Purpura et al. 2022). As such, CS_RLTRN_OUT provides sufficient insight to the outbreak exclusive simulations. Failure for sustained convection in this simulation appears to be a modeling limitation. Though one could argue that convective failure also highlights the role of synoptic scale forcing in realizing the more marginal supercell environments. Regardless, convective failure for this small subset of non-crossing cases does not significantly affect the overall results of the study.

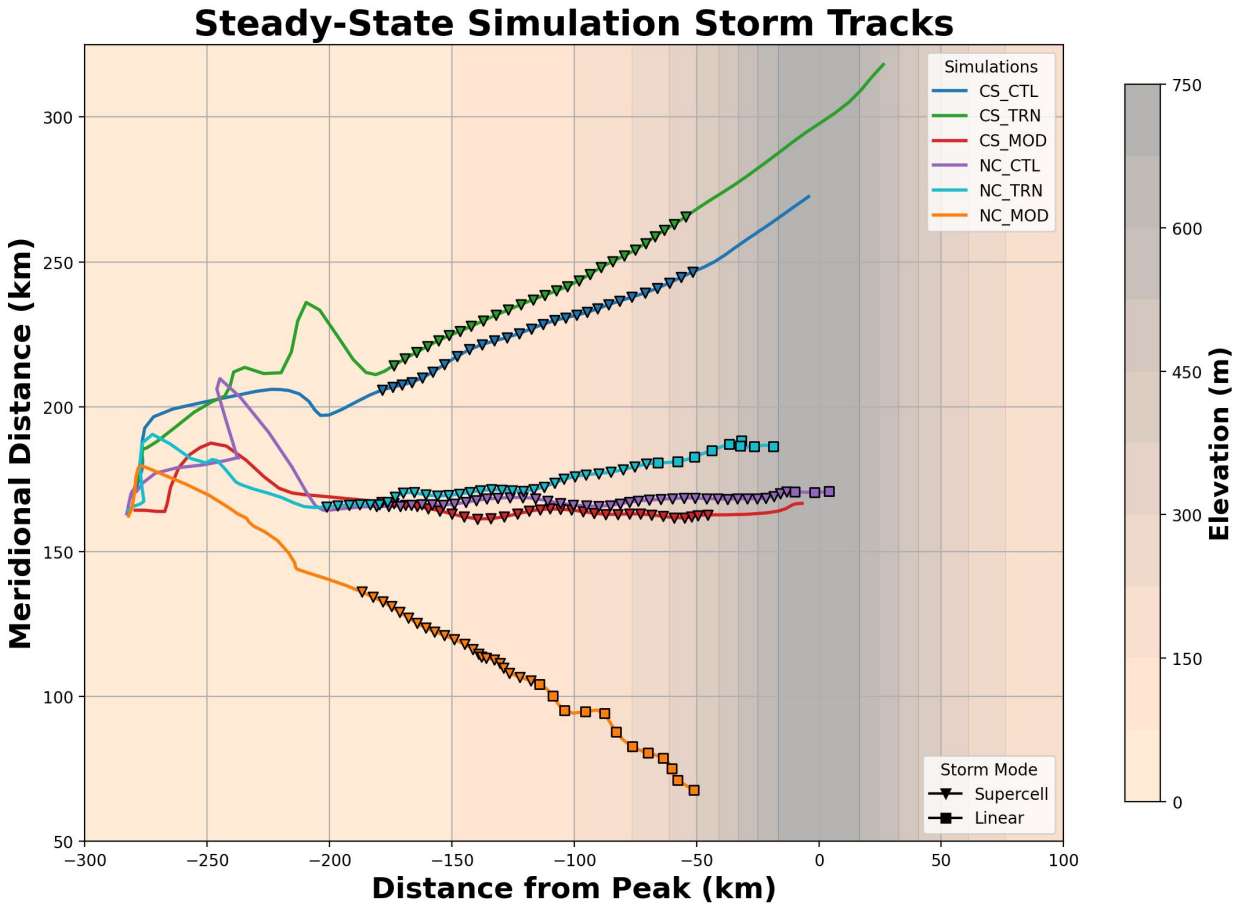

Figure 4.1: 1.0-sigma Gaussian filtered storm track from the six steady-state simulations (colored lines) with markers to demarcate storm mode (cone for supercell, square for linear) overlaid on the idealized terrain field (filled contour). Lines are drawn from initiation until each individual storm dissipates (radar reflectivity < 40 dBZ).

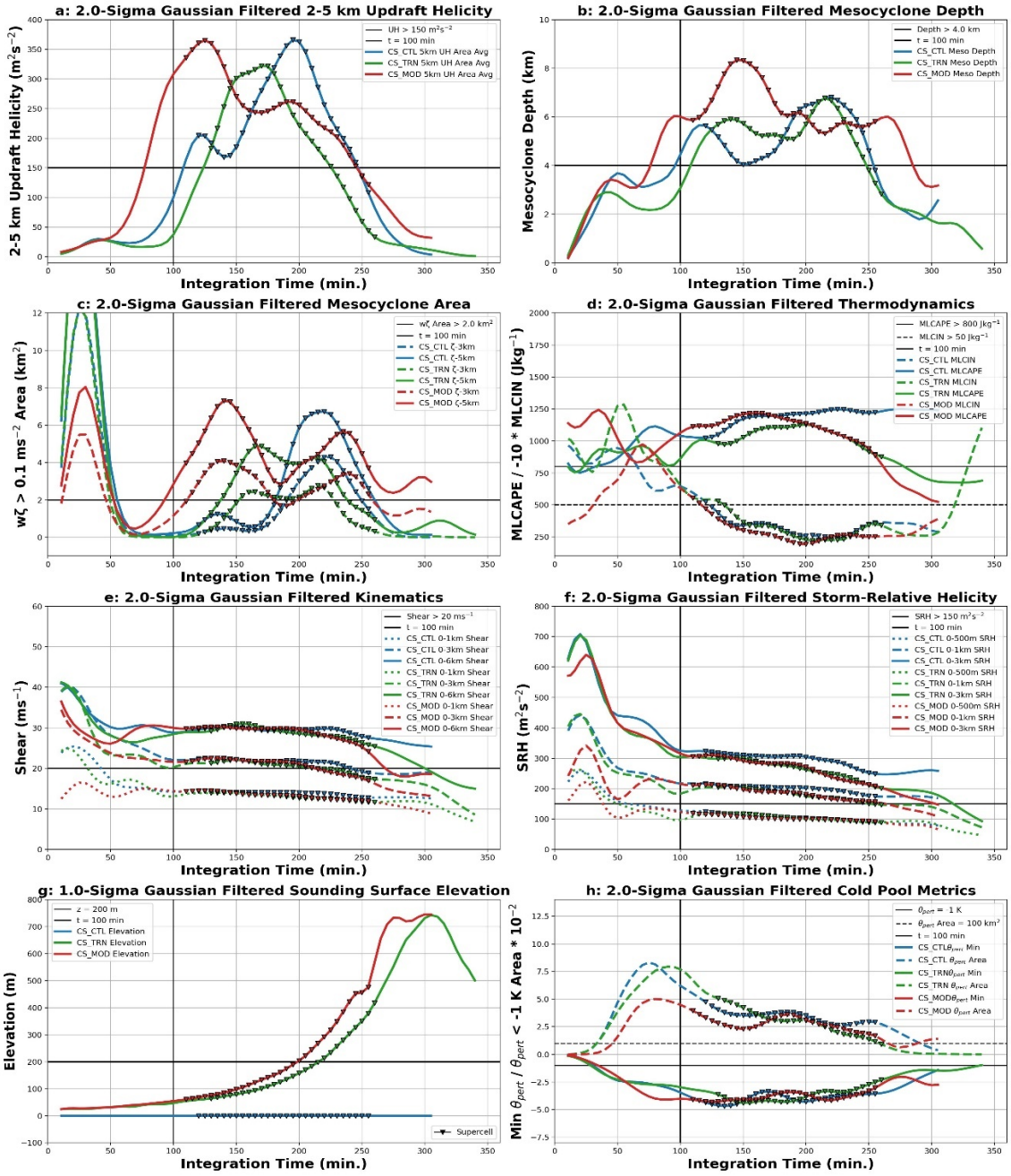

Figure 4.2: Gaussian filtered time-series for the three steady-state crossing simulations of various parameters pulled during storm tracking. a) included both maximum and 5.0 km areal averaged Updraft Helicity; b) Mesocyclone depth at the updraft helicity maxima; c) Mesocyclone area for 500 m, 1 km, and 5 km computed from a 35x35 km^2 box centered on the updraft helicity maxima; d) MLCAPE, MLCIN, and 3CAPE; e) 0-1 km, 0-3 km, and 0-6 km vertical shear; f) 0-500 m 0-1 km, and 0-3 km storm relative helicity, all computed from the near-storm inflow soundings; and g) the surface elevation of the near inflow sounding; and h) near-storm cold surface cold pool area and intensity; all for at any given time before dissipation with supercellular mode being demarcated by the upside down triangles.

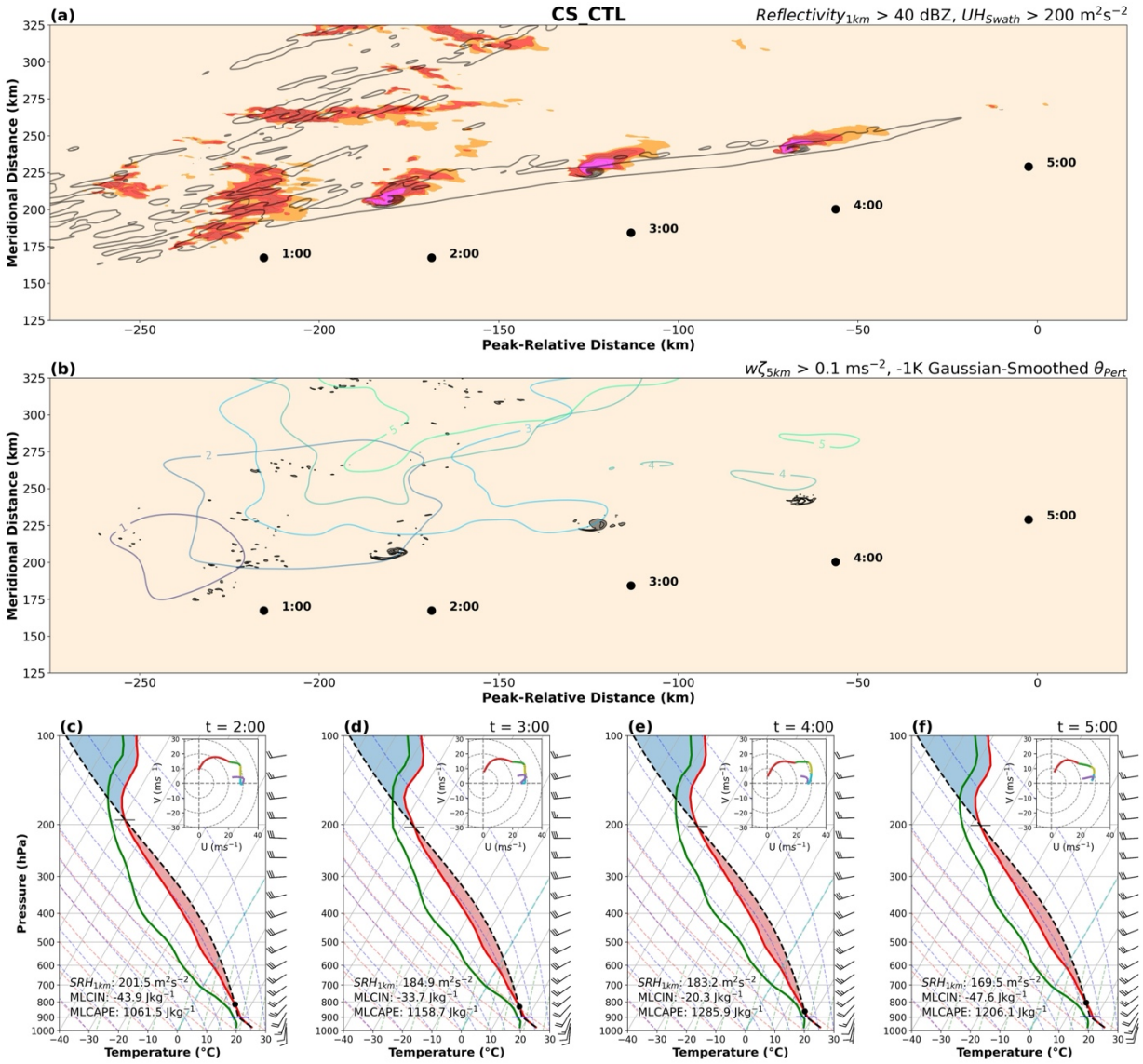

Figure 4.3: a) 2D hourly time-series depicting the radar reflectivity and updraft helicity swath of the CS_CTL simulation; b) 2D hourly time-series depicting the cold pool (-1 K potential temperature perturbation contour) and rotating updraft ($w\xi$ > 0.1 ms^{-2}); and c) near-storm inflow soundings for integration hours t = 2:00-5:00 that correspond to the spatial locations annotated by the labeled points in panels a & b with LCL denoted by the black line and LFC denoted by the black dot on each individual sounding.

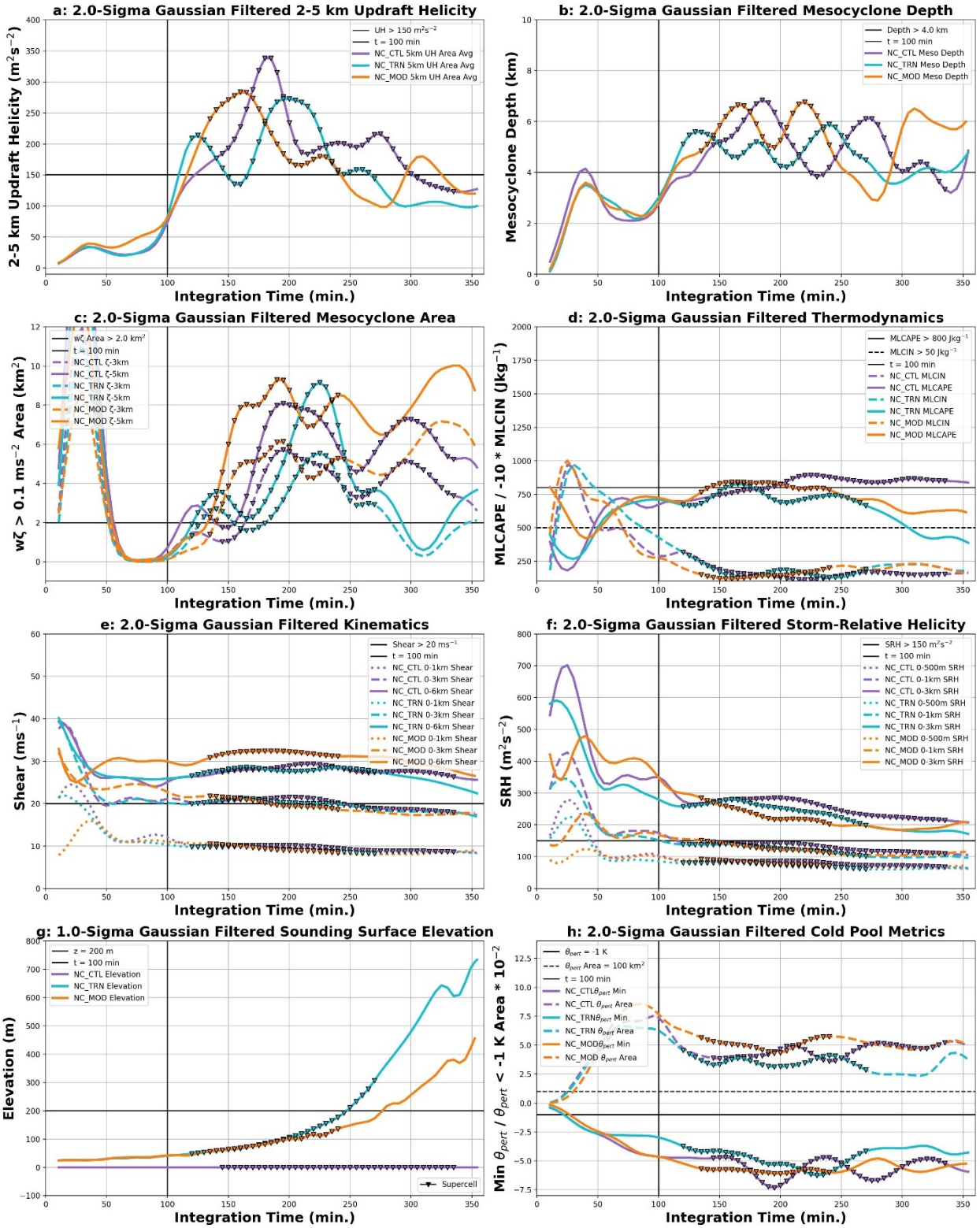

Figure 4.4: Same as in Figure 4.2 but for the steady-state non-crossing simulations.

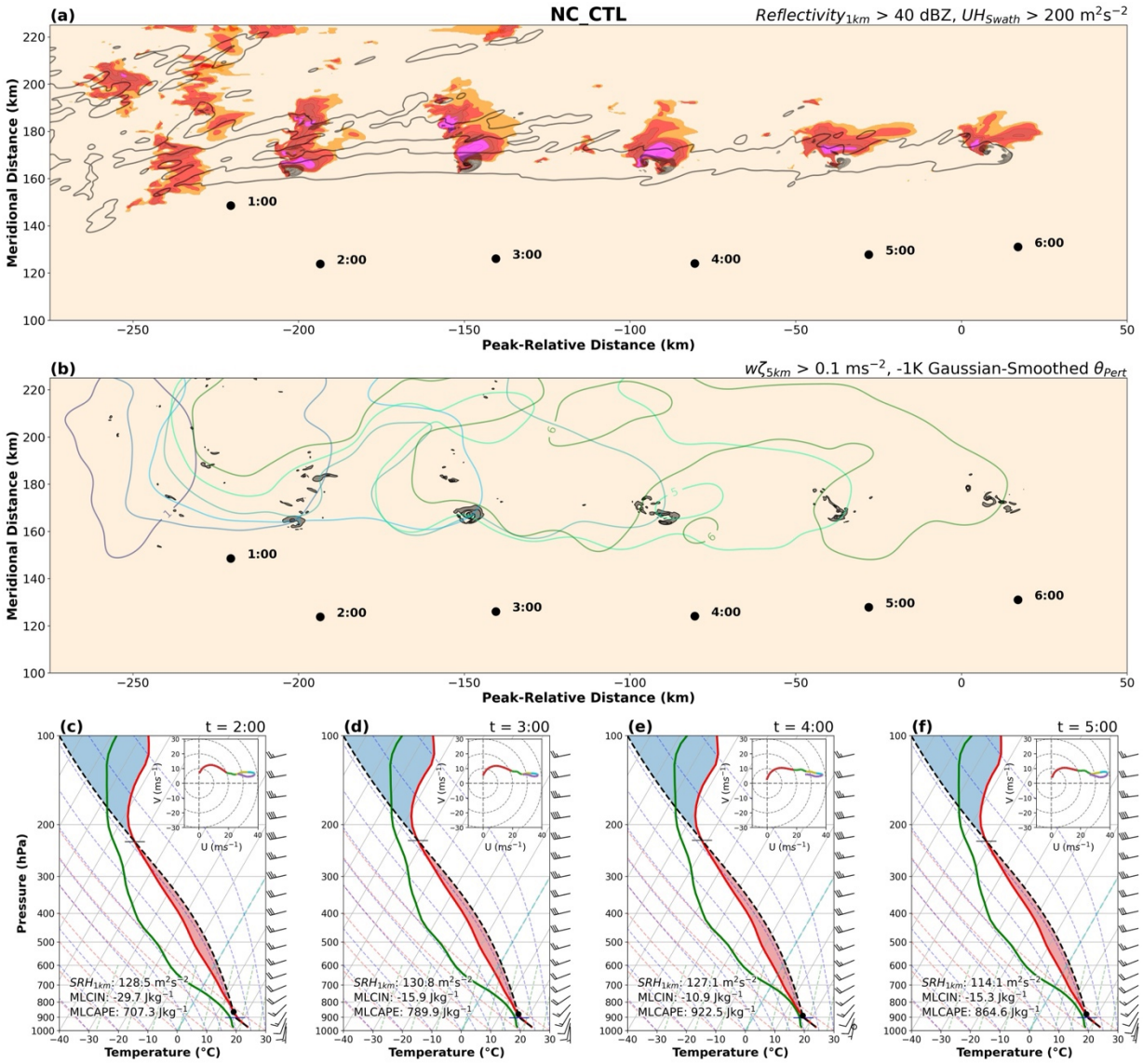

Figure 4.5: Same as in Figure 4.3 but for the NC_CTL simulation

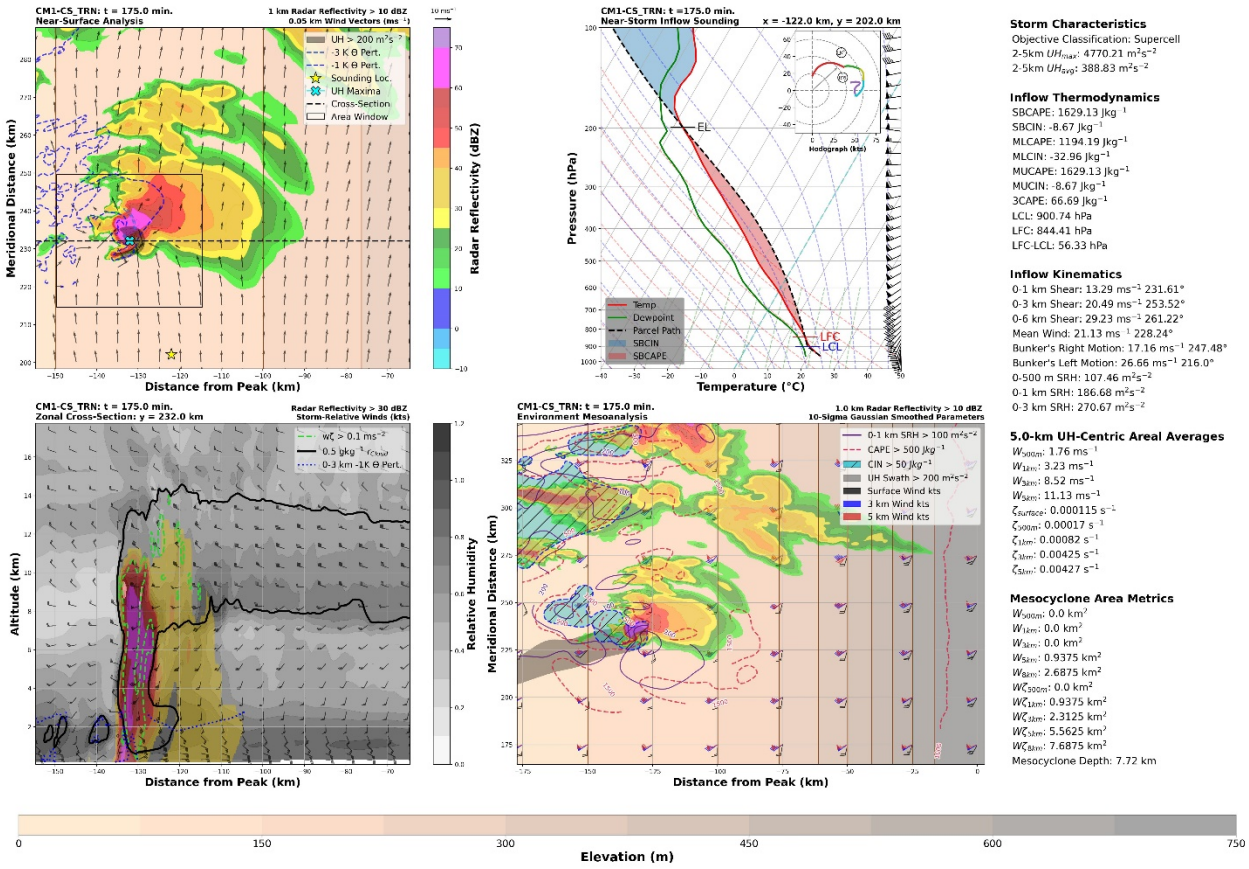

Figure 4.6: CS_TRN 4-Panel Plot including the Near-Surface Analysis (Upper-Left); Near-Storm Inflow Sounding (Upper-Right); Zonal Cross-Section through the local UH maxima (Bottom-Left); Environmental Mesoanalysis (Lower-Right); and Various inflow sounding parameters and mesocyclone metrics computed during the 5-minute analysis for t= 175 minutes when CS_TRN was at peak intensity.

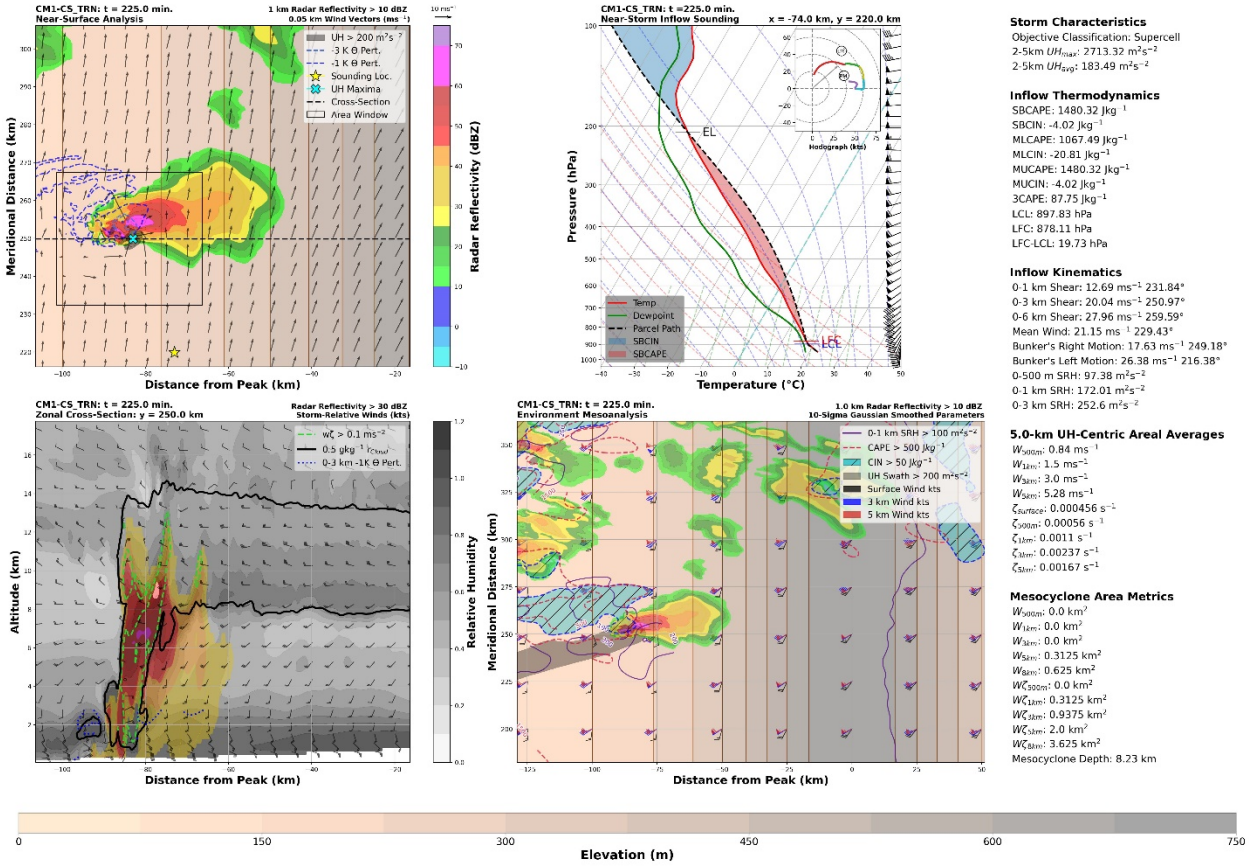

Figure 4.7: Same as Figure 4.6 but for CS_TRN at t = 225 min.

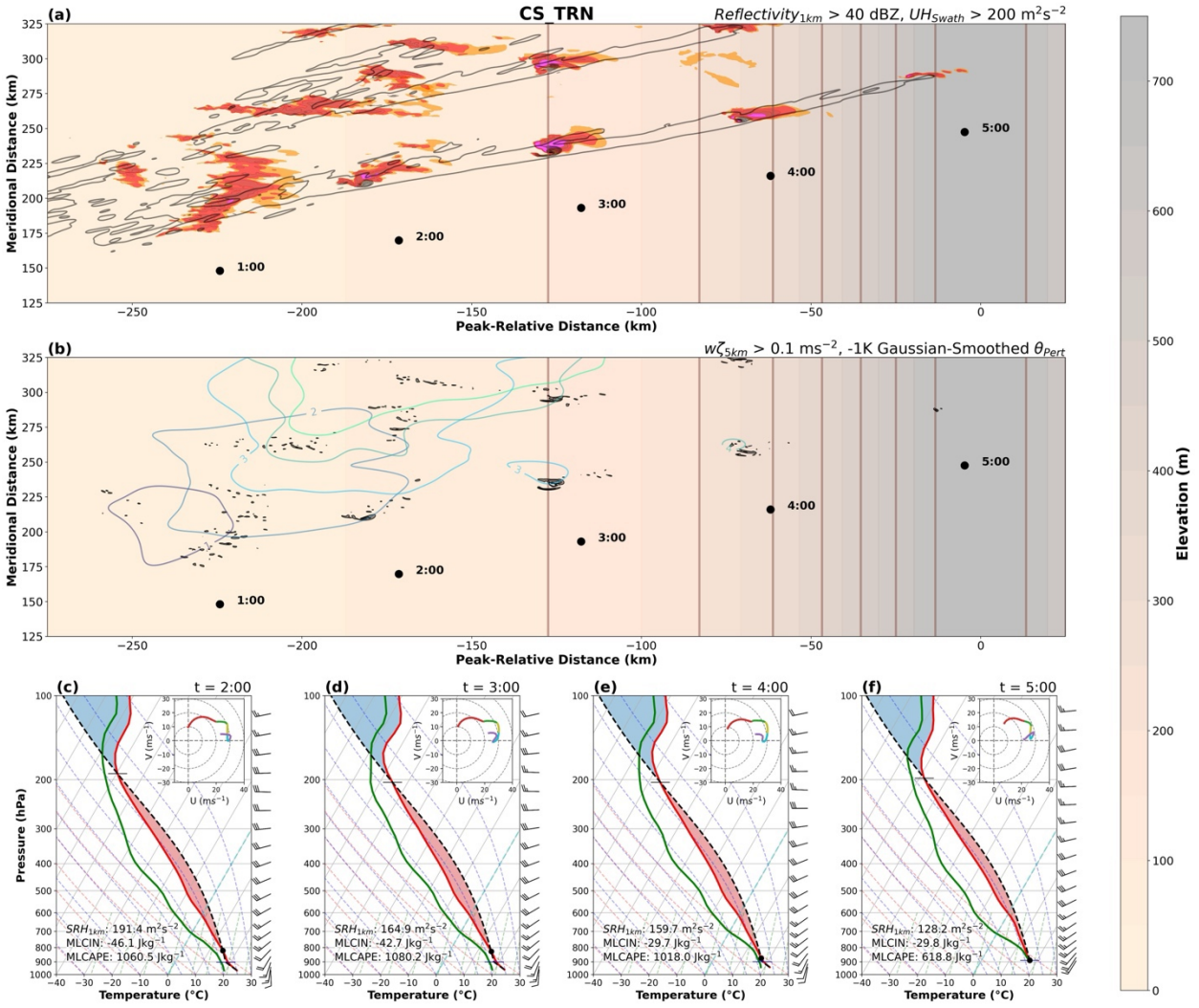

Figure 4.8: Same as in Figure 4.3 but for CS_TRN.

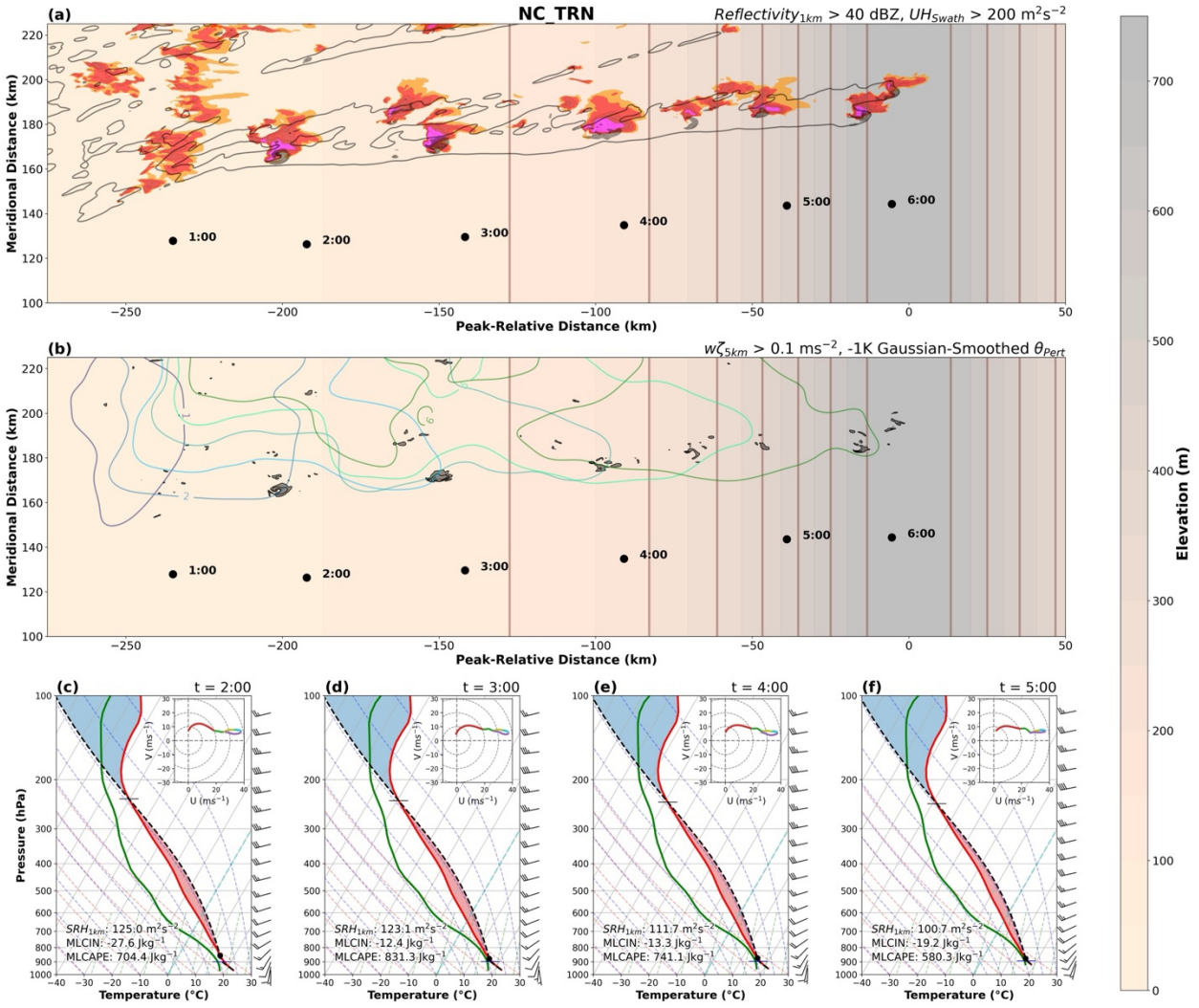

Figure 4.9: Same as in Figure 4.3 but for NC_TRN.

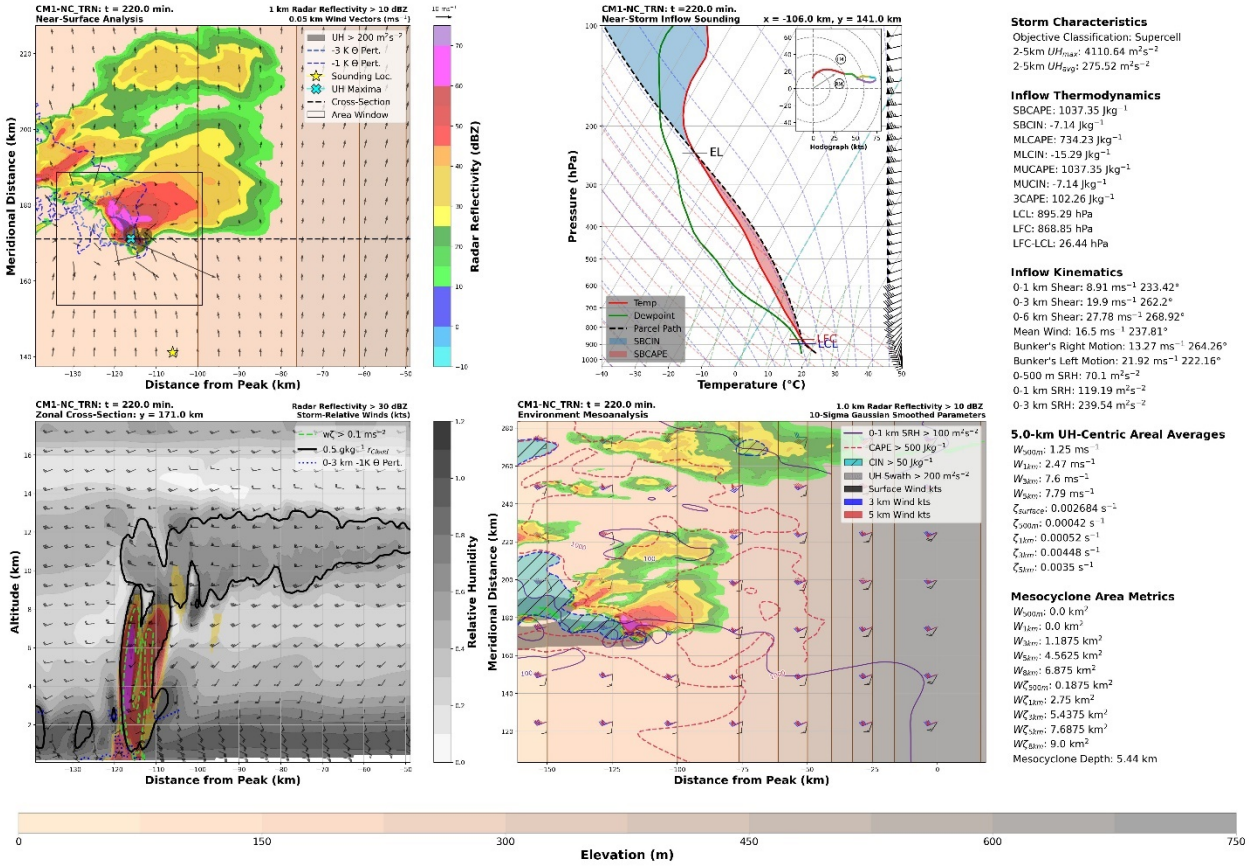

Figure 4.10: Same as in Figure 4.6 but for NC_TRN at t= 220 min.

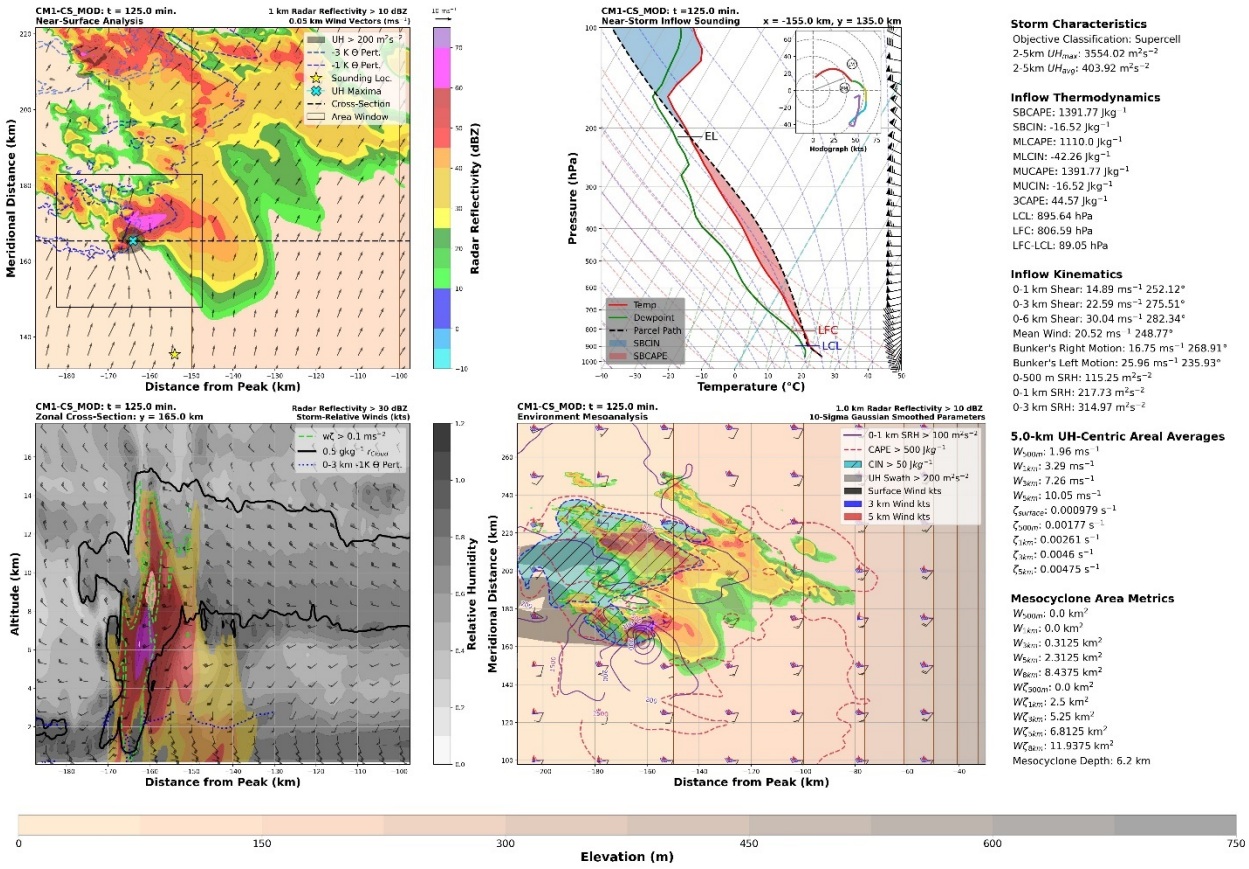

Figure 4.11: Same as in Figure 4.6 but for CS_MOD at t= 125 min when the storm is at peak intensity.

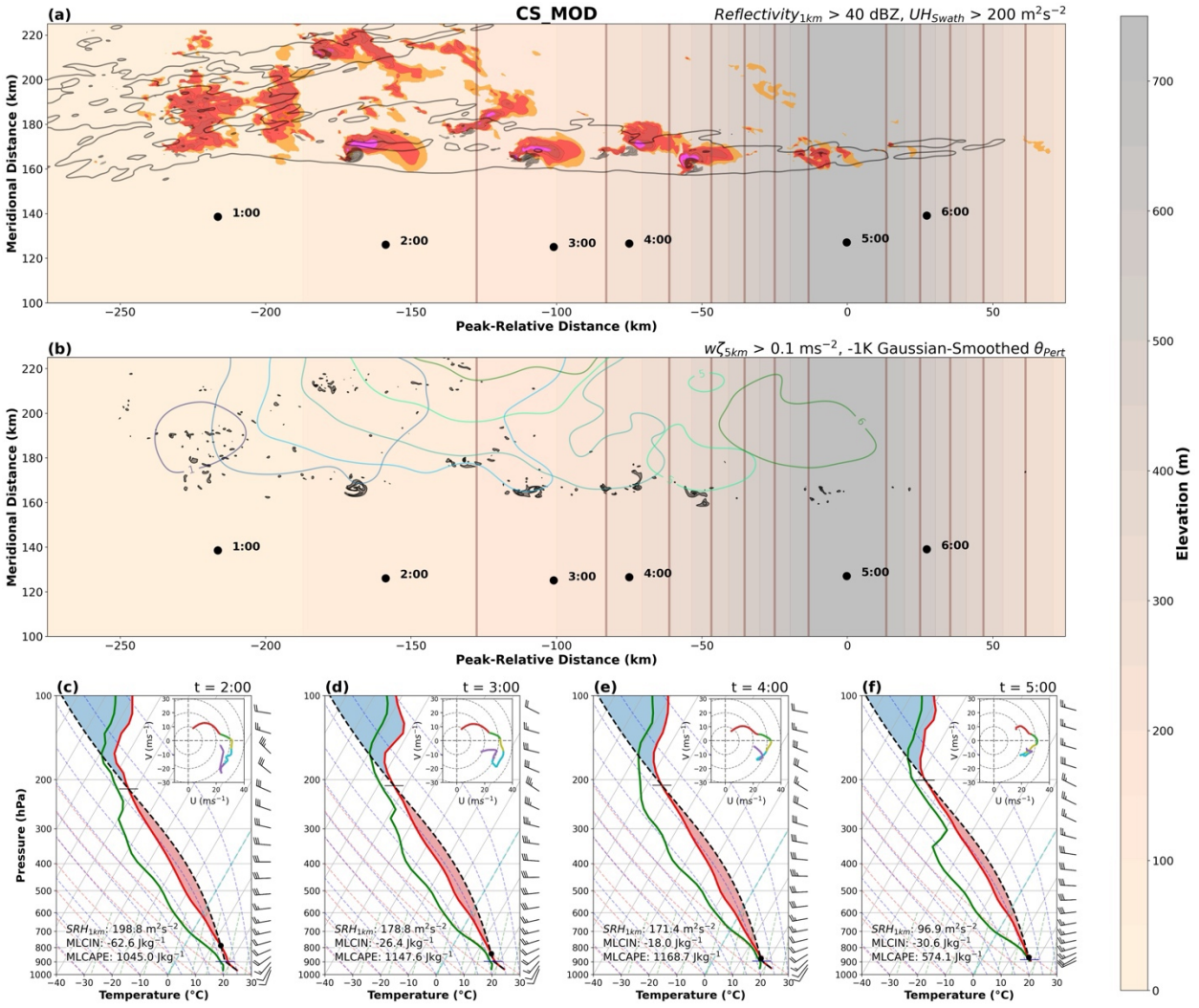

Figure 4.12: Same as in Figure 4.3 but for CS_MOD.

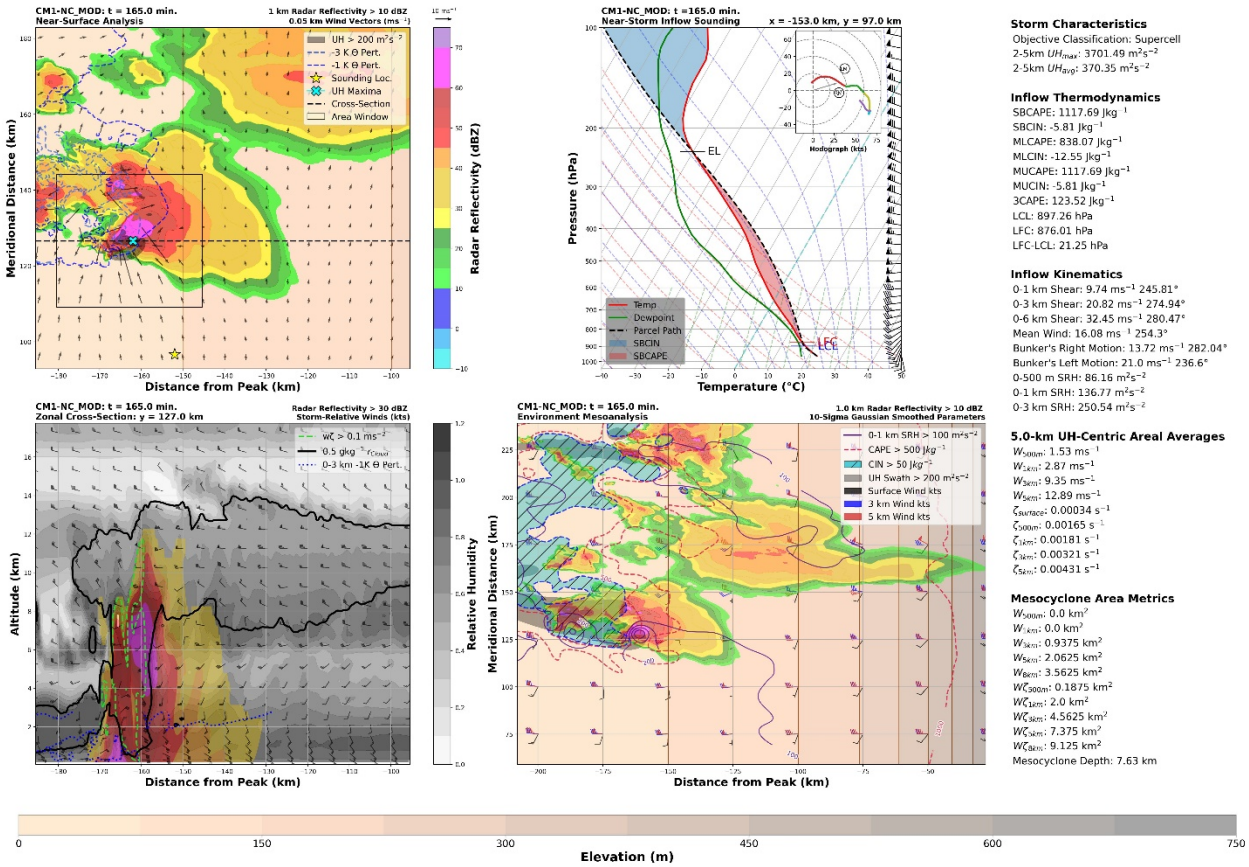

Figure 4.13: Same as in Figure 4.6 but for NC_MOD at t= 165 min. when the storm was at peak intensity.

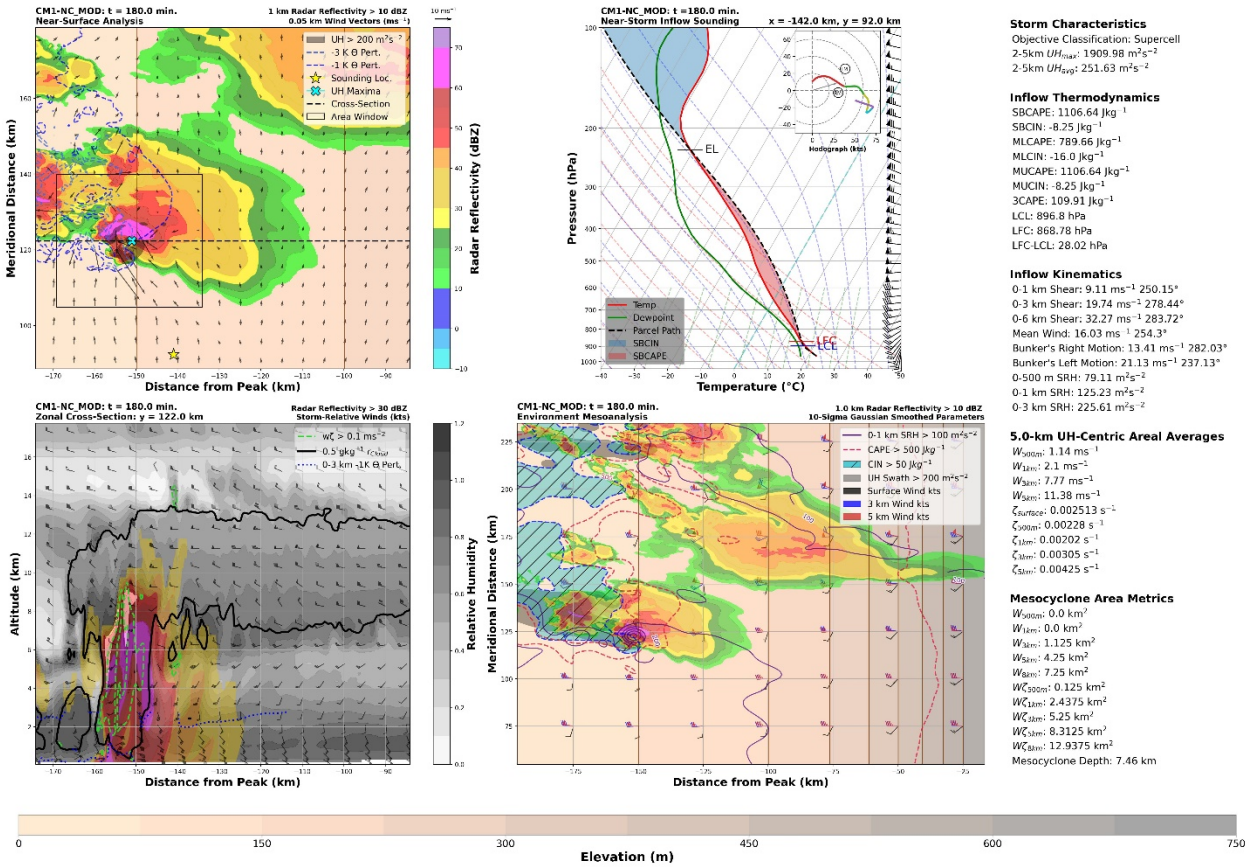

Figure 4.14: Same as in Figure 4.6 but for NC_MOD at t= 180 min.

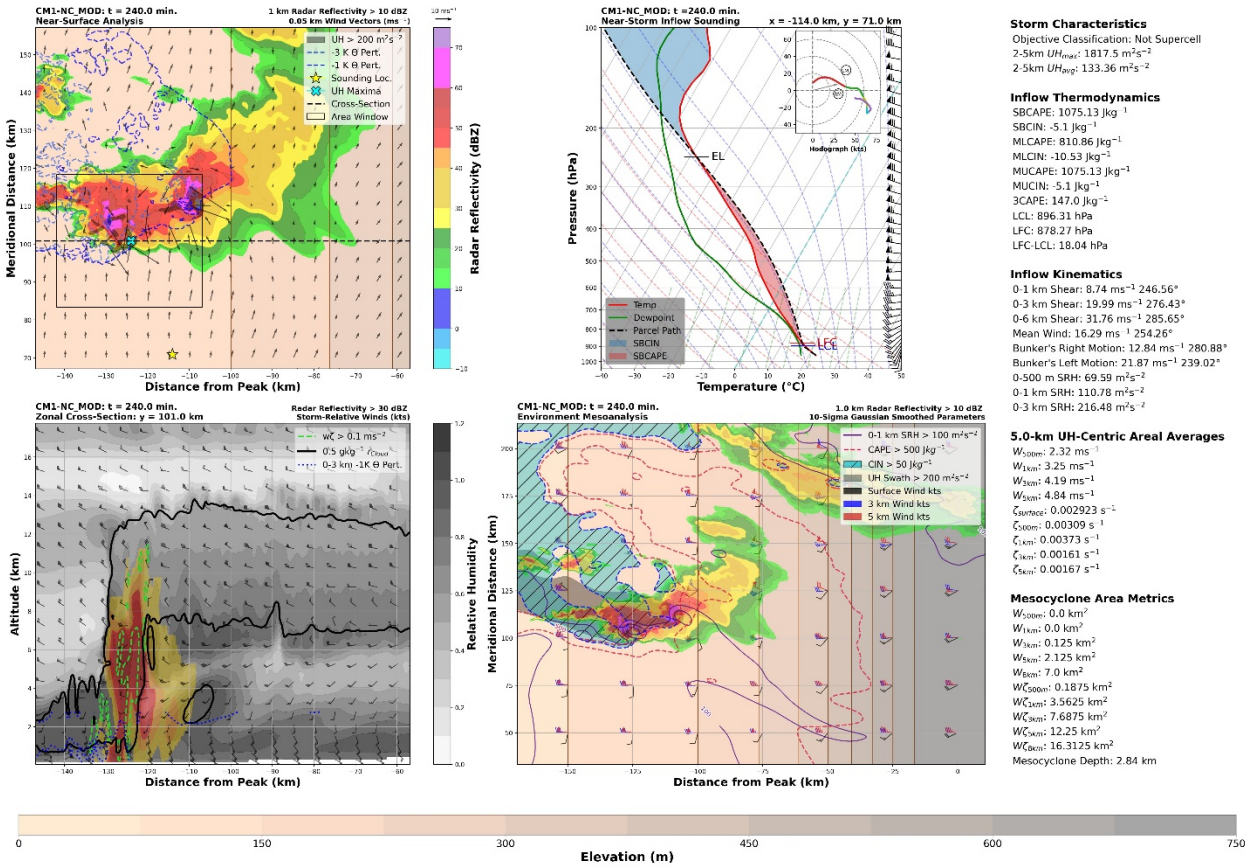

Figure 4.15: Same as in Figure 4.6 but for NC_MOD at t= 240 min. when the storm has completed linear transition on the windward slope of the terrain.

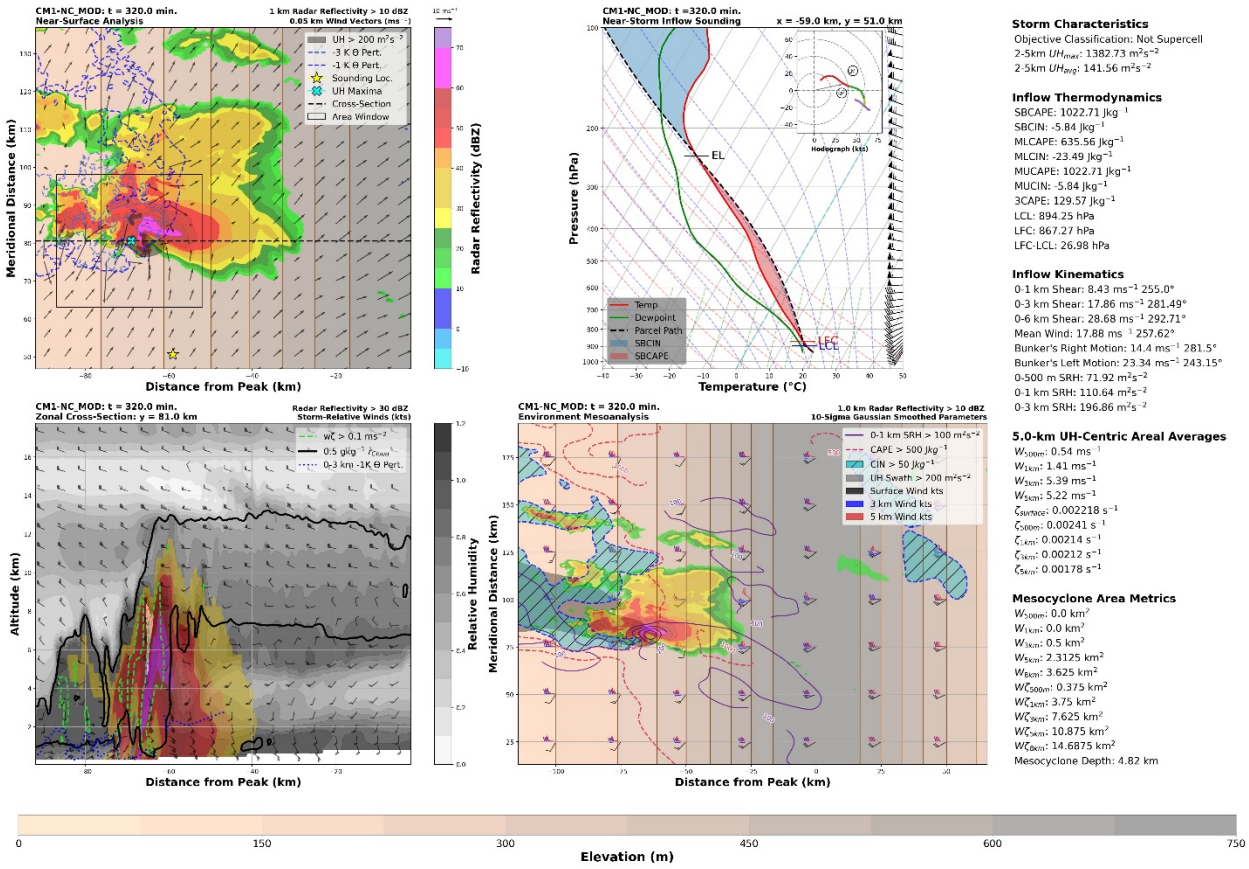

Figure 4.16: Same as in Figure 4.6 but for NC_MOD at t= 320 min

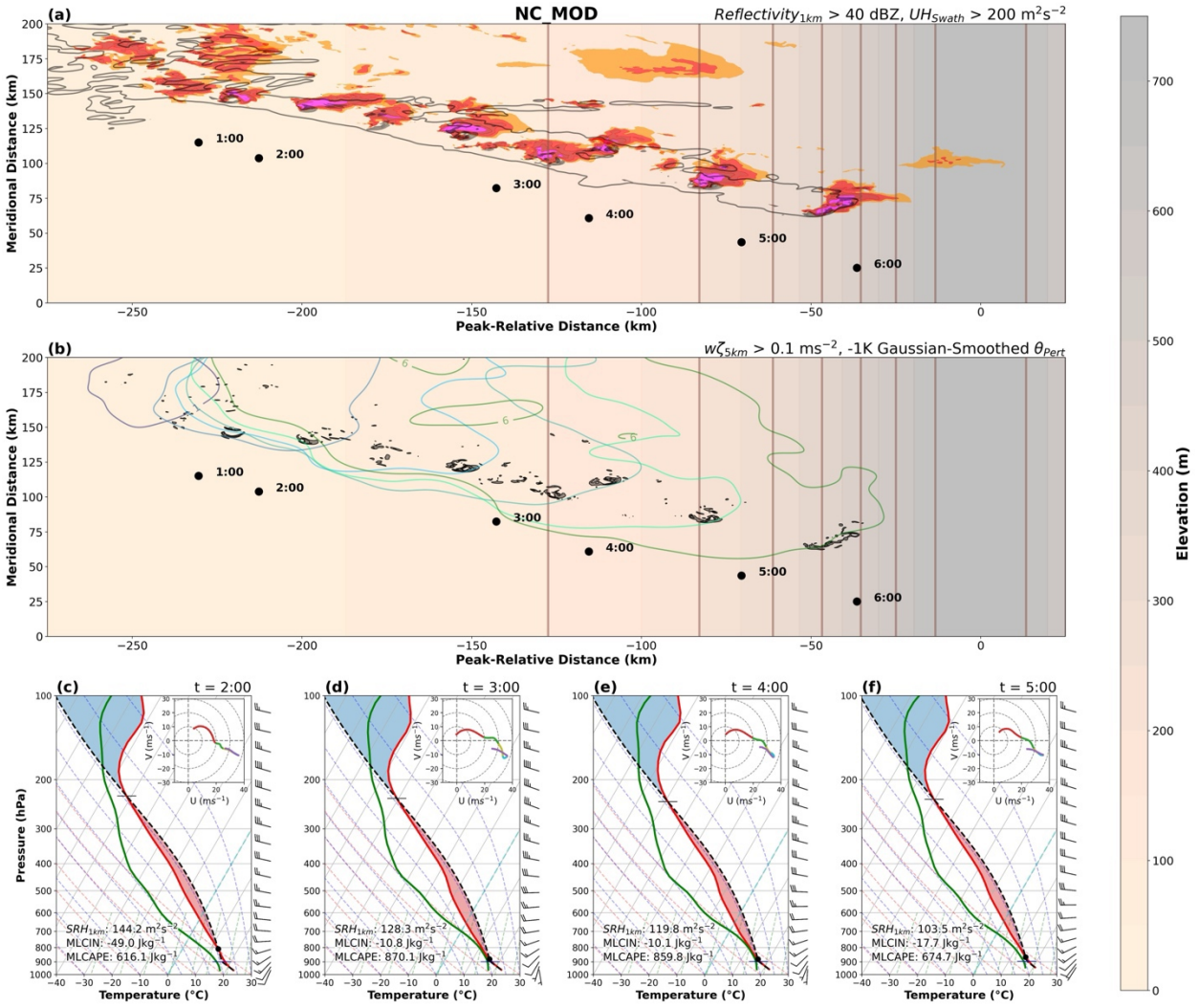

Figure 4.17: Same as in Figure 4.3 but for NC_MOD.

Simulation	Updraft Nudging X-Center Point	Updraft Nudging Y-Center Point
CS_RLTRN_ALL	100 km	175 km
CS_RLTRN_NO_OUT	125 km	250 km
CS_RLTRN_OUT	150 km	125 km
NC_RLTRN_ALL	150 km	250 km
NC_RLTRN_NO_OUT	75 km	250 km

Table 4.1: A table displaying the central coordinates of the artificial updraft nudging technique used for convective initiation during our realistic terrain simulations. In all five simulations the updraft nudging dimensions were the same (15 x 75 x 0.75 km^3).

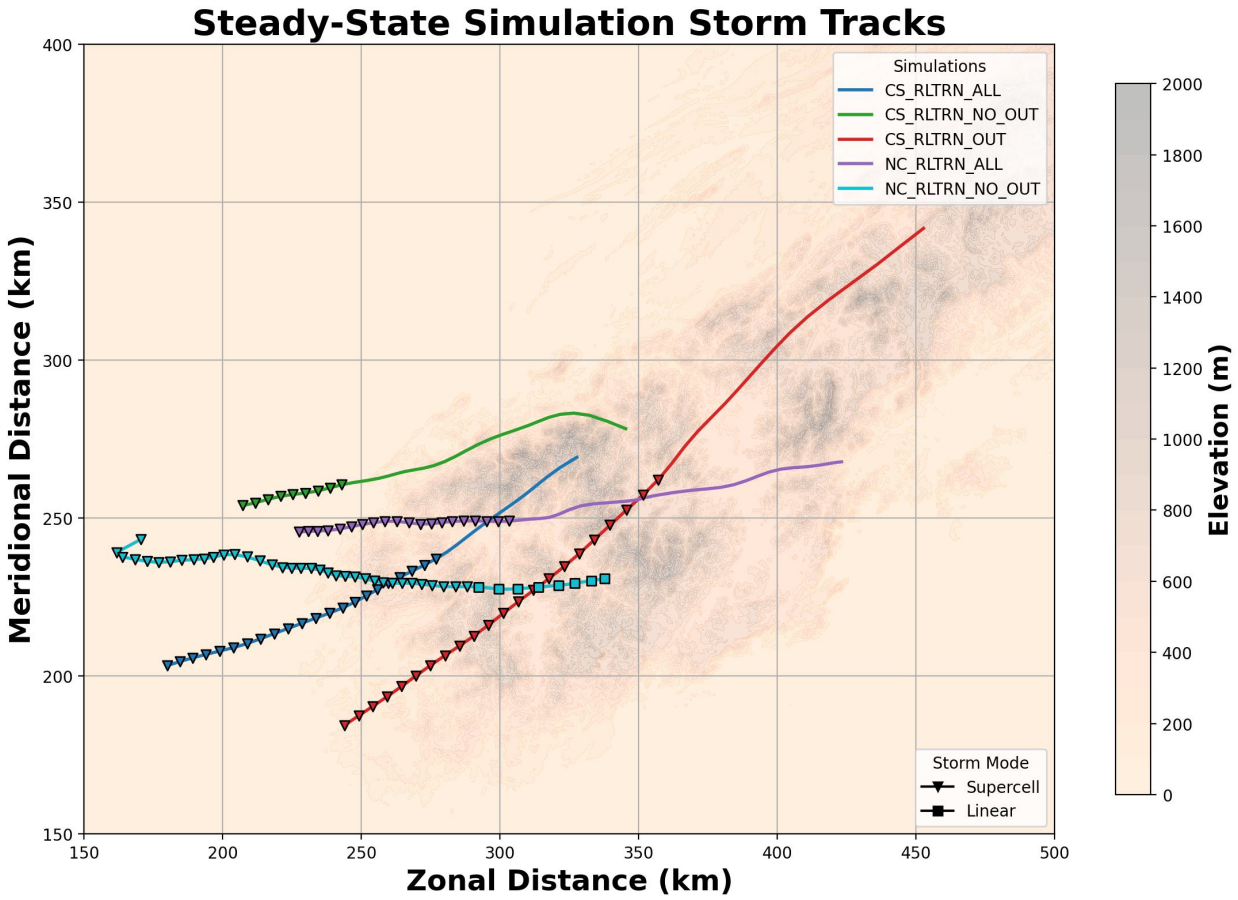

Figure 4.18: Same as in Figure 4.1 but for the five Realistic Terrain simulations.

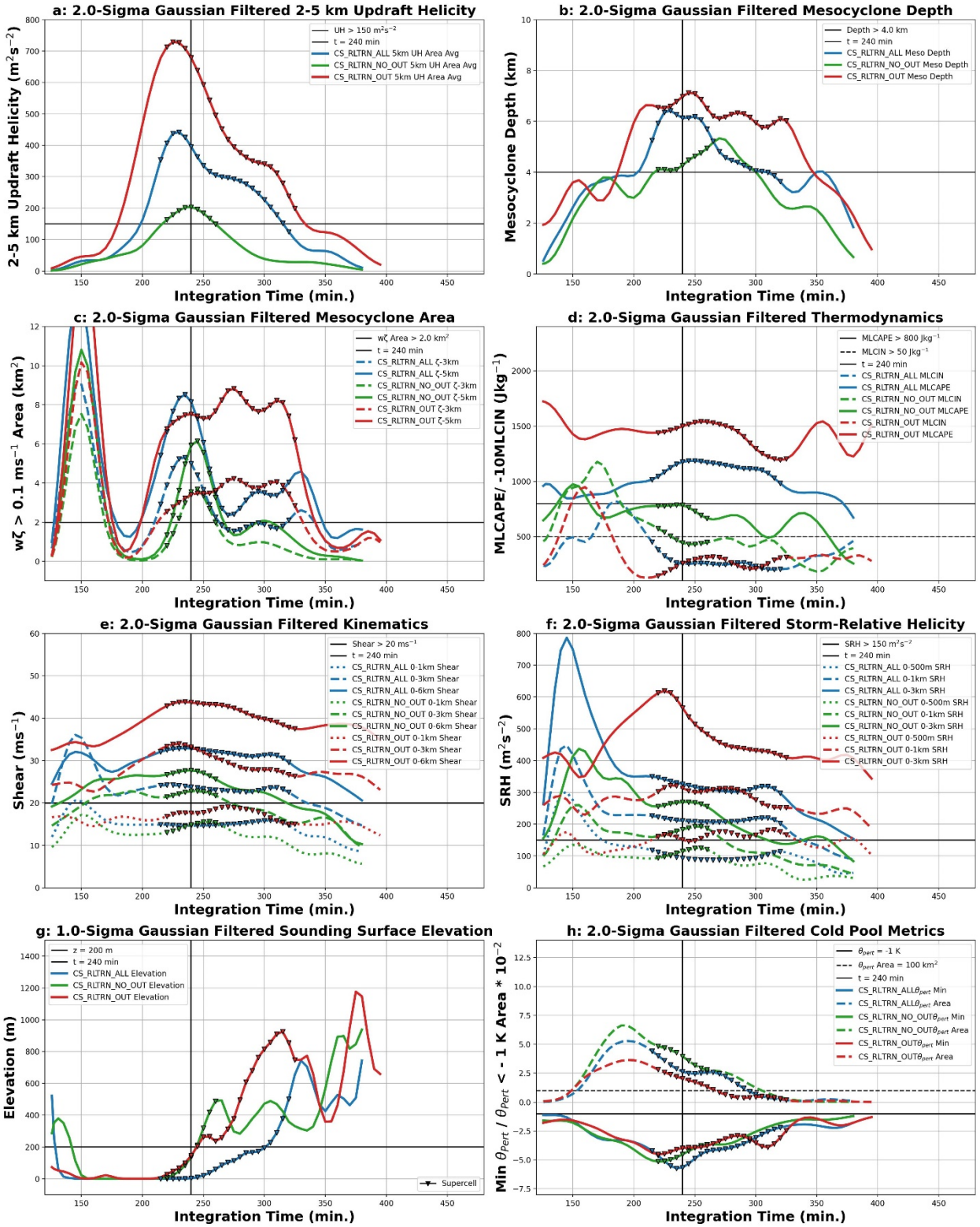

Figure 4.19: Same as in Figure 4.2 but for the steady-state crossing realistic terrain simulations.

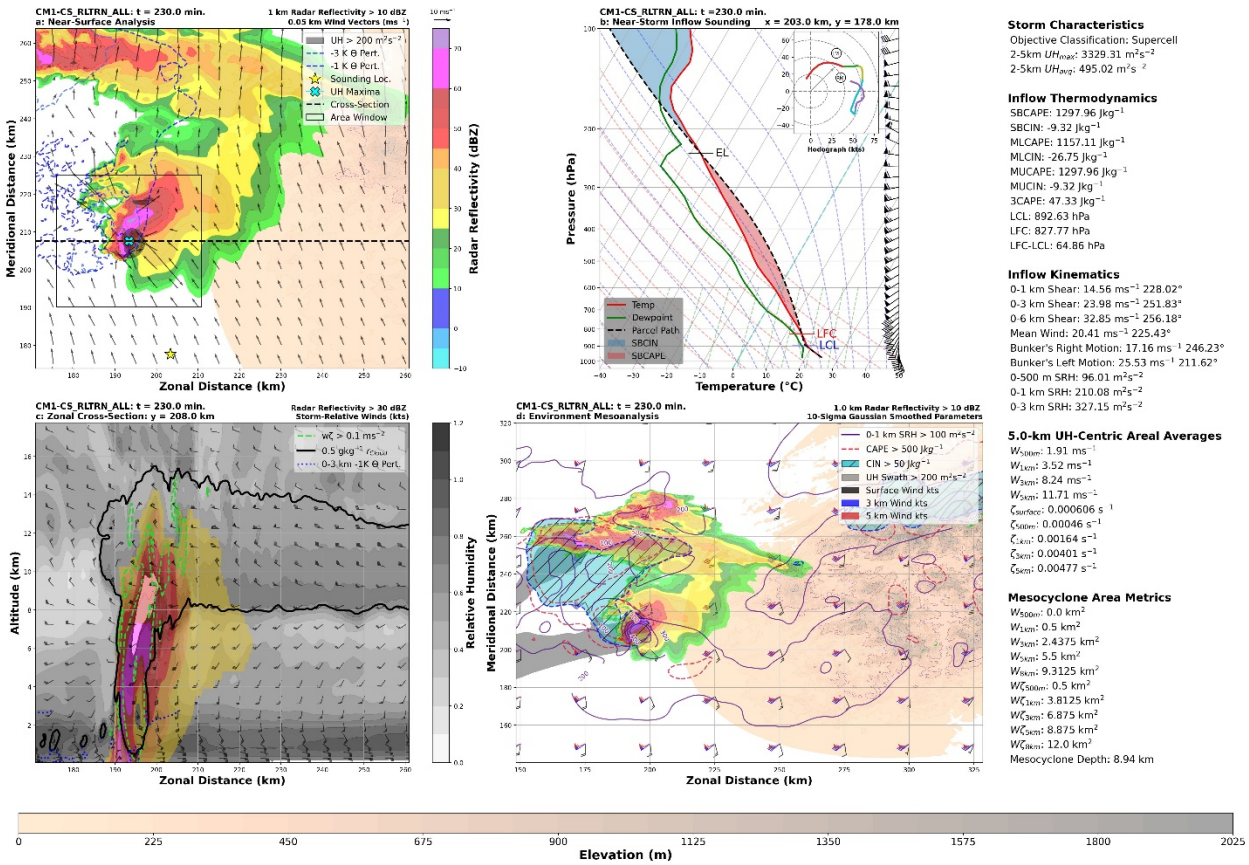

Figure 4.20: Same as in Figure 4.6 but for CS_RLTRN_ALL at t= 230 min. when the storm was at peak intensity.

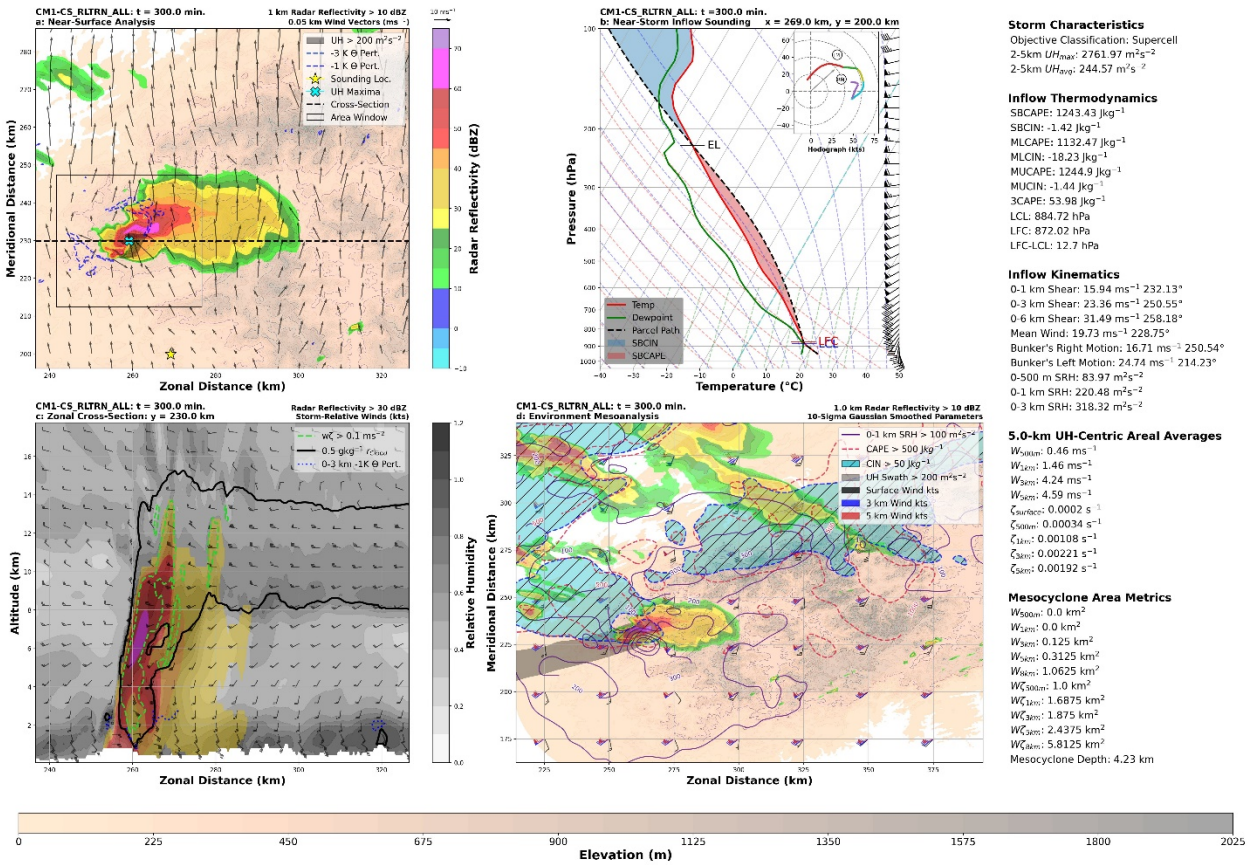

Figure 4.21: Same as in Figure 4.6 but for CS_RLTRN_ALL at t= 300 min.

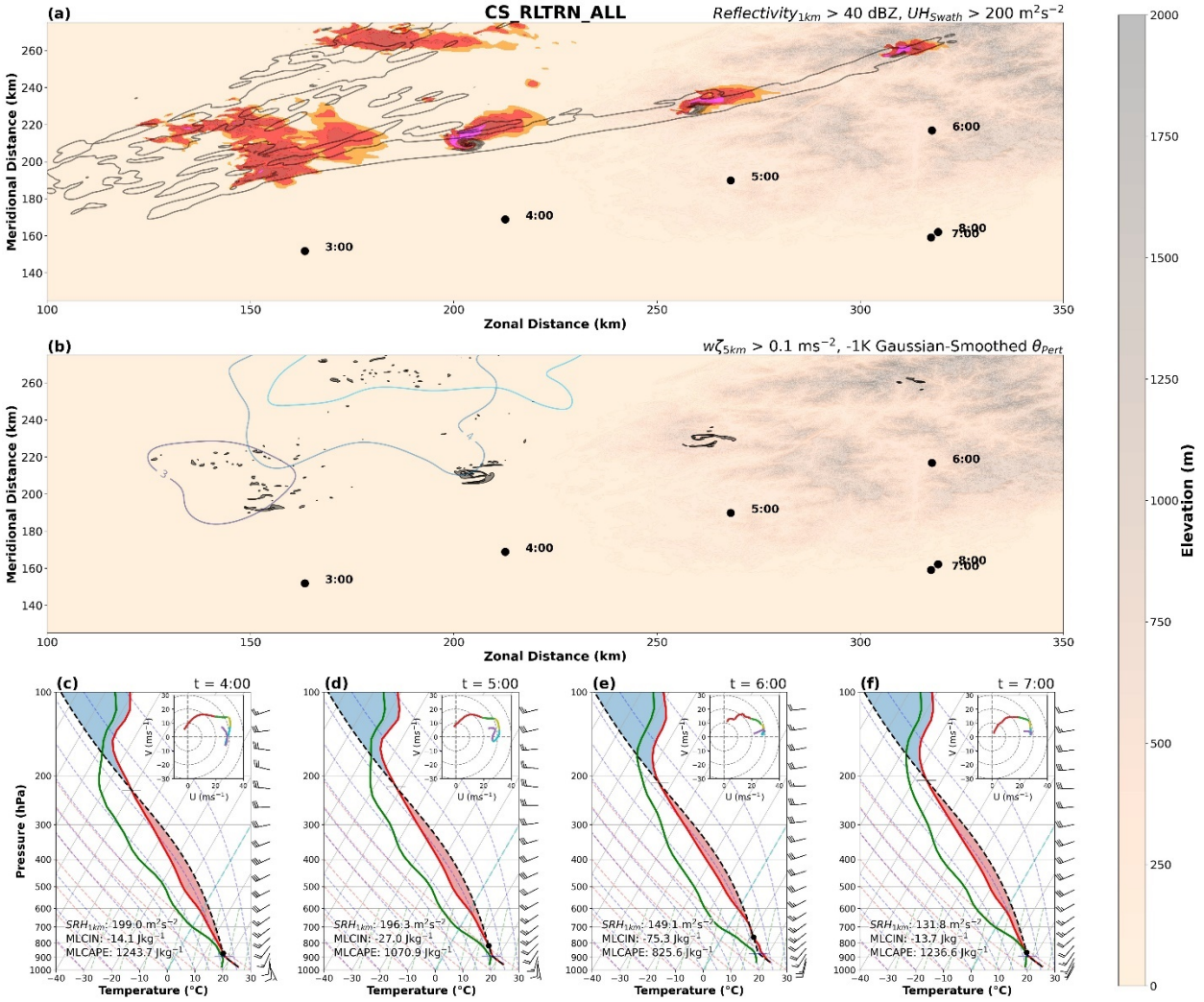

Figure 4.22: Same as in Figure 4.3 but for CS_RLTRN_ALL

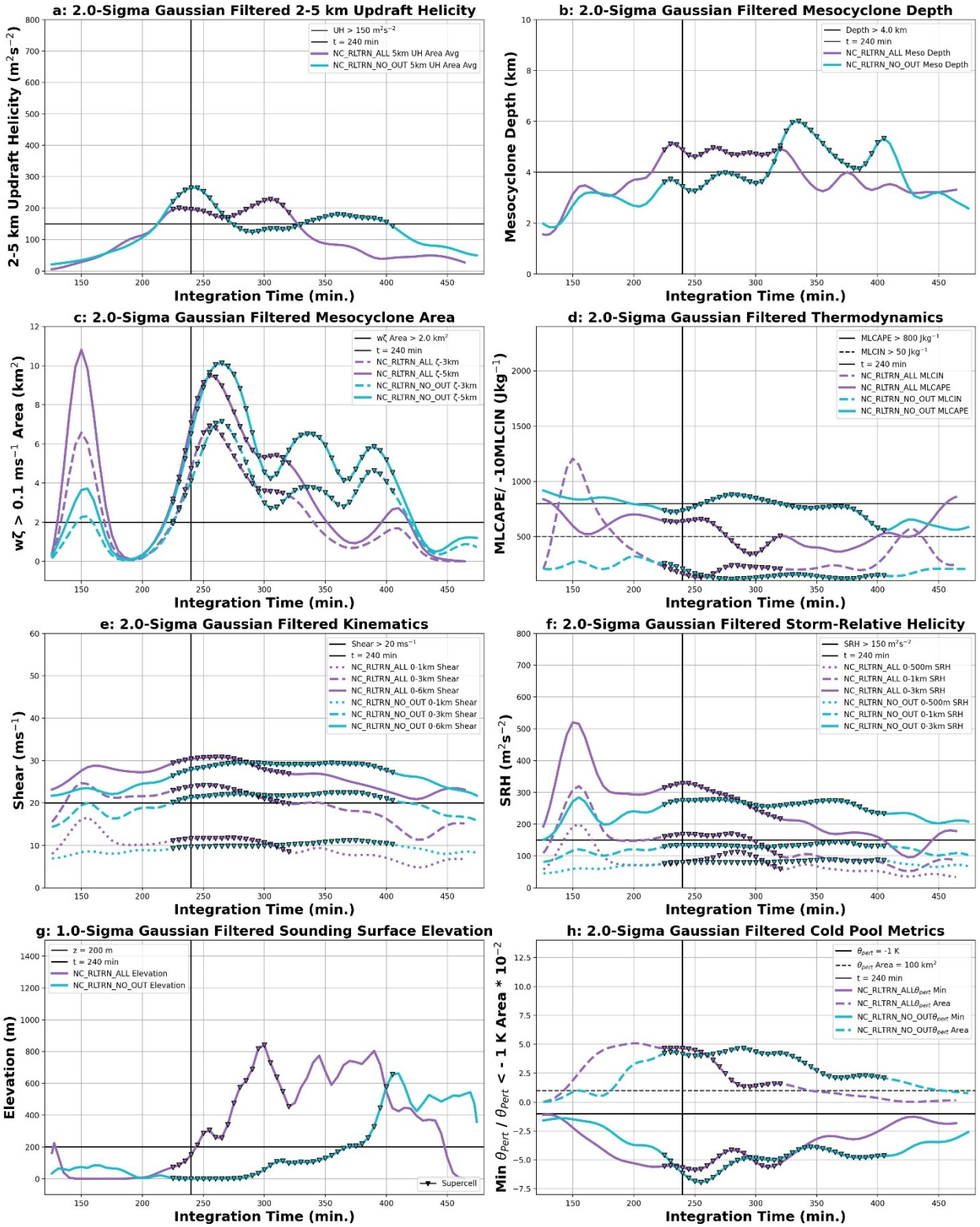

Figure 4.23: Same as in Figure 4.2 but for the steady-state non-crossing realistic terrain simulations.

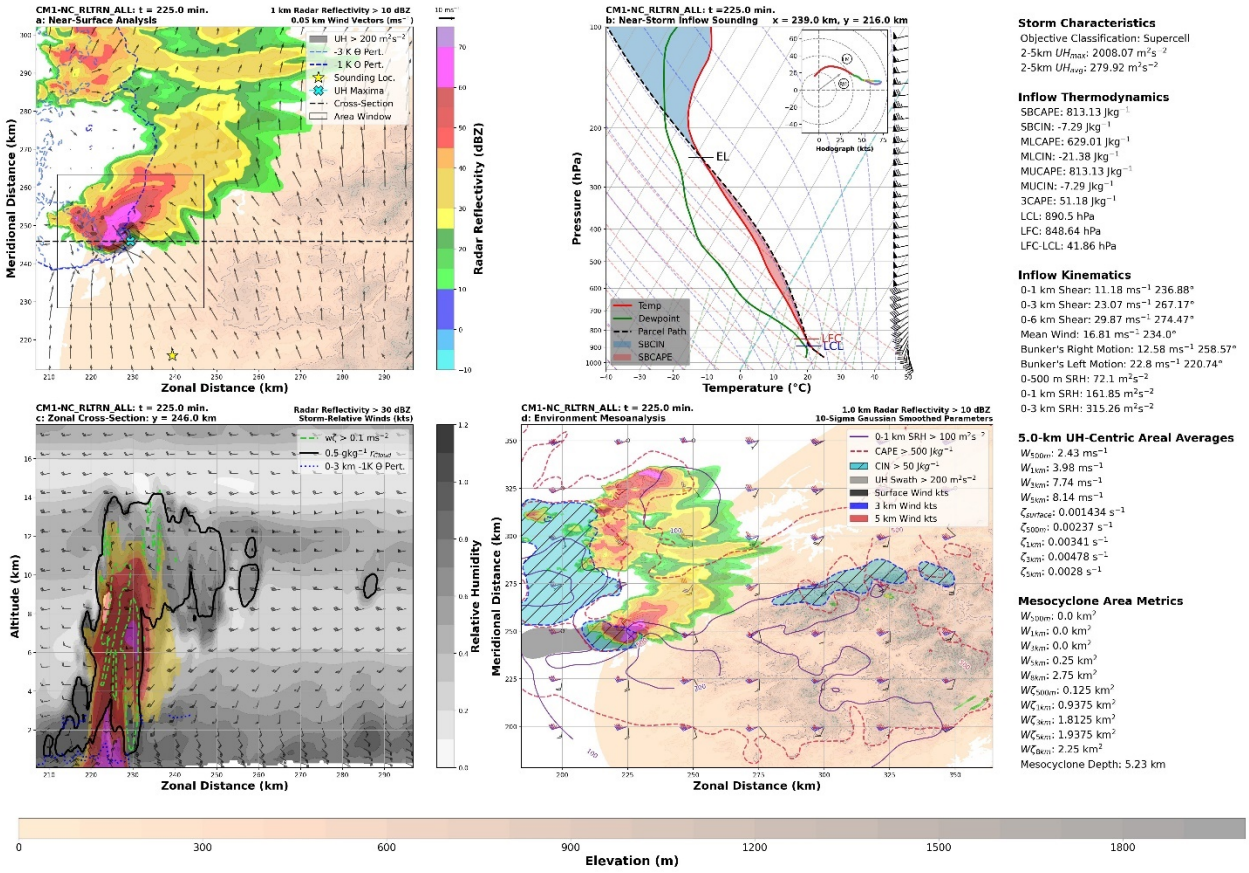

Figure 4.24: Same as in Figure 4.6 but for NC_RLTRN_ALL at t= 225 min.

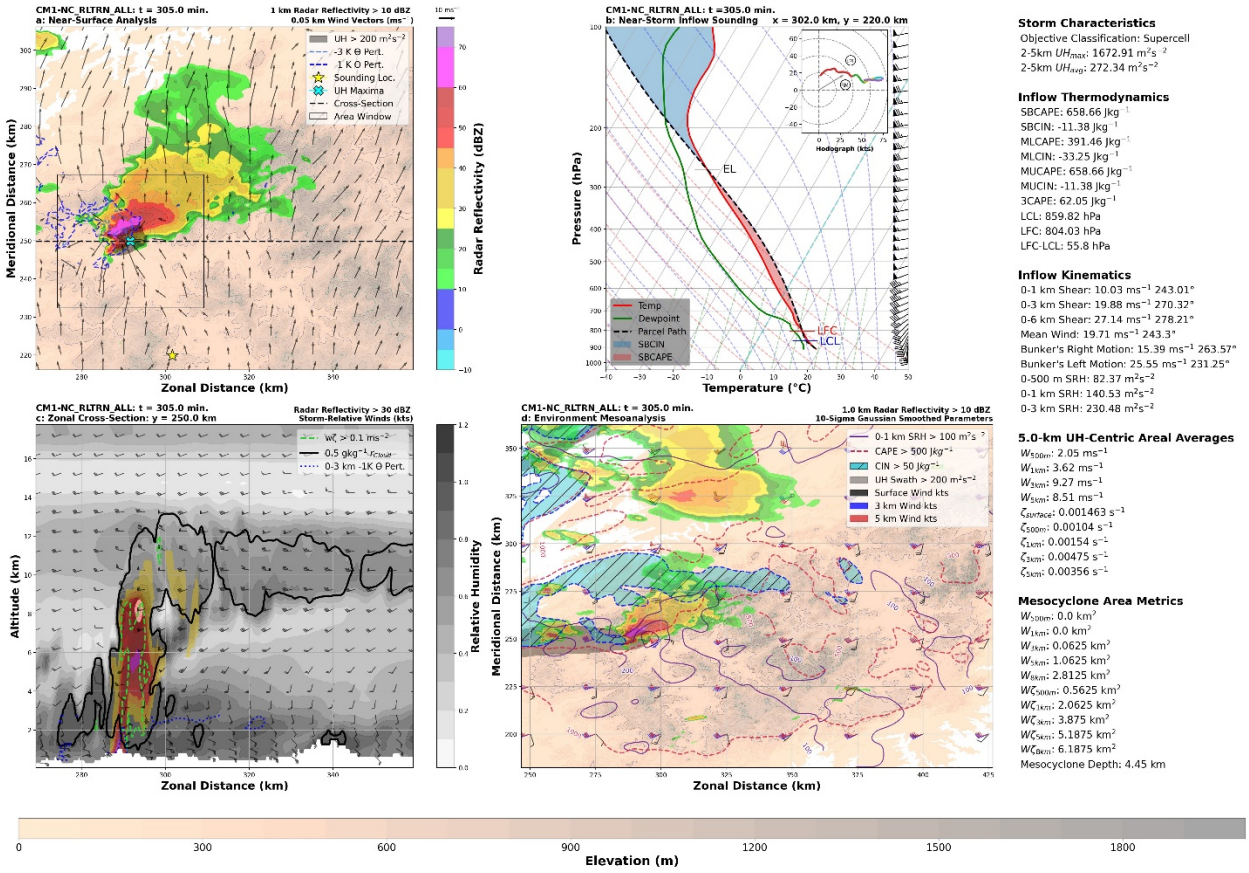

Figure 4.25: Same as in Figure 4.6 but for NC_RLTRN_ALL at t= 305 min when the storm was at peak intensity.

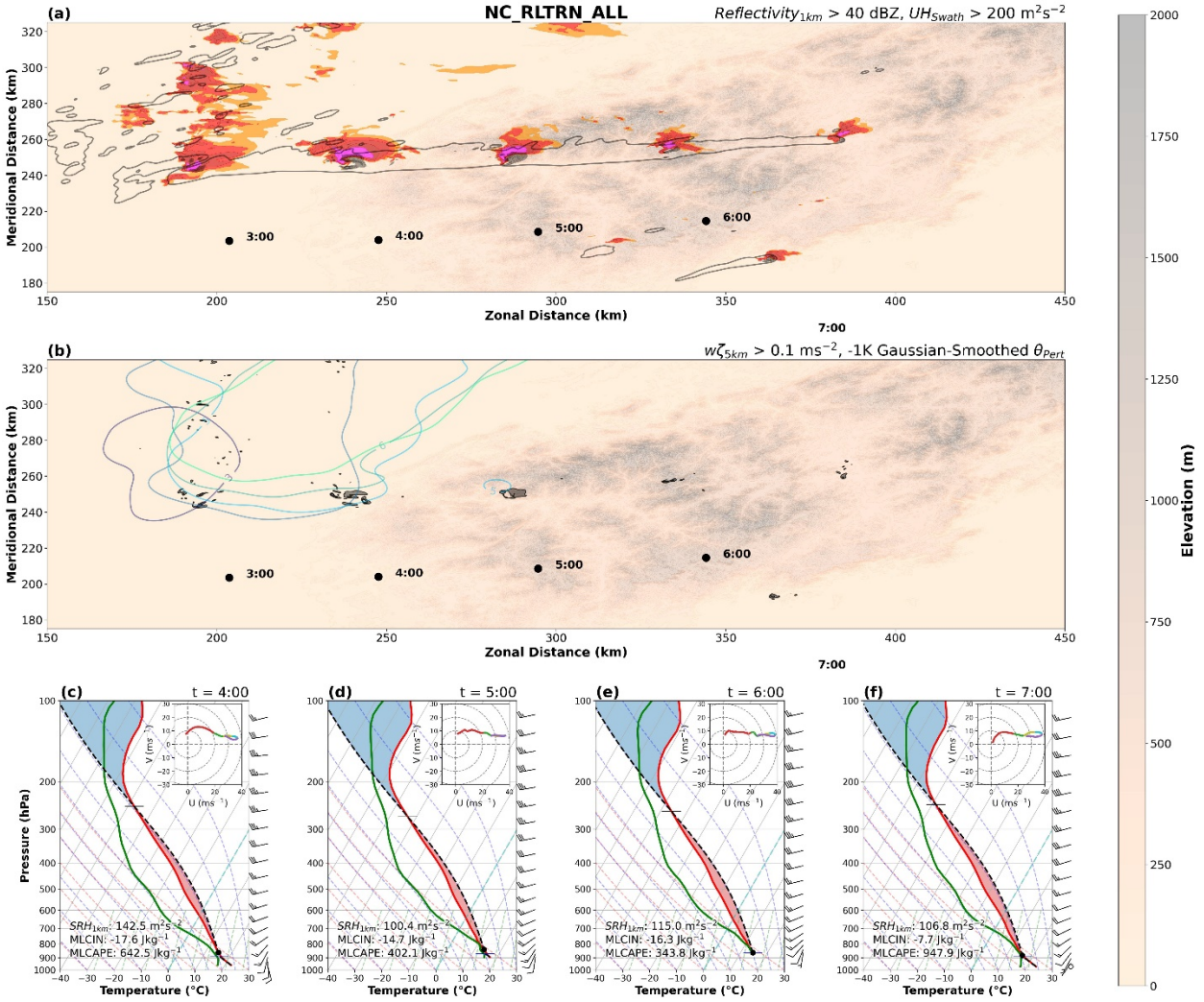

Figure 4.26: Same as in Figure 4.3 but for NC_RLTRN_ALL.

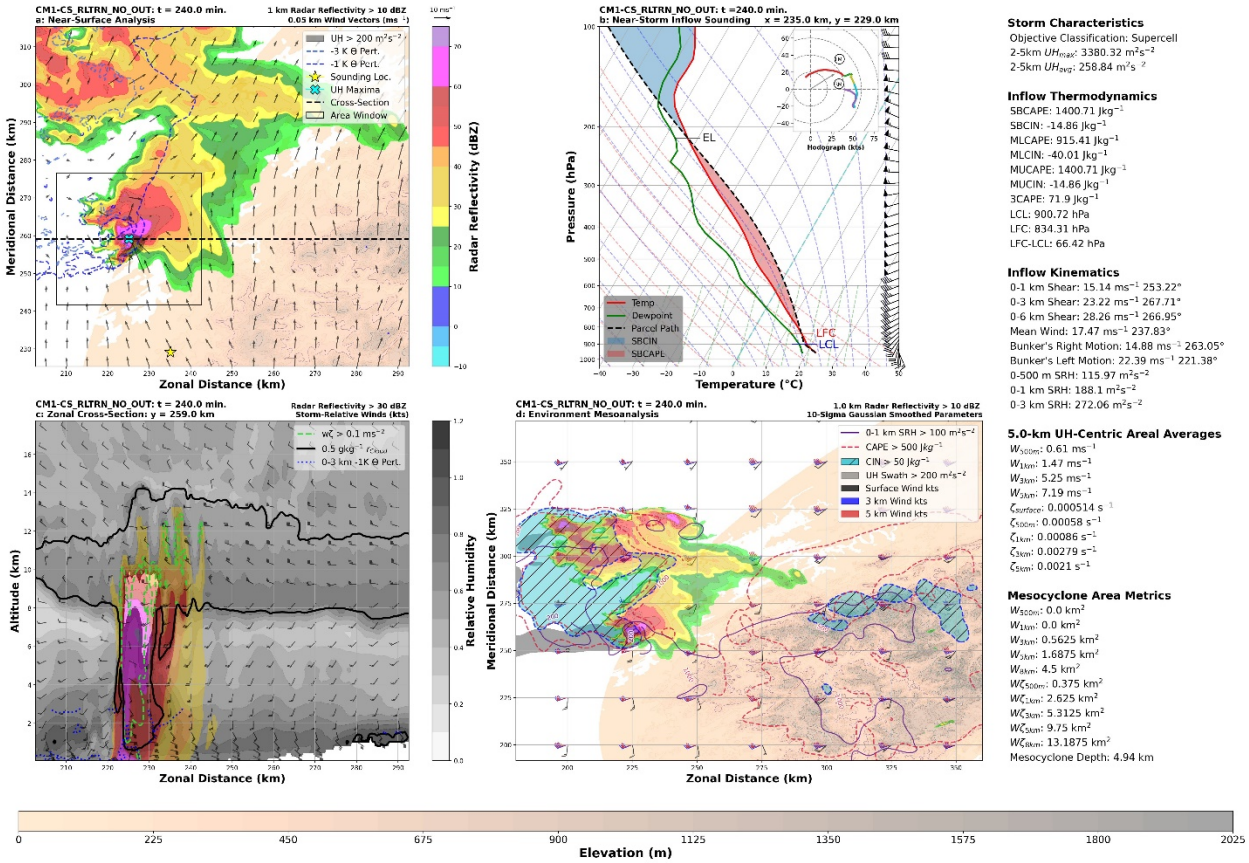

Figure 4.27: Same as in Figure 4.6 but for CS_RLTRN_NO_OUT at t= 240 min. when the storm was at peak intensity.

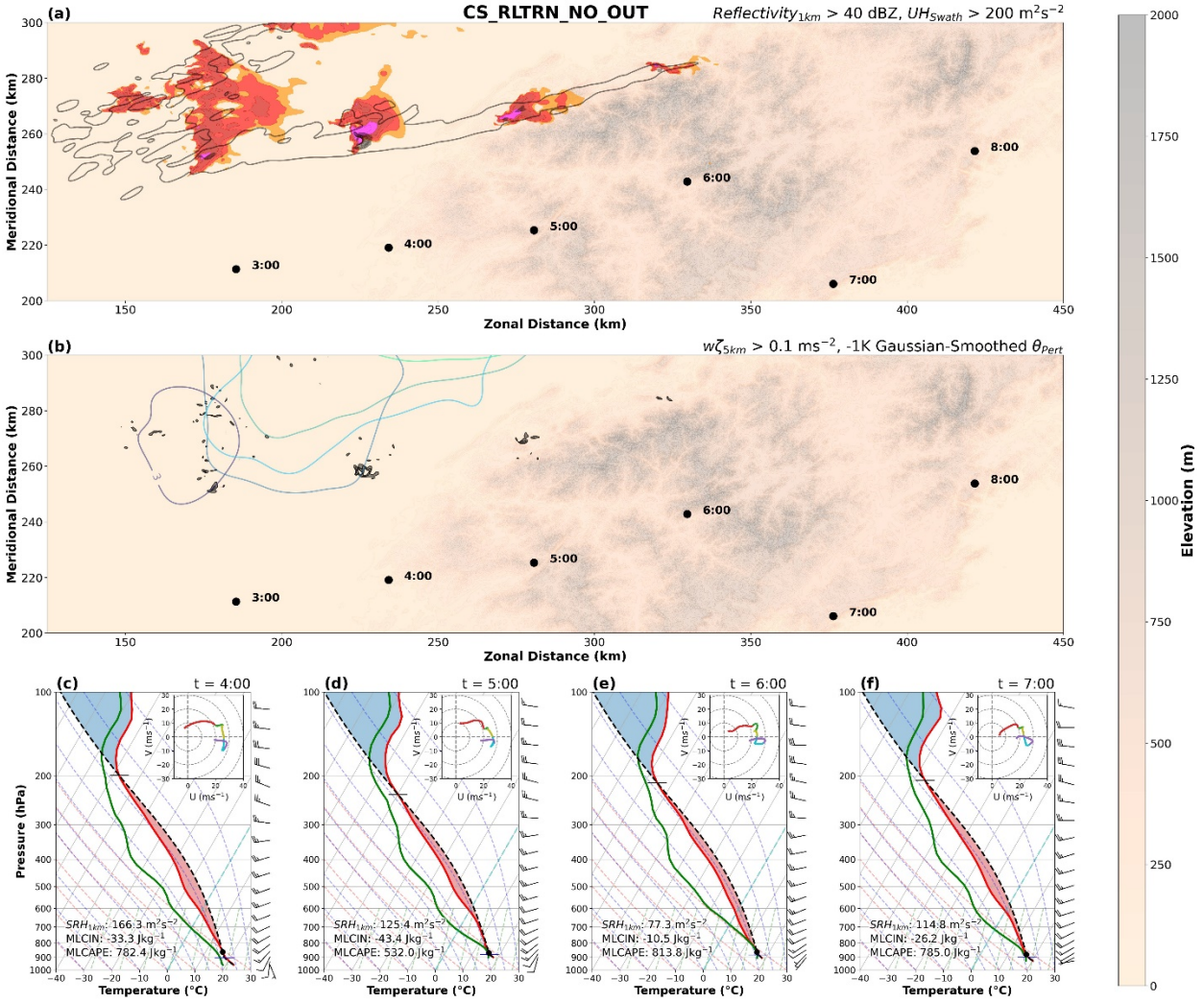

Figure 4.28: Same as in Figure 4.3 but for CS_RLTRN_NO_OUT.

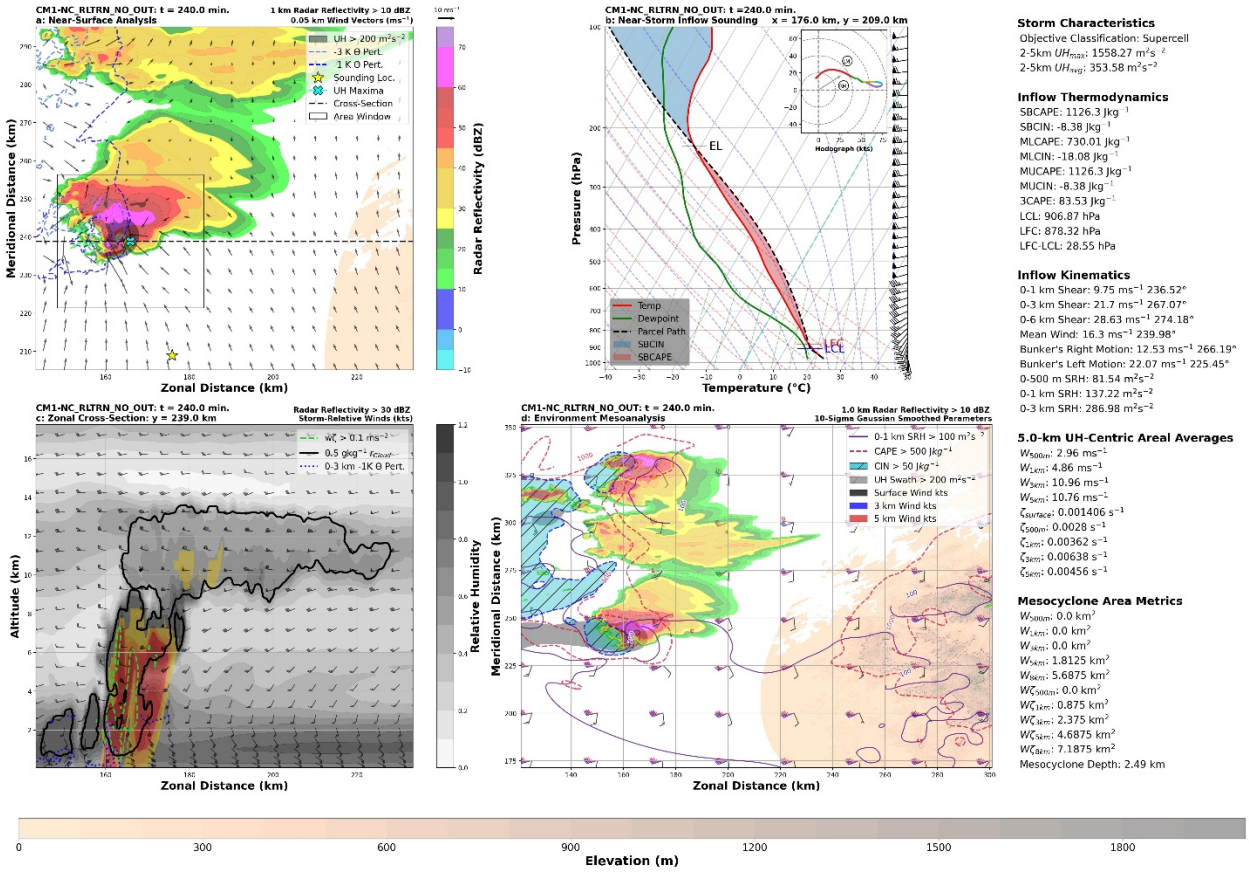

Figure 4.29: Same as in Figure 4.6 but for NC_RLTRN_NO_OUT at t= 240 min. when the storm was at peak intensity.

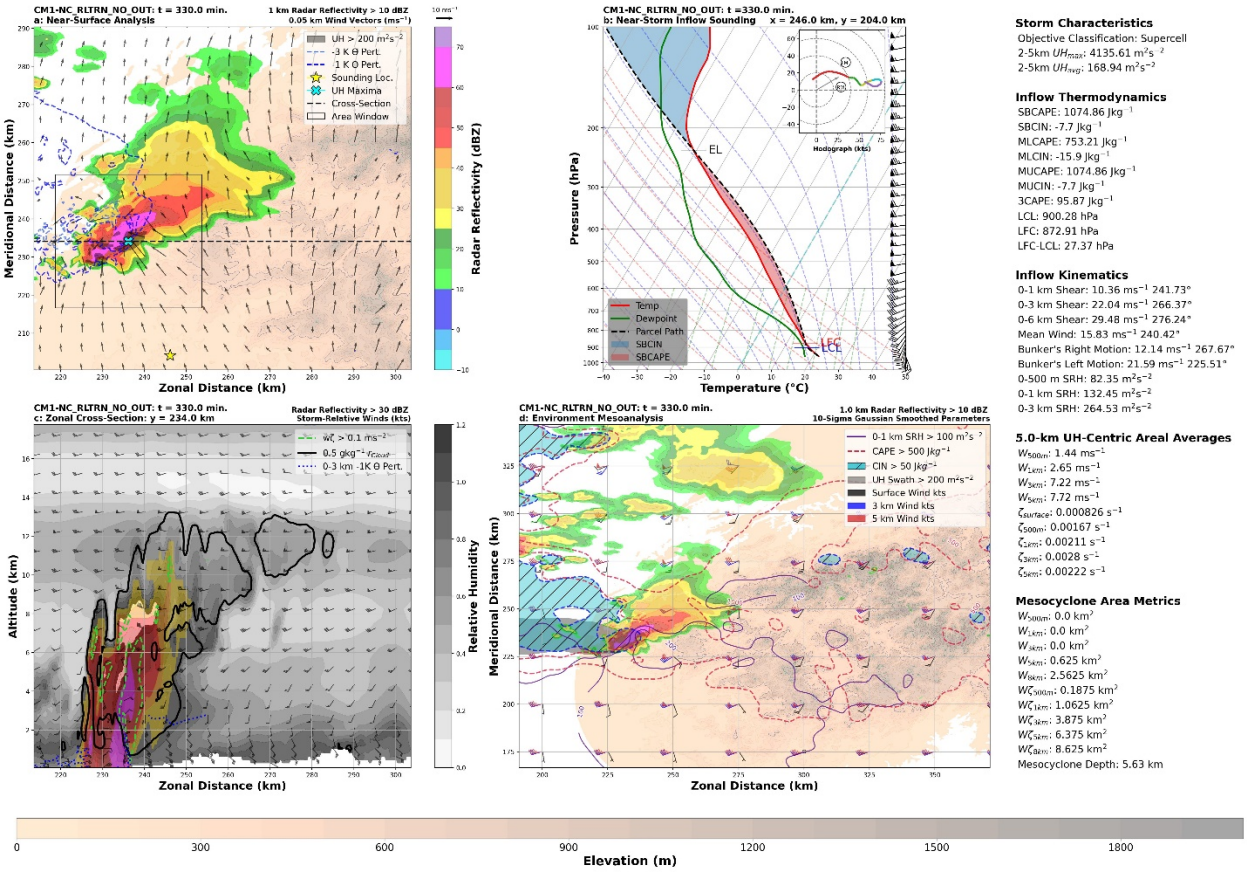

Figure 4.30: Same as in Figure 4.6 but for NC_RLTRN_NO_OUT at t= 330 min.

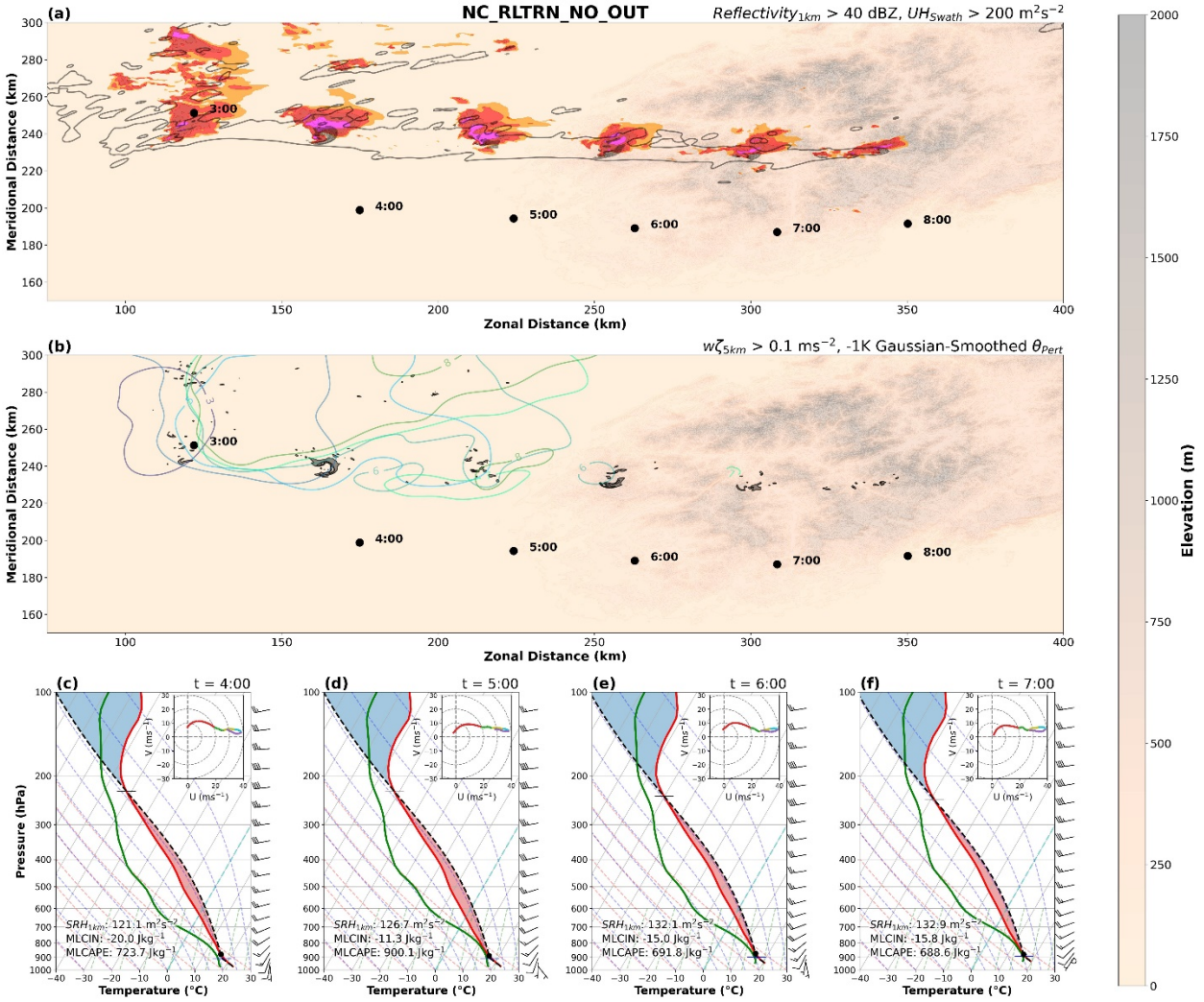

Figure 4.31: Same as in Figure 4.3 but for NC_RLTRN_NO_OUT.

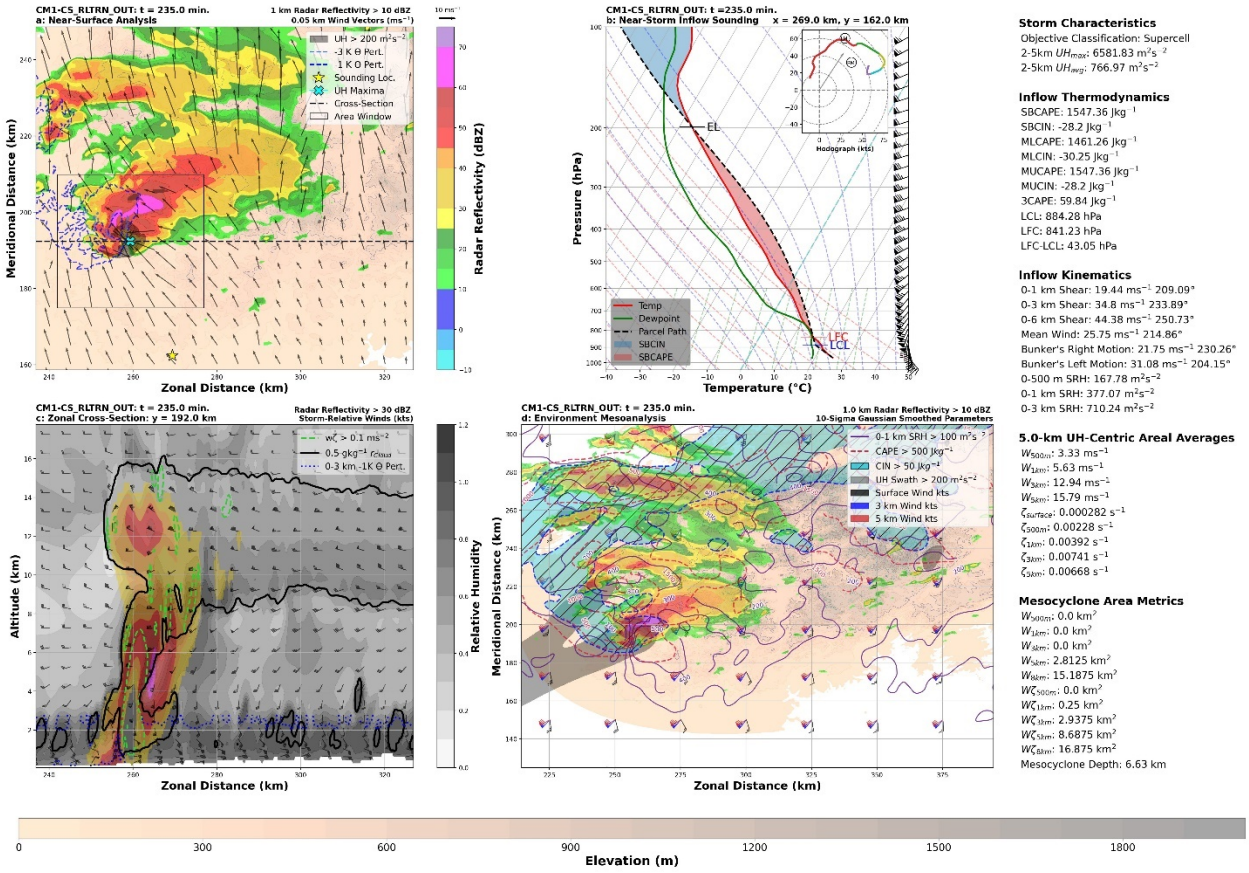

Fig. 4.32: Same as in Figure 4.6 but for CS_RLTRN_OUT at t= 235 min. when it was at peak intensity.

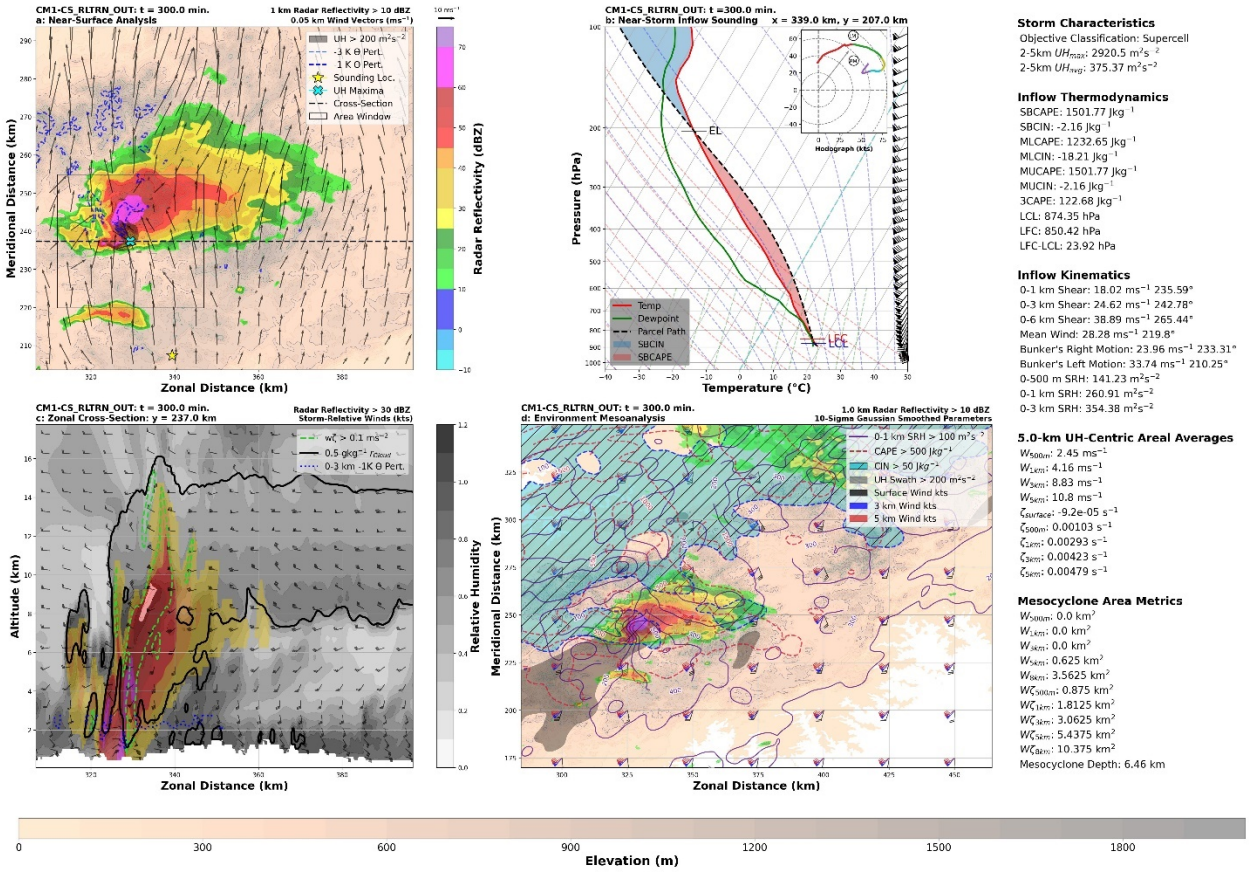

Figure 4.33: Same as in Figure 4.6 but for CS_RLTRN_OUT at t= 300 min.

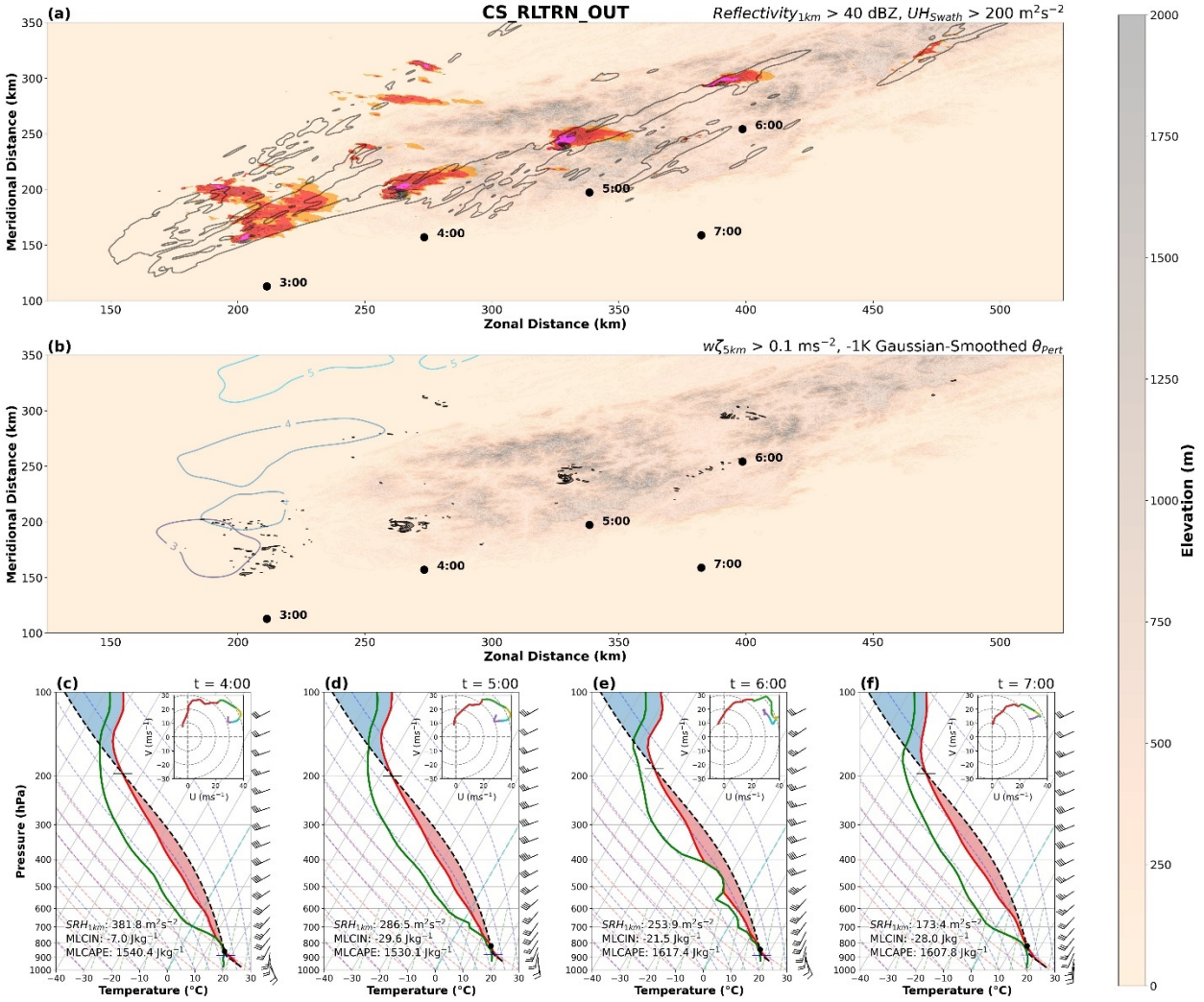

Figure 4.34: Same as in Figure 4.3 but for CS_RLTRN_OUT.

CHAPTER 5: SUMMARY AND FUTURE WORK

5.1 Introduction

This chapter summarizes the key results from our numerical simulations. Section 5.2 provides a broad overview of the salient results and how it relates to the prior literature. Section 5.3 highlights the results most pertinent to operational forecasters by condensing the relevant information into a conceptual model. Section 5.4 discusses the limitations of our results and provides direction for future research that could improve or build upon the current work.

5.2 Summary

The current study works to address some limitations of prior works by using an idealized cloud-resolving numerical model (CM1; Bryan and Fritsch 2002) to explore the sensitivity of supercells in realistic background environments to complex terrain in a controlled manner. Simulated storms were initialized in a horizontally homogenous background environment derived from the composite upstream/initiation crossing and non-crossing soundings discussed in Purpura et al. (2022). Three different terrain configurations (CTL, ID_TRN, RLTRN) were used to explore how the Appalachians modulate supercells and their inflow environments. Additional subsets were also explored (e.g., MOD, OUT, NO_OUT) resulting in 12 unique simulations. Our simulations generally showed that complex topography results in significant modulations to the local storm environment at both the meso-β (20-200 km) and meso-γ (2-20 km) scales. Kinematic modulations usually favored supercell maintenance while thermodynamic modulations lead to dissipation or upscale growth. The following discussion will elaborate on these findings in detail via a consensus of all 12 simulations.

Both crossing and non-crossing environments experienced low-level kinematic enhancements via terrain blocking that favored supercell maintenance. Blocking increased

vertical shear in the 0-3 km layer resulting in additional ambient helicity to sustain and/or amplify the mesocyclone. Blocking effects were largely a meso-β phenomenon with upstream enhancements observed as far as 100 km from localized ridges, also seen in Smith et al. (2016). The complexity of the terrain field also played a significant role in realizing such blocking-induced enhancements, as Scheffknecht et al. (2017) noted in their simulation of an Alpine Supercell. During our idealized terrain simulations, blocking effectively maintained 0-3 km kinematic parameters that were comparable to the already favorable base-state (e.g., CS_TRN, NC_TRN). The more complex realistic terrain profile better captured the low-level accelerations associated with blocked flow, resulting in notable SRH enhancements from the base-state along the upstream slope (e.g., CS_RLTRN_NO_OUT, NC_RLTRN_NO_OUT). Our simulations suggest blocking is likely a key component in supercell maintenance during the initial interactions with complex topography and shows little discrimination between crossers and non-crossers.

Wind profile changes were also observed in response to terrain channeling, where moist, vorticity-rich air was accelerated between two bounding ridges, leading to increases in ambient 0-3 km shear and SRH. This terrain effect was not present in the idealized terrain profile due to a single smooth ridge, but channeling effects were observed in three of the five realistic terrain simulations (CS_RLTRN_ALL, NC_RLTRN_ALL, CS_RLTRN_OUT) where amplified SRH aided in maintaining supercellular convection.

The above channeling effects were a meso-γ phenomenon, and thus challenging to quantify through our near-storm inflow soundings (~30 km from the updraft). As a result, we subjectively identified its influence by utilizing the near-surface wind vectors and the 0-1 km SRH field in our mesoanalysis plots (e.g., Fig 4.25a and d). The combination of these data

showed that terrain channeling effects began as the storm approached the opening a localized valley, and waned towards the exit. Inflow winds would parallel and accelerate through the valley towards the updraft resulting in mesocyclone intensification. These enhancements were usually observed when mesocyclone intensity was on decline, supporting prior notions that channeling is critical for supercell maintenance while traversing complex terrain (Bosart et al. 2006; Gaffin 2012; Tang et al. 2016; LeBel et al. 2021). As such, channeling is likely key in realizing crossing supercells and thus, additional work is needed to explore a greater spectrum of possible channeling enhancements.

Air flow over orographic features has been noted as a common source of environmental modification in prior literature (e.g., MD2011; Smith et al. 2016; Tang et al. 2016; Katona and Markowski 2021). We designed our MOD simulations, from the idealized terrain suite, to explore storm sensitivities to upslope flow via cross-barrier flow. When simulated storms ascended steeper terrain slopes, we observed some dynamic enhancements to mesocyclone intensity and size as cross-barrier inflow was forced up into the updraft by the terrain. Precipitation production increased because of these enhancements resulting in prolonged cold pool maintenance, when compared to CTL. Simulations showed that supercell maintenance was highly sensitive to cold pool size and intensity: with smaller/weaker cold pools resulting in dissipation for crossing environments, and large/stronger cold pools promoting upscale growth in non-crossing environments. These differences appear related to drier mid-levels (700-400 hPa) observed in non-crossing simulations, which were statistically significant at both the peak and downstream points in Purpura et al. (2022).

Agreement between the observations and the simulations is promising, but we should also note that an idealized modeling framework introduces some additional caveats that control

cold pool properties as well. Different microphysics parameterization schemes result in variable cold pool maintenance, even without the inclusion of terrain (Morrison and Milbrandt 2011; Johnson et al. 2016). Additionally, the background environments were fixed and did not necessarily evolve consistently with the observations, most notably when comparing crossing inflow soundings with the respective peak and downstream/dissipation composites. As such, there are additional sensitivities to explore before drawing conclusive inferences on how upslope flow acts to encourage supercell maintenance.

Downslope flow also results in significant environmental modification that were largely unfavorable for supercell maintenance, Simulations showed that downsloping winds modify the local environments through subsidence, resulting reduced CAPE, elevated LCLs and enhanced CIN on the leeside of any significant ridges, consistent with prior literature (MD2011; Katona et al. 2016; Katona and Markowski 2021). While neither MOD supercell persisted long enough to encounter the idealized leeside environment, mesoanalysis did show CIN pooling as evidence of downsloping. Indeed, two realistic terrain supercells (NC_RLTRN_NO_OUT, CS_RLTRN_OUT) met their demise as they moved into downslope-enhanced CIN fields. Such results imply a high degree of sensitivity to low-level wind direction and storm motion. Greater cross-barrier flow on the leeside favors more significant environmental modulations towards an unfavorable state. Storm motion dictates when and how long the storm will be subjected to the unfavorable environment. Additionally, a more robust supercell can thrive in downsloping environments longer (CS_RLTRN_OUT). As such, downslope flow likely plays a key role in the longevity of supercells as they traverse complex terrain.

Our simulations consistently showed four key terrain-induced mechanisms responsible for supercell modulation while traversing complex terrain. Again, these modulation usually

resulted in kinematic enhancements and thermodynamic inhibitions that modulate supercells, consistent with the observations (McKeown 2021; Purpura et al. 2022). The magnitude of these environmental modifications were largely in agreement for non-crossing simulations, were we see consistent kinematics (0-3 km SRH ~ 200 m^2s^{-2}) and reduced thermodynamic parameters (MLCAPE < 750 Jkg^{-1}) in the inflow soundings, consistent with the evolution discussed in Purpura et al. (2022). Crossing environments largely remained constant in the idealized terrain simulations. Realistic terrain resulted in more environmental variability. Purpura et al. (2022) suggests the environment evolution should be characterized by increasing kinematics (0-3 km SRH > 300 m^2s^{-2}) as thermodynamics wane (MLCAPE < 500 Jkg^{-1}), which was not consistently seen in the simulations (SRH ~ 250-300 m^2s^{-2}; MLCAPE > 750 Jkg^{-1}). This may explain why we were unable to replicate a crossing supercell in our simulations. Additional work is needed to control for environmental heterogeneity in the model to increase the confidence in our results. Still the current work has shown strong consistencies with prior literature and therefore is a viable starting point to formulate a new conceptual forecasting model of supercell behavior in the south-central Appalachians.

5.3 Conceptual Forecasting Model

The following discussion will break down the key results of this study in a manner that is useful for forecasting application. This is accomplished by summarizing each of the four-key terrain-induced processes from Section 5.2 in a visual and numeric manner, providing a quick reference to forecasters when supercellular convection threatens the study area. Visual aids will present a three-step timeline of radar structure and updraft size over time when a particular terrain-induced modification is dominant. Numeric values are included to quantify the expected change in relevant radar and sounding parameters as a quantitative guideline to express whether

supercellular convection can be maintained due to that mechanism. These conceptual model figures are broadly representative of the range of possible outcomes and need to be used in conjunction with one another as these mechanisms often occur sequentially or simultaneously.

Terrain Blocking Conceptual Model

Figure 5.1 summarizes a conceptual model by which supercells may be influenced by terrain blocking in the south-central Appalachians. The model assumes a mature quasi-steady supercell has formed before any terrain-induced modifications have occurred. This supercell approaches a westward facing slope , with ambient low-level flow containing a parallel component to the terrain (Fig. 5.1a). As the storm approaches the base of the terrain, low-level flow is effectively blocked by the barrier and begins to accelerate along the terrain contours. Such accelerations act to increase ambient 0-3 km shear and helicity along the windward slope and can be observed as far as 100 km from ridge peak (Smith et al. 2016). An approaching storm will respond to the enhanced inflow by intensifying, resulting in a more robust mesocyclone and enhanced precipitation production downstream in the FFD region (Fig. 5.1b). Blocking-induced enhancements continue to be observed until the storm travels immediately past the orographic feature responsible for the blocking effect. At this point the storm tends to weaken as the ambient environment becomes more in line with pre-blocking observations (Fig. 5.1c).

Blocking effects should be fairly resolvable via the current WSR-88D network, given that the associated impacts can occur well away from the terrain peak. The realistic terrain simulations suggest that topographic relief and slope orientation may modulate how far away blocking effects can be resolved. Generally, larger reliefs with a westward slope generated more significant ambient kinematic enhancements. Operational forecasters should monitor radar

products such as rotational velocity, mesocyclone depth and/or diameter, Vertically Integrated Liquid (VIL), and Normalized Rotation (NROT) when looking for blocking effects on observed supercells in the study region. Gradual increases of these products as a storm approaches a localized ridge suggest blocking enhancements are actively occurring, especially if the increase continues over consecutive scans. Additionally, blocking enhancements should be observable via the HRRR (Benjamin et al. 2016) given the more meso-β scale ambient modulations. These recommendations are summarized in Fig. 5.1d.

Terrain Channeling Conceptual Model

Figure 5.2 summarizes a conceptual model by which supercells may be influenced by terrain channeling in the south-central Appalachians. The model assumes a mature quasi-steady supercell has formed before any terrain-induced modifications have occurred. This supercell approaches a localized valley bounded by two ridges from the west. Ambient low-level flow has a strong easterly component which parallels the valley resulting in terrain-channeled flow (Fig. 5.2a). The two bounding ridges force low-level accelerations within the valley, effectively increasing shear and helicity within the 0-3 km layer. This holds true for any valley/flow orientation that acts to lengthen the ambient hodograph (e.g., easterly low-level flow with westerly upper-level flow). As the storm approaches the valley opening, this horizontal vorticity-rich air is funneled directly into the updraft promoting intensification via dynamic stretching (Fig. 5.2b). Enhancements usually wane once the supercell traverses to the other side of the local valley unless another terrain-induced mechanism favors continued shear modulations to maintain the storm in its enhanced state (Fig. 5.2c). Note that the supercell does not necessarily have to traverse through the entire valley to see enhancements, though that would prolong channeling

effects. Channeling enhancements were often seen on the meso-γ scale and may not be resolvable via any current observation network. As such, we suggest operational forecasters to pay close attention to the forecasted storm track in relation to the underlying terrain when a supercell approaches any localized valley. WSR-88D products such as rotational velocity, mesocyclone depth and/or diameter, VIL, and NROT should show increases over consecutive scans if the effects occur (Fig. 5.2d). If possible, we recommend the WFOs use the Warn-on-Forecast System (WoFS; Stensrud et al. 2009) for numerical guidance of terrain channeling. WoFS provides a higher temporal resolution (5 min) from an ensemble which should provide increased confidence in channeling enhancements when compared to the hourly output from the operational HRRR alone.

Upslope Flow Conceptual Model

Figure 5.3 summarizes a conceptual model by which supercells may be influenced by upslope flow in the south-central Appalachians. The model assumes a mature quasi-steady supercell has formed before any terrain-induced modifications have occurred. This supercell approaches an elevated slope from the west, with ambient low-level flow containing a perpendicular component to the terrain. The flow is largely upslope creating a low-level convergence zone along the windward slope of the terrain (Fig. 5.3a). As the storm approaches the base of the terrain, this convergence zone effectively forces additional air into the updraft resulting in dynamic intensification of the mesocyclone. Consequentially, precipitation production increases in the FFD region as the updraft advects additional hydrometeors downstream. FFD enhancements play a role in modulating cold pool intensity which can promote supercell maintenance. Alternatively, this could lead to outflow dominance and promote

upscale growth. The current findings do not provide much guidance on the sensitivity to cold pool maintenance, warranting some caution when applying this conceptual model (Fig 5.3b). If the storm remains supercellular after reaching the peak elevation, it may continue to experience dynamic enhancements in response to recycling vorticity-rich parcels from the amplified FFD (Fig. 5.3c). Outside of the Cumberland Plateau, most of the south-central Appalachians is characterized by a series of successive ridges (e.g., Blue Ridge, Allegheny Mountains). This suggests storm will often transition into a downslope dominant environment after completing an upslope ascent. The reader is referred to use the upslope and downslope conceptual models in conjunction for a full understand of possible outcomes. Increases in similar WSR-88D parameters as the prior two models would provide quantitative evidence for upslope enhancements (Fig. 5.3d). Again, the HRRR's temporal resolution may not be sufficient to capture these effects, making WoFS a better alternative if possible.

Downslope Flow Conceptual Model

Figure 5.4 summarizes a conceptual model by which supercells may be influenced by downslope flow in the south-central Appalachians. This model continues where the upslope model left off, assuming a quasi-steady supercell successfully traversed up the windward slope of any given terrain feature. The storm approaches the leeward slope where ambient low-level flow now contains a considerable downslope component (Fig. 5.4a), resulting in adiabatic warming. This creating a thermodynamically hostile environment by enhancing CIN along the leeward slope, which effectively cuts off inflow into the updraft leading to weakening (Figs. 5.4b-c). Prior observational work suggests that vortex stretching promotes dynamic enhancements as the storm descends downslope (Keighton et al. 2004; Bosart et al. 2006; Prociv

2012). This was not seen in our simulations, likely a result of enhanced CIN making the downslope environment too hostile for continued convection (e.g., CS_MOD; NC_MOD; CS_RLTRN_NO_OUT; CS_RLTRN_OUT).

Downsloping effects are largely dictated by terrain slope, with larger slopes promoting more amplified CIN. These effects can act quickly to promote dissipation, especially for typical non-crossing synoptic environments supportive for cold air damming events (Purpura et al. 2022). Decreases in similar WSR-88D parameters as the prior three models would provide quantitative evidence for downslope effects (Fig. 5.4d). As with upslope flow, the HRRR's temporal resolution may not be sufficient to capture downsloping effects, making WoFS a better alternative if it is available.

5.4 Limitations and Future Work

We have identified several limitations in our study that warrant additional discussion for future work. The first being how sensitive our results are to the general storm track with respect to the underlying terrain. The complexity of the realistic terrain field could support an infinite number of potential storm tracks and low-level flow orientations relative to the terrain, resulting in unique solutions due to different combinations of terrain-induced modulations. A model ensemble approach could help weed out some of the uncertainty associated with storm track through repeated simulations with slightly different initiation points. Individual ensemble members could then be grouped by the dominant terrain-induced mechanism and statistically analyzed to further emphasize the more subjective results of this study.

Additionally, our simulations failed to produce a single supercell that was able to successfully cross the entire terrain field. We hypothesize this to be in part a function of the

model's idealized nature (i.e., a single atmospheric profile that is interpolated to the model domain in a horizontally homogenous manner), with no explicit accounting of synoptic-scale dynamical processes such differential vorticity and temperature advection aiding vertical motion or jet streak dynamics. Such processes may be critical for supercell maintenance during more hostile terrain interactions (e.g., as evident in the 27 April 2011 outbreak; Knupp et al. 2014). Future research could address this limitation by utilizing a full-physics model such as the Weather Research and Forecasting (WRF) model (Skamarock et al. 2008) to complete individual case-study simulations of crossing and non-crossing supercells to quantify the importance of synoptic-scale dynamics during interactions with complex terrain.

Lastly, our simulations assumed that the upstream composite environment will be sufficient to emulate crossing/non-crossing storm behavior alone due to terrain-induced environmental variability in the model that is consistent with observed variability from Purpura et al. (2022). However, modeled environmental heterogeneities were not consistent with the observations. Accordingly, we suggest repeating our experiments by running simulations where the model background field is forced to evolve in a consistent manner with the observations. Base-State Substitution (BSS; Letkewicz et al. 2013; Davenport et al. 2019) is an additional module that can be added to the CM1's source code to introduce environmental heterogeneity over time while maintaining the existing perturbation fields produced by simulated convection and the terrain field. Figure 5.5 conceptually shows how we could implement BSS into our idealized terrain simulations to ensure the environmental nudging is realized at the appropriate spatial location (i.e., the peak nudging occurs as the simulated storm approaches the peak ridge of the terrain field). Including BSS simulations into our current experiment suite would help to

build up the realism of our simulations which will be critical for verifying our conceptual model of supercell behavior around the south-central Appalachians.

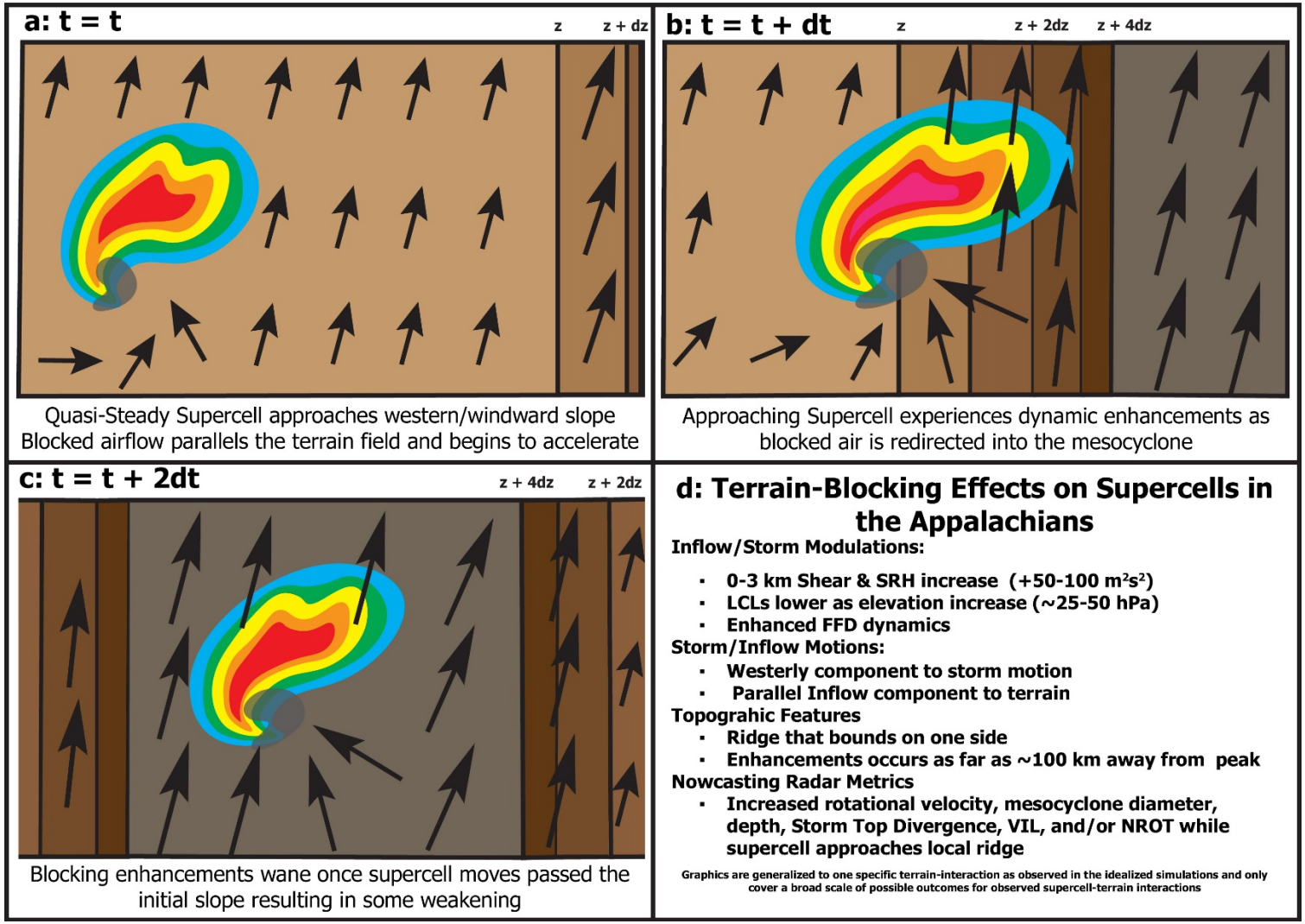

Figure 5.1: A conceptual model of supercell behavior in the south-central Appalachians Mountains when terrain-blocking is the dominant terrain-induced mechanism responsible for environmental modulation.

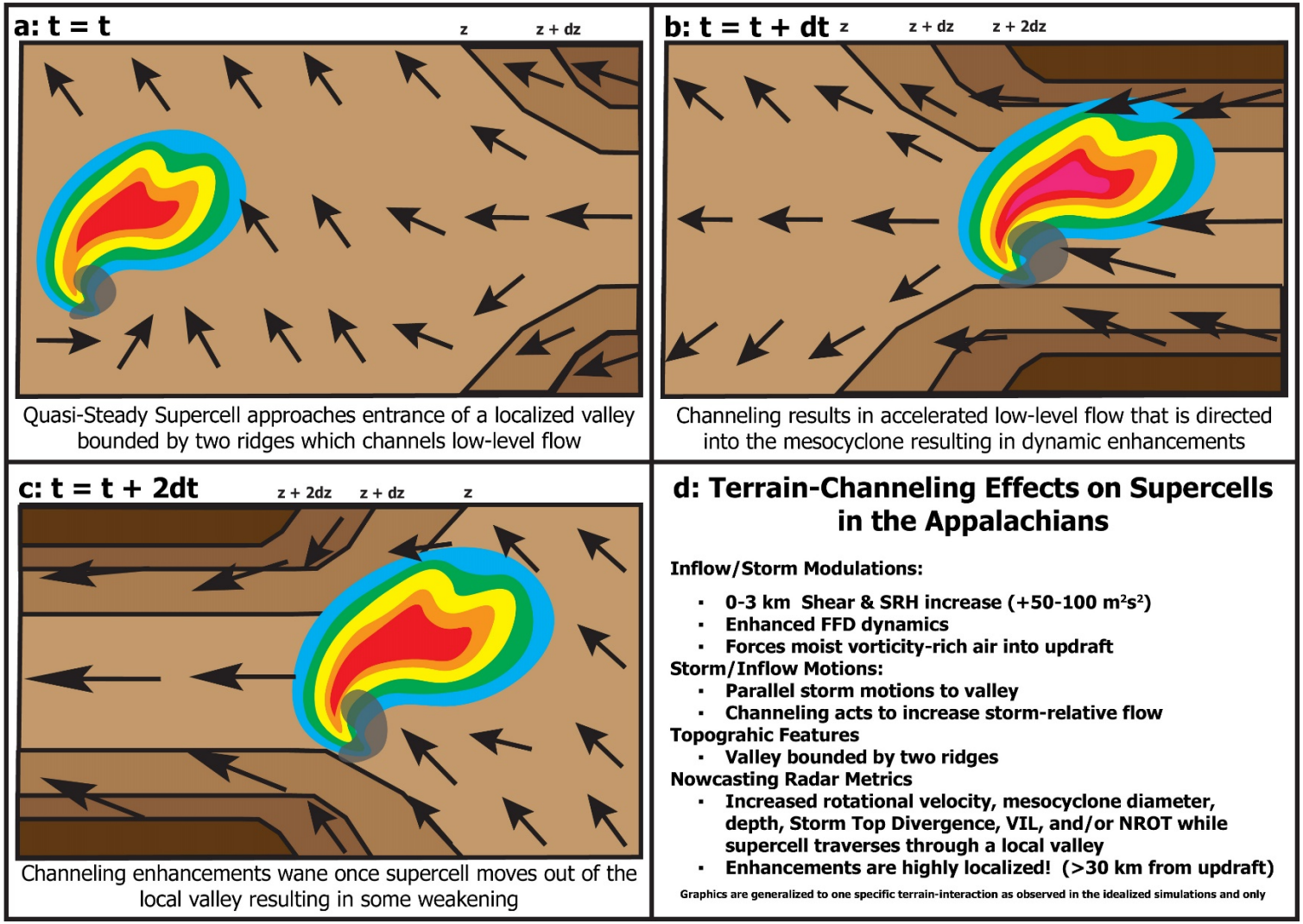

Figure 5.2: A conceptual model of supercell behavior in the south-central Appalachians Mountains when terrain-channeling is the dominant terrain-induced mechanism responsible for environmental modulation.

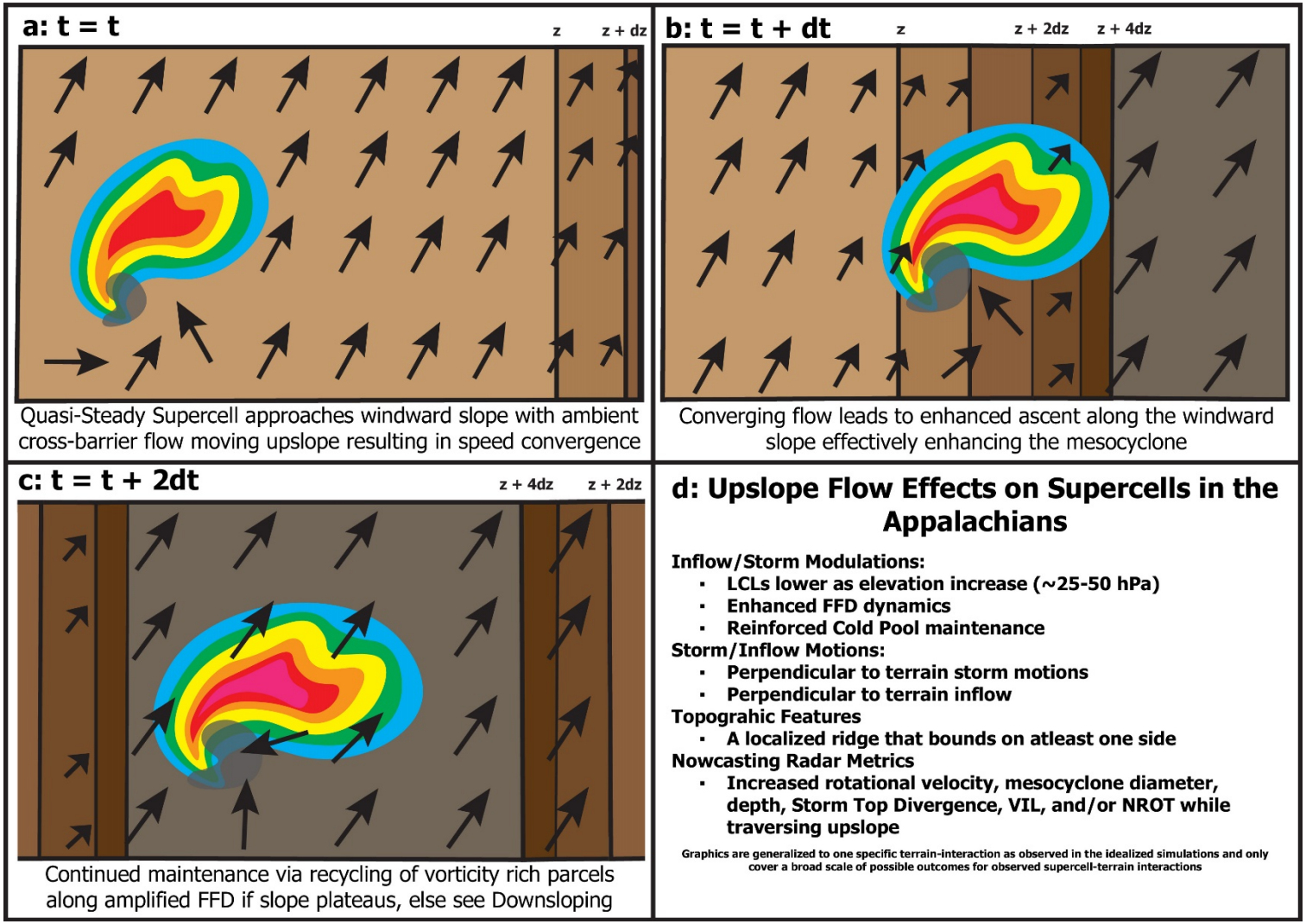

Figure 5.3: A conceptual model of supercell behavior in the south-central Appalachians Mountains when upslope flow is the dominant terrain-induced mechanism responsible for environmental modulation.

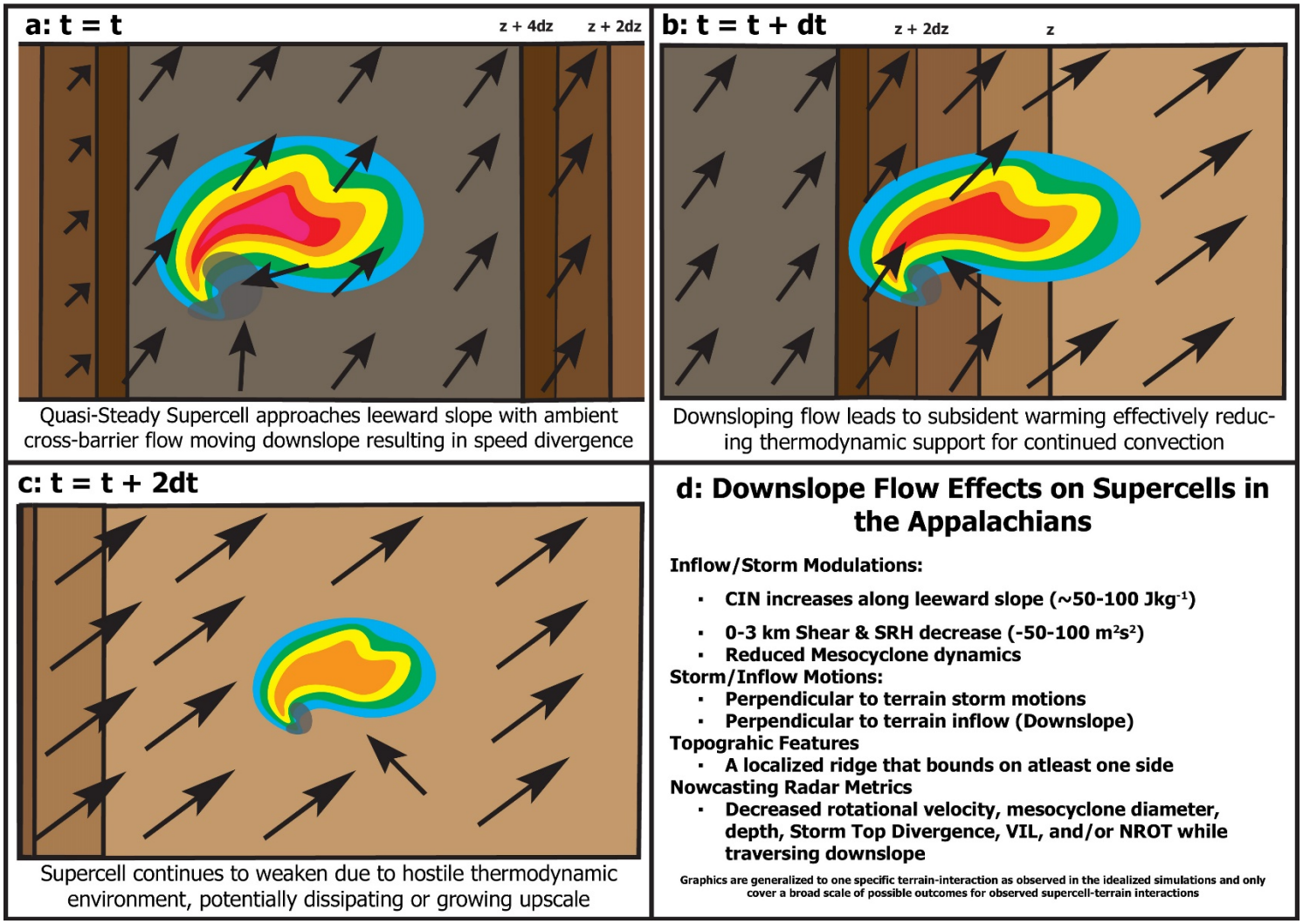

Figure 5.4: A conceptual model of supercell behavior in the south-central Appalachians Mountains when downslope flow is the dominant terrain-induced mechanism responsible for environmental modulation.

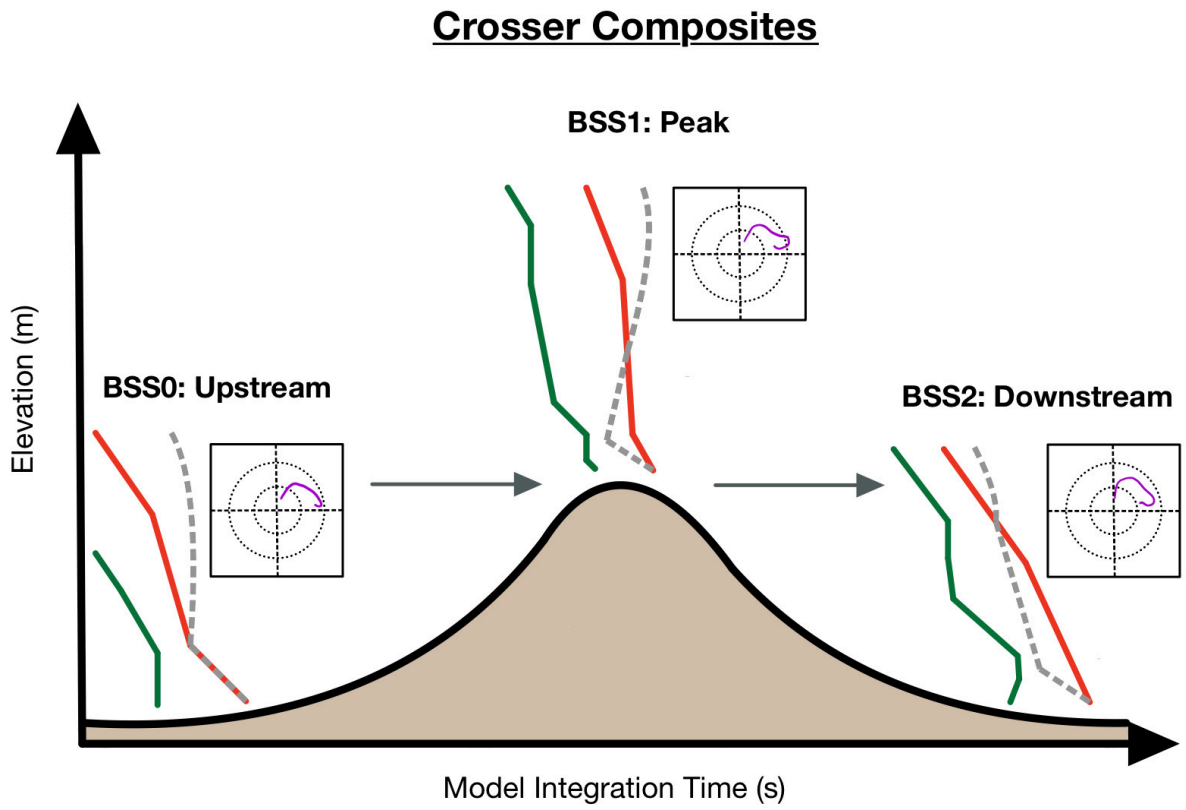

Figure 5.5: A conceptual model of Base-State Substitution (BSS) being implemented for a crossing composite simulation. BSS nudges the model background field from the original base-state BSS0 toward BSS1 and BSS2 over time.

REFERENCES

Adlerman, E. J., Droegemeier, K. K., & Davies-Jones, R. (1999). A Numerical Simulation of Cyclic Mesocyclogenesis, *Journal of the Atmospheric Sciences*, *56*(13), 2045-2069. Retrieved Aug 16, 2022, from https://journals.ametsoc.org/view/journals/atsc/56/13/1520-0469_1999_056_2045_ansocm_2.0.co_2.xml

Benjamin, S. G., Weygandt, S. S., Brown, J. M., Hu, M., Alexander, C. R., Smirnova, T. G., Olson, J. B., James, E. P., Dowell, D. C., Grell, G. A., Lin, H., Peckham, S. E., Smith, T. L., Moninger, W. R., Kenyon, J. S., & Manikin, G. S. (2016). A North American Hourly Assimilation and Model Forecast Cycle: The Rapid Refresh, *Monthly Weather Review*, *144*(4), 1669-1694. Retrieved Sep 16, 2022, from https://journals.ametsoc.org/view/journals/mwre/144/4/mwr-d-15-0242.1.xml

Bosart, L., A. Seimon, K. D. LaPenta, and M. J. Dickinson, 2006: Supercell Tornadogenesis over Complex Terrain. The Great Barrington, Massachusetts, Tornado on 29 May 1995. *Wea. Forecasting*, 21, pp. 897-922.

Brown, M., & Nowotarski, C. J. (2019). The Influence of Lifting Condensation Level on Low-Level Outflow and Rotation in Simulated Supercell Thunderstorms, *Journal of the Atmospheric Sciences*, *76*(5), 1349-1372. Retrieved Dec 29, 2021, from https://journals.ametsoc.org/view/journals/atsc/76/5/jas-d-18-0216.1.xml

Bryan, G. H., and J. M. Fritsch, 2002: A benchmark simulation for moist nonhydrostatic numerical models. *Mon. Wea. Rev.*, 130, 2917-2928.

Bryan, G. H., Romine, G., Trier, S., & Ahijevych, D. (2018, October 23). Impact of terrain on supercells according to idealized simulations with actual terrain. *29th Conference on Severe Local Storms*, Stowe, VT, Retrieved October 24, 2021, from https://ams.confex.com/ams/29SLS/webprogram/Paper348681.html.

Buechler, D. E., E. W. McCaul, S. J. Goodman, R. J. Blakeslee, J. C. Bailey, and P. N. Gatlin, 2004: The severe weather outbreak of 10 November 2002: Lightning and radar analysis of storms in the Deep South. Preprints, *22nd Conf. on Severe Local Storms,* Hyannis, MA, Amer. Meteor. Soc., 16B.8.

Coleman, T. A., & Dixon, P. G. (2014). An Objective Analysis of Tornado Risk in the United States, *Weather and Forecasting*, *29*(2), 366-376. Retrieved Nov 3, 2021, from https://journals.ametsoc.org/view/journals/wefo/29/2/waf-d-13-00057_1.xml

Corfidi, S. F., Weiss, S. J., Kain, J. S., Corfidi, S. J., Rabin, R. M., & Levit, J. J. (2010). Revisiting the 3–4 April 1974 Super Outbreak of Tornadoes, *Weather and Forecasting*, *25*(2), 465-510. Retrieved Oct 16, 2021, from https://journals.ametsoc.org/view/journals/wefo/25/2/2009waf2222297_1.xml

Davenport, C. E., & Parker, M. D. (2015). Observations of the 9 June 2009 Dissipating Supercell from VORTEX2, *Weather and Forecasting*, *30*(2), 368-388. Retrieved Jul 12, 2022, from https://journals.ametsoc.org/view/journals/wefo/30/2/waf-d-14-00087_1.xml

Davenport, C. E., Ziegler, C. L., & Biggerstaff, M. I. (2019). Creating a More Realistic Idealized Supercell Thunderstorm Evolution via Incorporation of Base-State Environmental Variability, *Monthly Weather Review*, *147*(11), 4177-4198. Retrieved Apr 28, 2022, from https://journals.ametsoc.org/view/journals/mwre/147/11/mwr-d-18-0447.1.xml

Davies-Jones, R., 1984: Streamwise vorticity: The origin of updraft rotation in supercell storms. *J. Atmos. Sci*., **41**, 2991-3006

Frame, J., & Markowski, P. (2006). The Interaction of Simulated Squall Lines with Idealized Mountain Ridges, *Monthly Weather Review*, *134*(7), 1919-1941. Retrieved Oct 24, 2021, from https://journals.ametsoc.org/view/journals/mwre/134/7/mwr3157.1.xml

Gaffin, D. M., S. S. Parker, 2006: A Climatology of Synoptic Conditions Associated with Significant Tornadoes across the Southern Appalachian Region. *Wea. Forecasting*, 21, 735-751.

Gaffin, D., M., 2012: The Influence of Terrain During the 27 April 2011 Super Tornado Outbreak and 5 July 2012 Derecho around the Great Smoky Mountains National Park. *26th Conf. on Severe Local Storms,* Nashville TN, Amer. Meteor. Soc.

Geerts, B., T. Andretta, S. Luberda, J. Vogt, Y. Wang, and L. D. Oolman, 2009: A case study of a long-lived tornadic mesocyclone in a low-CAPE complex-terrain environment. *Electronic J. Severe Storms Meteor*., 4 (3), 1-29.

Grams, J. S., Thompson, R. L., Snively, D. V., Prentice, J. A., Hodges, G. M., & Reames, L. J. (2012). A Climatology and Comparison of Parameters for Significant Tornado Events in the United States, *Weather and Forecasting*, *27*(1), 106-123. Retrieved Nov 8, 2021, from https://journals.ametsoc.org/view/journals/wefo/27/1/waf-d-11-00008_1.xml

Guarriello, F., Nowotarski, C. J., & Epifanio, C. C. (2018). Effects of the Low-Level Wind Profile on Outflow Position and Near-Surface Vertical Vorticity in Simulated Supercell Thunderstorms, *Journal of the Atmospheric Sciences*, *75*(3), 731-753. Retrieved Dec 29, 2021, from https://journals.ametsoc.org/view/journals/atsc/75/3/jas-d-17-0174.1.xml

Hocker, J. E., & Basara, J. B. (2008). A Geographic Information Systems–Based Analysis of Supercells across Oklahoma from 1994 to 2003, *Journal of Applied Meteorology and Climatology*, *47*(5), 1518-1538. Retrieved Nov 2, 2021, from https://journals.ametsoc.org/view/journals/apme/47/5/2007jamc1673

Hoyer, S. and Hamman, J., 2017. Xarray: N-D labeled Arrays and Datasets in Python. *Journal of Open Research Software*, 5(1), p.10. DOI: http://doi.org/10.5334/jors.148

Hunter J. D., "Matplotlib: A 2D Graphics Environment," in *Computing in Science & Engineering*, vol. 9, no. 3, pp. 90-95, May-June 2007, doi: 10.1109/MCSE.2007.55.

Johnson, M., Jung, Y., Dawson, D. T., II, & Xue, M. (2016). Comparison of Simulated Polarimetric Signatures in Idealized Supercell Storms Using Two-Moment Bulk Microphysics Schemes in WRF, *Monthly Weather Review*, *144*(3), 971-996. Retrieved Sep 15, 2022, from https://journals.ametsoc.org/view/journals/mwre/144/3/mwr-d-15-0233.1.xml

Kain, J. S., Weiss, S. J., Bright, D. R., Baldwin, M. E., Levit, J. J., Carbin, G. W., Schwartz, C. S., Weisman, M. L., Droegemeier, K. K., Weber, D. B., & Thomas, K. W. (2008). Some Practical Considerations Regarding Horizontal Resolution in the First Generation of Operational Convection-Allowing NWP, *Weather and Forecasting*, *23*(5), 931-952. Retrieved Oct 25, 2021, from https://journals.ametsoc.org/view/journals/wefo/23/5/waf2007106_1.xml

Katona, B., P. Markowski, C. Alexander, S. Benjamin, 2016: The Influence of Topography on Convective Storm Environments in the Eastern United States as Deduced from the HRRR. *Wea. Forecasting,* 31, 1481-1490.

Katona, B., & Markowski, P. (2021). Assessing the Influence of Complex Terrain on Severe Convective Environments in Northeastern Alabama, *Weather and Forecasting*, *36*(3), 1003-1029. Retrieved Oct 24, 2021, from https://journals.ametsoc.org/view/journals/wefo/36/3/WAF-D-20-0136.1.xml

Keighton, S., K. Kostura, C. Liscinsky., 2004: Examination of Tornadic and Non-tornadic Supercells in Southwest Virginia on 28 April 2002. *22nd Conf. on Severe Local Storms, Amer. Meteor. Soc,* Hyannis, MA.

Klemp, J. B., 1987: Dynamics of tornadic thunderstorms. *Ann. Rev. Fluid Mech*., **19**, 369-402

Klemp, J. B., & Rotunno, R. (1983). A Study of the Tornadic Region within a Supercell Thunderstorm, *Journal of Atmospheric Sciences*, *40*(2), 359-377. Retrieved Nov 8, 2021, from https://journals.ametsoc.org/view/journals/atsc/40/2/1520-0469_1983_040_0359_asottr_2_0_co_2.xml

Knupp, K. R., Murphy, T. A., Coleman, T. A., Wade, R. A., Mullins, S. A., Schultz, C. J., Schultz, E. V., Carey, L., Sherrer, A., McCaul, E. W., Jr., Carcione, B., Latimer, S., Kula, A., Laws, K., Marsh, P. T., & Klockow, K. (2014). Meteorological Overview of the Devastating 27 April 2011 Tornado Outbreak, *Bulletin of the American Meteorological Society*, *95*(7), 1041-1062. Retrieved Oct 16, 2021, from https://journals.ametsoc.org/view/journals/bams/95/7/bams-d-11-00229.1.xml

Lane, J., 2008: A Comprehensive Climatology of Significant Tornadoes in the Greenville-Spartanburg, South Carolina County Warning Area (1880-2006). Eastern Region Technical Attachment, no. 2008-01.

LeBel, L. J., Tang, B. H., & Lazear, R. A. (2021). Examining Terrain Effects on an Upstate New York Tornado Event Utilizing a High-Resolution Model Simulation, *Weather and Forecasting*, *36*(6), 2001-2020. Retrieved Nov 5, 2021, from https://journals.ametsoc.org/view/journals/wefo/36/6/WAF-D-21-0018.1.xml

Lemon, L. R., and C. A. Doswell, 1979: Severe Thunderstorm Evolution and Mesocyclone Structure as Related to Tornadogenesis. *Mon. Wea. Rev.*, 107, 1184-1197.

Letkewicz, C. E., & Parker, M. D. (2011). Impact of Environmental Variations on Simulated Squall Lines Interacting with Terrain, *Monthly Weather Review*, *139*(10), 3163-3183. Retrieved Oct 24, 2021, from https://journals.ametsoc.org/view/journals/mwre/139/10/2011mwr3635.1

Letkewicz, C. E., French, A. J., & Parker, M. D. (2013). Base-State Substitution: An Idealized Modeling Technique for Approximating Environmental Variability, *Monthly Weather Review*, *141*(9), 3062-3086. Retrieved Oct 25, 2021, from https://journals.ametsoc.org/view/journals/mwre/141/9/mwr-d-12-00200.1.xml

Lyza, A. W., and K. Knupp, 2014: An Observational Analysis of Potential Terrain Influences on Tornado Behavior. *27th Conf. on Severe Local Storms,* Madison, WI, Amer. Meteor. Soc.

Lyza, A. W., & Knupp, K. R. (2018). A Background Investigation of Tornado Activity across the Southern Cumberland Plateau Terrain System of Northeastern Alabama, *Monthly Weather Review*, *146*(12), 4261-4278. Retrieved Nov 2, 2021, from https://journals.ametsoc.org/view/journals/mwre/146/12/mwr-d-18-0300.1.xml

Mansell, E. R., & Ziegler, C. L. (2013). Aerosol Effects on Simulated Storm Electrification and Precipitation in a Two-Moment Bulk Microphysics Model, *Journal of the Atmospheric Sciences*, *70*(7), 2032-2050. Retrieved Sep 22, 2022, from https://journals.ametsoc.org/view/journals/atsc/70/7/jas-d-12-0264.1.xml

Markowski, P., & Richardson, Y. (2010). Ch 8 Organization of Isolated Convection. In *Mesoscale Meteorology in Midlatitudes*, Wiley-Blackwell, (pp. 213–242).

Markowski, P.M., N. Dotzek, 2011: A Numerical Study of the Effects of Orography on Supercells. Atmospheric Research 100, 457-478.

May, R. M., Arms, S. C., Marsh, P., Bruning, E., Leeman, J. R., Goebbert, K., Thielen, J. E., and Bruick, Z., 2020: MetPy: A Python Package for Meteorological Data. Unidata, https://github.com/Unidata/MetPy, doi:10.5065/D6WW7G29.

McKeown, K. E. (2021). *Radar Characteristics of Observed Supercell Thunderstorms interacting with the Appalachian Mountains* (Order No. 28416999). Available from Dissertations & Theses @ University of North Carolina Charlotte. (2528579145).

Miglietta, M., 2017: Numerical Simulations of a Tornadic Supercell over the Mediterranean. *Wea. Forecasting*, 32, p. 1209-1226.

Morrison, H., & Milbrandt, J. (2011). Comparison of Two-Moment Bulk Microphysics Schemes in Idealized Supercell Thunderstorm Simulations, *Monthly Weather Review*, *139*(4), 1103-1130. Retrieved Sep 15, 2022, from https://journals.ametsoc.org/view/journals/mwre/139/4/2010mwr3433.1.xml

Mulholland, J. P., Nesbitt, S. W., Trapp, R. J., & Peters, M. (2020). The Influence of Terrain on the Convective Environment and Associated Convective Morphology from an Idealized Modeling Perspective, *Journal of the Atmospheric Sciences*, *77*(11), 3929-3949.

Naylor, J., & Gilmore, M. S. (2012). Convective Initiation in an Idealized Cloud Model Using an Updraft Nudging Technique, *Monthly Weather Review*, *140*(11), 3699-3705. Retrieved Oct 24, 2021, from https://journals.ametsoc.org/view/journals/mwre/140/11/mwr-d-12-00163.1.xml

NOAA, (2016): *Maps of the NWS Rawinsonde Network.* Accessed October 2, 2021, https://www.weather.gov/upperair/nws_upper.

Parker, M. D. (2014). Composite VORTEX2 Supercell Environments from Near-Storm Soundings, *Monthly Weather Review*, *142*(2), 508-529. Retrieved Jun 20, 2022, from https://journals.ametsoc.org/view/journals/mwre/142/2/mwr-d-13-00167.1.xml

Parker, M. D., & Johnson, R. H. (2000). Organizational Modes of Midlatitude Mesoscale Convective Systems, *Monthly Weather Review*, *128*(10), 3413-3436. Retrieved Dec 29, 2021, from https://journals.ametsoc.org/view/journals/mwre/128/10/1520-0493_2001_129_3413_omommc_2.0.co_2.xml

Prociv, K.A., 2012: Terrain and Landcover Effects of the Southern Appalachian Mountains on The Rotational Low Level Wind Fields of Supercell Thunderstorms.

Purpura, S. M., C. E. Davenport, M. D. Eastin, K. E. McKeown, and R. R. Riggin, (2022). *Environmental Evolution of Supercell Thunderstorms Interacting with the Appalachian Mountains.* Submitted to *Weather and Forecasting*, in review.

Rasmussen, E. N., & Blanchard, D. O. (1998). A Baseline Climatology of Sounding-Derived Supercell and Tornado Forecast Parameters, *Weather and Forecasting*, *13*(4), 1148-1164. Retrieved Nov 2, 2021, from https://journals.ametsoc.org/view/journals/wefo/13/4/1520-0434_1998_013_1148_abcosd_2_0_co_2.xml

Rasmussen, E. N., Straka, J. M., Davies-Jones, R., Doswell, C. A., III, Carr, F. H., Eilts, M. D., & MacGorman, D. R. (1994). Verification of the Origins of Rotation in Tornadoes Experiment: VORTEX, *Bulletin of the American Meteorological Society*, *75*(6), 995-1006. Retrieved Oct 16, 2021, from

https://journals.ametsoc.org/view/journals/bams/75/6/1520-0477_1994_075_0995_votoor_2_0_co_2.xml

Reeves, H. D., & Lin, Y. (2007). The Effects of a Mountain on the Propagation of a Preexisting Convective System for Blocked and Unblocked Flow Regimes, *Journal of the Atmospheric Sciences*, *64*(7), 2401-2421.

Scheffknecht, P., S. Serafin, and V. Grubišić., 2017: A long-lived supercell over mountainous Terrain. Q.J.R. Meteorol. Soc., 143: 2973-2986.

Schneider, D., G., 2009: The Impact of Terrain on Three Cases of Tornadogenesis in the Great Tennessee Valley. National Weather Association, Electronic Journal of Operational Meteorology, 2009-EJ11.

Skamarock, W. C., and Coauthors, 2008: A description of the Advanced Research WRF version 3. NCAR Tech. Note NCAR/TN-475+STR, 113 pp, https://doi.org/10.5065/D68S4MVH.

Smith, G.M., Y. Lin, R. Yevgenii., 2016: Orographic Effects on Supercell: Development and Structure, Intensity and Tracking. Environment and Natural Resources Research, 6, no. 2.

Soderholm, B., Ronalds, B., & Kirshbaum, D. J. (2014). The Evolution of Convective Storms Initiated by an Isolated Mountain Ridge, *Monthly Weather Review*, *142*(4), 1430-1451. Retrieved Oct 24, 2021, from https://journals.ametsoc.org/view/journals/mwre/142/4/mwr-d-13-00280.1.xml

Stensrud, D. J., Xue, M., Wicker, L. J., Kelleher, K. E., Foster, M. P., Schaefer, J. T., Schneider, R. S., Benjamin, S. G., Weygandt, S. S., Ferree, J. T., & Tuell, J. P. (2009). Convective-Scale Warn-on-Forecast System, *Bulletin of the American Meteorological Society*, *90*(10), 1487-1500. Retrieved Sep 15, 2022, from https://journals.ametsoc.org/view/journals/bams/90/10/2009bams2795_1.xml

Stonefield, R. C., J. E. Hudgins, 2006: A Severe Weather Climatology for the WFO Blacksburg, Virginia, County Warning Area. NOAA Technical Memorandum, NWS ER-99.

Tang, B., M. Vaughan, R. Lazear, Corbosiero, K., Bosart, L., 2016: Topographic and Boundary Influences on the 22 May 2014 Duanesburg New York, Tornadic Supercell. *Wea. Forecasting*, 31, pp. 107-127.

Thompson, R. L., Edwards, R., Hart, J. A., Elmore, K. L., & Markowski, P. (2003). Close Proximity Soundings within Supercell Environments Obtained from the Rapid Update Cycle, *Weather and Forecasting*, *18*(6), 1243-1261. Retrieved Nov 2, 2021, from https://journals.ametsoc.org/view/journals/wefo/18/6/1520-0434_2003_018_1243_cpswse_2_0_co_2.xml

Van Rossum, G., & Drake, F. L. (2009). *Python 3 Reference Manual*. Scotts Valley, CA: CreateSpace.

Weisman, M. L., & Klemp, J. B. (1984). The Structure and Classification of Numerically Simulated Convective Stormsin Directionally Varying Wind Shears, *Monthly Weather Review*, *112*(12), 2479-2498. Retrieved Dec 30, 2021, from https://journals.ametsoc.org/view/journals/mwre/112/12/1520-0493_1984_112_2479_tsacon_2_0_co_2.xml

Wurman, J., Dowell, D., Richardson, Y., Markowski, P., Rasmussen, E., Burgess, D., Wicker, L., & Bluestein, H. B. (2012). The Second Verification of the Origins of Rotation in Tornadoes Experiment: VORTEX2, *Bulletin of the American Meteorological Society*, *93*(8), 1147-1170. Retrieved Oct 16, 2021, from https://journals.ametsoc.org/view/journals/bams/93/8/bams-d-11-00010.1.xml

Ziegler, C. L., Mansell, E. R., Straka, J. M., MacGorman, D. R., & Burgess, D. W. (2010). The Impact of Spatial Variations of Low-Level Stability on the Life Cycle of a Simulated Supercell Storm, *Monthly Weather Review*, *138*(5), 1738-1766. Retrieved Sep 7, 2022, from https://journals.ametsoc.org/view/journals/mwre/138/5/2009mwr3010.1.xml